Analysis of Textile Composite Structures Subjected to High Temperature Oxidizing Environment

AFOSR Award No. FA9550-07-1-0207

John Whitcomb

Texas A&M University

Final Report

August 2010

Report Documentation Page

Form Approved
OMB No. 0704-0188

1. REPORT DATE	2. REPORT TYPE	3. DATES COVERED
01 AUG 2010		

4. TITLE AND SUBTITLE	5a. CONTRACT NUMBER
Analysis of Textile Composite Structures Subjected to High Temperature Oxidizing Environment	5b. GRANT NUMBER
	5c. PROGRAM ELEMENT NUMBER

6. AUTHOR(S)	5d. PROJECT NUMBER
John Whitcomb	5e. TASK NUMBER
	5f. WORK UNIT NUMBER

7. PERFORMING ORGANIZATION NAME(S) AND ADDRESS(ES)	8. PERFORMING ORGANIZATION REPORT NUMBER
Aerospace Engineering Department,3141 TAMU,Texas A&M University,College Station,TX,77843	

9. SPONSORING/MONITORING AGENCY NAME(S) AND ADDRESS(ES)	10. SPONSOR/MONITOR'S ACRONYM(S)
	11. SPONSOR/MONITOR'S REPORT NUMBER(S)

12. DISTRIBUTION/AVAILABILITY STATEMENT

Approved for public release; distribution unlimited.

13. SUPPLEMENTARY NOTES

14. ABSTRACT

This research work has contributed in various ways to help develop a better understanding of textile composites and materials with complex microstructures in general. An instrumental part of this work was the development of a framework that made it convenient to perform multiscale/multiphysics analyses of advanced materials such as textile composites with complex microstructures. In addition to the studies conducted in this work, this framework lays the groundwork for continued research of these materials. In addition to implementing an oxidation model, the framework was also used to implement strategies that expedited the simulation of oxidation in textile composites so that it would take only a few hours instead of impractically long times. Finally, a coupled diffusion/oxidation and damage progression analysis was implemented that was used to study the mechanical behavior of textile composites under mechanical loading as well as oxidation.

15. SUBJECT TERMS

16. SECURITY CLASSIFICATION OF:			17. LIMITATION OF ABSTRACT	18. NUMBER OF PAGES	19a. NAME OF RESPONSIBLE PERSON
a. REPORT	b. ABSTRACT	c. THIS PAGE			
unclassified	**unclassified**	**unclassified**		**154**	

Table of Contents

1. Introduction

This section will provide an introduction to the oxidation of textile composites. The general challenge of characterizing damage due to environmental conditions will be discussed, in particular the effect of a high-temperature oxidizing environment. The development of a multiscale/multiphysics finite element program will also be discussed which will provide the user with tailored tools for textile composite analysis that do not exist in commercial software. In particular, the challenge of simulation of oxidation in textile composites and the coupling of oxidation and mechanical damage will be addressed. A proposed framework for the coupling is presented.

1.1. Damage due to environmental conditions

Woven composite structures are expected to undergo a range of hygrothermal and oxidizing environmental conditions during their service life. Environmentally induced degradation of textile composites has been examined experimentally. However, the characterization is typically macroscopic. For example, Luan et al. [1] studied the corrosion of a C-SiC composite with SiC coating (SiC-C/SiC) under a low frequency cyclic stress in various gas atmospheres of oxygen, water vapor, and sodium sulfate vapor at temperatures from 1000 to 1300 °C. A model for the cyclic stress corrosion mechanism of the composite was proposed from the experimental study and an equation to predict the lifetime of the composite under cyclic stress conditions was derived from the model. Hale [2] characterized the strength reduction of three GRP composite materials as a function of temperature and testing environment (sea water and crude oil condensate). In neither case were the microscopic damage mechanisms considered.

Haque and Rahman [3] investigated the damage development in woven ceramic matrix composites under tensile and cyclic loading at elevated temperatures. The tensile strength of SiC/SiNC woven composites was found to increase with increased temperatures up to 1000°C. Elevated temperature was found to have a remarkable effect on the fatigue strength. At 700°C, the fatigue strength was approximately 50 percent of the ultimate strength, while at 1000°C it was found to be less than 20 percent of the ultimate strength. They developed rate equations for modulus degradation and life prediction under fatigue loading at room and elevated temperatures which fitted well with the experimental results. In some cases, the success of the application itself depends on the ability of the composite to withstand environmental conditions. For example, cryogenic propellant tanks fabricated using composites need to be able to avoid leakage of the propellant through the micro cracks in the composite material. Peddiraju et al [4] simulated the leakage of gaseous hydrogen through the thickness of a damaged composite laminate and predicted the leakage rate at room and cryogenic temperatures.

Polymer matrix composites absorb moisture during service. This can lead to plasticization of the polymer matrix, alter the stress state and degrade the fiber/matrix interface [5-7]. Due to this, a good understanding of the moisture absorption and desorption behavior is important for predicting long-term material and structural performance. Some good work has been put in to investigating the thermal conductivity and moisture diffusion behavior of polymer matrix woven composites. Dasgupta and Agarwal [8] studied the thermal conductivity of plain weave

composites using a homogenization technique and were able to achieve very good agreement with the experimental results. Roy et al. [9] examined the effect of preexisting matrix-cracks on the moisture diffusion behavior of a 5-harness satin weave composite using a continuum damage mechanics approach based on the theory of irreversible thermodynamics. Li et al. [10] investigated the moisture diffusion behavior in hybrid woven composite laminates using a simple 1D diffusion model to simulate the effect of stacking sequence of woven plies on the diffusion behavior. Tang et al [11] studied the effect of tow architecture on the diffusion behavior in woven composites. This helps in identifying the dominant architectural factors that affect the diffusion behavior of a polymer matrix woven composite. Their analysis consisted of two steps – calculating the effective diffusivity of the fiber tows with matrix and then using these properties to model the tow with the corresponding tow architecture in the woven composite. The effective diffusivity of the tows was calculated using 3D finite element micromechanics [12]. The effect of irregular fiber distribution was taken into account using a finite element based 'bi-zone' model [13]. Simulations of moisture diffusion tests for a 3-ply woven hybrid composite were performed and found to be in close agreement with experimental results.

1.2. Effect of oxidation

Oxidation at high temperature has been a concern for a long time. Of course, the definition of high temperature depends on the material system. Carbon fiber-reinforced silicon carbide composites (C–SiC) exhibit excellent mechanical properties at temperatures below 1650°C and have been designed and developed for high-temperature applications such as the high thrust-to-weight ratio turbine engines and reentry thermal protection for spacecraft. However, the mismatch in thermal expansion coefficients between the carbon fiber and the SiC matrix induce matrix and seal coating microcracking during cooling from the processing temperature [14]. These cracks allow for oxygen to leak in and react with the carbon fibers at temperatures above 400 °C [15-17]. This oxidation in turn will degrade the mechanical properties of the composite. Luan et al [18] examined C-SiC composites being oxidized or corroded in various gas atmospheres and found that oxygen was the major factor degrading the composite under conditions with cyclic stresses. They proposed a model for the cyclic stress corrosion mechanism from the experimental results as well as an equation to predict the lifetime of the composite. Halbig et al [19] studied oxidation tests of C/SiC composites at elevated temperatures and developed a model that simulates the diffusion of oxygen into a matrix crack bridged by carbon fibers.

Carbon-carbon composites are designed for extremely high temperatures, but they must be protected from oxidation. Various researchers have studied the behavior of carbon-carbon and proposed schemes for oxidation protection. Ceramic coatings alone do not provide a comprehensive barrier against oxidation because of the mismatch between the coefficients of thermal expansion. Due to this mismatch, cracks form in the coatings. As an additional form of protection, particulates are added to the matrix [20]. These 'inhibitor' particulate materials are usually boron, boron carbide or silicon carbide. Ochoa and Elliott [21] studied oxidation under isothermal, cyclic thermal, and thermo-mechanical fatigue conditions for inhibited carbon-carbon composites. Mass loss and material property degradation assessment was undertaken with subsequent exploratory nondestructive testing utilizing dynamic mechanical analysis (DMA) and piezoelectric ultrasonic composite oscillator technique (PUCOT) techniques. Degradation in

shear and axial moduli were measured as oxidation progressed. Lou et al. [22] examined the effect of additives on the mechanical properties of oxidation-resistant carbon/carbon composites (C/C). The additives used in their test included silicon carbide, silicon nitride, and metal borides. These additives resulted in large increases in flexural modulus and strength. Recently Mazany et al [23] filed a patent on oxidation inhibition of carbon-carbon composites. Their invention involves two steps: (a) contacting the carbon-carbon composite with an oxidation inhibiting composition composed of phosphoric acid or an acid phosphate salt, at least one aluminum salt, and at least one additional metal salt and (b) heating the carbon-carbon composite at a temperature sufficient to form a deposit from the oxidation inhibiting composition within at least some of the penetrated pores of the carbon-carbon composite.

Schoeppner, Pochiraju and Tandon [24] developed a multidisciplinary approach aimed at predicting the performance of high-temperature polymer matrix composites (HTPMCs). HTPMCs are used in a variety of aerospace applications. Pochiraju et al have performed an extensive review of the state of the art in predicting thermo-oxidative degradation and performance of HTPMCs[25]. Unfortunately, there is still much more research required and all the underlying mechanisms for the predicting the behavior of these materials are yet to be determined. Characterizing the behavior of these materials is not trivial [27-29] and very time-consuming and in some cases, reliable methods to determine certain properties do not yet exist. Pochiraju et al also reviewed the effect of oxidation and aging on the fibers as well as composite behavior. Tandon et al [24] characterized the behavior of neat PMR-15 resin and developed a model to predict the thermo-oxidation of the material. Thermo-oxidative aging was simulated with a diffusion reaction model in which temperature, oxygen concentration and weight loss effects were considered. The model which was implemented using FEM considered diffusion, reaction and oxidation of the resin system. The model developed by Pochiraju et al [24-26] is used as the basis for the oxidation model developed in this work and is discussed in detail in Section 3. They also used the finite element method (FEM) to model the oxidation behavior in a Graphite/PMR-15 composite [26], where they assumed the fiber did not oxidize. The oxidation model developed by Pochiraju et al tends to be very computationally intensive and most of their analyses were performed at the fiber/matrix scale. Pochiraju et al [30] also used the oxidation model to predict the evolution of stresses and deformation in HTPMCs by accounting for thermo-oxidation induced shrinkage. The oxidation model and the non-linear elastic deformation analyses are coupled using information obtained by experimental observation of shrinkage in neat PMR-15 resin under aging in oxygen and argon.

Roy et al [31] developed a multi-scale model based on micromechanics and continuum damage mechanics to simulate the accelerated fiber-matrix debond growth in a unidirectional HTPMC undergoing oxidation. The model was used to predict the mechanical behavior of a laminate in a three-point bending test incorporating the damage caused due to oxidation. Wang and Chen [32] developed a computation micromechanics approach based on irreversible thermodynamics to obtain constitutive properties of HTPMCs while tracking thermo-oxidative reactions, microstructural damage and thermo-mechanical loading. A two-scale homogenization theory is also used to determine macroscopic behavior of these composites. They also stressed the need for many not yet available thermal, chemical, mechanical and interphase properties and microstructural parameters in order to accurately predict the behavior of HTPMCs.

1.3. Development of multiscale/multiphysics finite element framework

There are many commercial and public domain software packages for finite element analysis. However, they are typically not designed for the particular challenges one will face when performing detailed 3D analysis of textile composite structures. Textile composites have multiple microstructural scales – the fiber/matrix scale, the lamina scale, and the laminate scale. This complex microstructure of textile composites makes it necessary to use multiscale analyses in order to obtain detailed information about their behavior. Moreover the proposed work also studies the behavior of textile composites under oxidizing environments. This requires a multiphysics analysis that couples damage progression analyses with oxidation simulations. These sorts of novel analysis methods are not convenient to implement in commercial FEA packages due to the restrictive nature of these software.

A finite element analysis framework called 'BETA' has been developed, which is a successor to the existing in-house finite element code, "ALPHA". Alpha has been used for static linear and nonlinear thermo-mechanical analysis and transient diffusion analysis of textiles. Existing tools formed the foundation of the BETA finite element framework. Although the existing code was designed to be quite modular and extensible, experience has shown that the needs of those performing detailed analysis of textiles is quite severe. The new framework has several enhancements over the existing in-house code in order to meet the needs of the proposed work. The goal is to design a robust framework that can be enhanced and extended in the years to come by future users and lives beyond the term of this research work. Towards this end, the software has been designed using an object oriented philosophy. This incorporates features such as inheritance, polymorphism, data abstraction and encapsulation. When designed properly, this kind of programming philosophy makes it easier and more convenient to maintain, manage, modify, extend and enhance a large software package.

The new framework makes use of the latest hardware improvements such as multi-processor machines which are very common now. The framework will also be portable so that it can be used on both the Windows as well as UNIX/LINUX environments. The developed framework can be used to analyze different configurations including textile composites subjected to a high temperature oxidizing environment. The framework includes tools for geometric description, including spatial variation of material properties, mesh development, finite element solver, and postprocessing. It also provides better control of output for debugging algorithms and postprocessing of results. A more detailed description of the framework is given in Ref.[33].

1.4. Simulation of oxidation in textile composites

Composite structures are increasingly being used for high temperature applications in the aerospace industry. The extreme operating environments that these materials are subjected to can lead to chemical degradation including oxidation. It is important to understand the behavior of these materials under these conditions so that they can be designed better and provide increased performance. A focal problem that is investigated in this work is the effect of oxidation on the mechanical behavior of textile composites. This will involve a coupled damage progression analysis that accounts for the effect of oxidation on the engineering properties of the composite.

A precursor to the coupled damage progression analysis is the oxidation analysis of the composite which is quite complex because in reality the fiber and matrix both have their own

response to high temperature oxidation and aging. In addition, when the two are combined to form the composite, the anisotropic oxidative response is even more complex to simulate because of the fiber-matrix microstructure. Micro-cracks and damage formed at the interface between the fiber and matrix affect the oxidative response of the composite. The task of simulating oxidation of textile composites requires a combination of various strategies. The underlying oxidation model is adopted from the work by Pochiraju, Schoeppner and Tandon[24-26] who have used their model to simulate the oxidation of neat PMR-15 resin with reasonable accuracy compared to experimental observations. The oxidation behavior is represented using a set of transient nonlinear governing equations based on the conservation of mass equation for diffusion. The oxidation model will be implemented using the finite element framework that is developed as part of this work. The finite element formulation imposes limitations on the element size and the time step size which make the simulation computationally intensive. New strategies have been developed in order to expedite the oxidation analysis. Moreover, it is not practical to discretely model the fibers in the textile composite. Strategies for determining effective oxidative properties have been developed and validated. The overall goal of this work has been to develop an efficient analysis strategy that can simulate the oxidation behavior in textile composites in a reasonable time frame.

1.5. Prediction of Damage in textile composites under oxidation

The overall goal of this work is to use a finite element framework to analyze damage progression in textile composites due to the combined effects of oxidation under high temperature and mechanical loads. Determining the effect of high temperature oxidation and aging on the mechanical behavior of composites is a very complex and challenging problem. There are a number of studies in the literature investigating the different time-dependent physical, chemical and mechanical damage mechanisms [25,34-36] as well as experimental characterization studies[37-42]. But there is still much more work that needs to be done in order to reliably predict the composite behavior using mechanistic approaches. The damage progression analysis involves performing an oxidation analysis that simulates the diffusion of oxygen into the composite and tracks how much the material has oxidized. The simulation of oxidation in the textile composite is one of the goals of this work and is discussed in the previous section.

The analysis is a one-way coupled problem where the oxidation is assumed to affect the mechanical behavior of the material and not vice versa. A constitutive theory is used to determine the amount of damage in terms of strength or stiffness degradation based on the oxidation state of the material in the composite. Figure 1.1 shows a schematic that illustrates the coupled analysis. Both the oxidation analysis as well as the damage progression analysis needs to account for the multiple microstructural scales in the composite. The damage will not affect the oxidation properties in the current implementation. The progressive damage analysis will track the damage state in the composite and calculate the stress state in the composite with respect to time as the oxidation progresses.

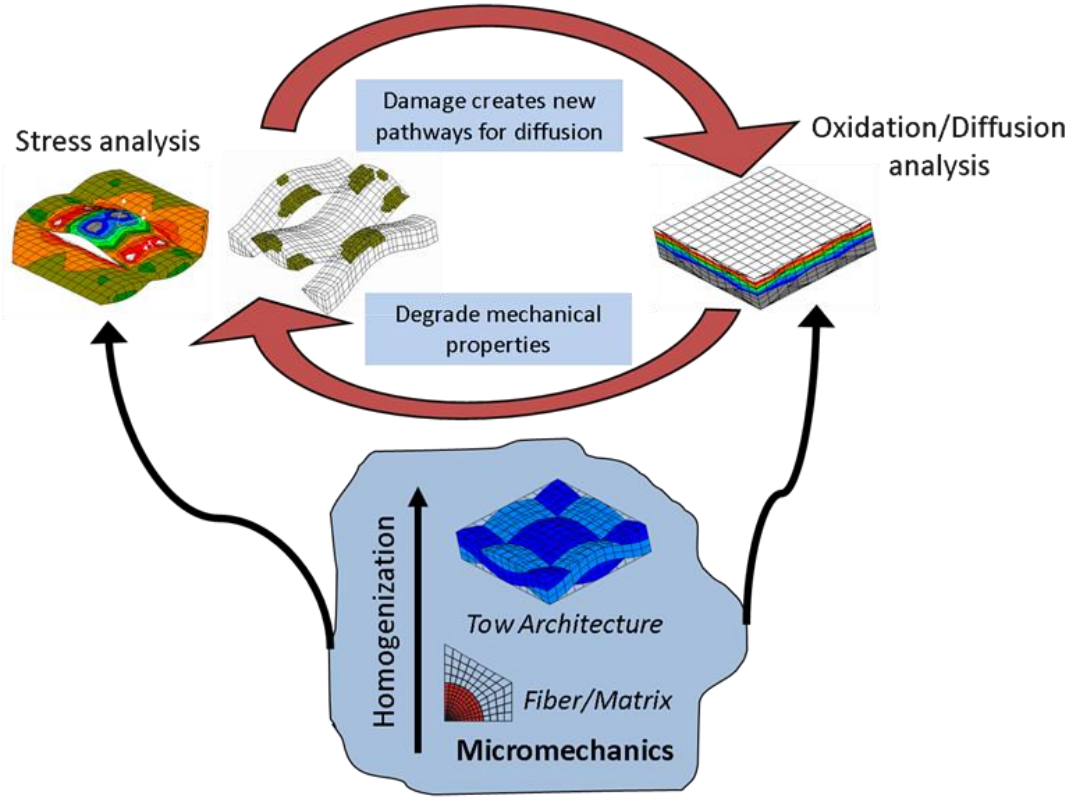

Figure 1.1: Schematic illustrating coupled oxidation/thermo-mechanical

The coupled analysis model is used to investigate a focal problem. The focal problem chosen for this work is a Graphite/PMR-15 plain weave composite laminate that is loaded uniaxially to a particular strain level and then the top and bottom surfaces are exposed to oxygen for 200 hours. The laminate in the simulation is assumed to be at 288 C. A parametric study was performed to study the effect of the number of plies in the laminate on its mechanical behavior. This analysis model lays the groundwork for fully coupled simulations of the behavior of textile composites under combined mechanical loading and oxidation.

In summary, this research will focused on the following:

1) Develop a coupled analysis model using the finite element framework that will couple the oxidation analysis and the damage progression analysis.

2) Develop a constitutive model to simulate the effect of oxidation on the mechanical properties of the tow and matrix.

3) Use the coupled analysis model to analyze a focal problem

a) Simulate mechanical behavior of a Graphite/PMR-15 plain weave laminate under oxidation.

b) Perform a parametric study on the effect of the number of plies on the mechanical behavior of the configuration.

1.6. Summary

This section discussed damage due to environmental conditions, in particular oxidation. For the oxidation analysis described in this work, a user-developed finite element framework provides the flexibility and freedom to implement the required model. This section also provided a literature review that detailed briefly the challenges and accomplishments involved in predicting the effect of environmental conditions on the behavior of composites. The overall goal of this work is to develop a multiscale/multiphysics analysis framework that can be used to study the mechanical behavior of textile composites under oxidation. Section 2 will describe the architecture of woven composites, and the particular configurations of interest in this study. Section 3 will describe the theory and formulation of an oxidation model that is used with FEM. Section 4 will provide the basic algorithm for implementing the oxidation model into a finite element program. Section 5 will discuss strategies that were employed to expedite analysis, and Section 6 will present validation of these strategies. Section 7 presents homogenized oxidation properties obtained through analysis. The infeasibility of discretely modeling composites on the fiber-matrix scale necessitates the use of homogenized properties. Section 8 presents results for oxidation analysis of a plain weave textile composite. Section 9 presents results for an oxidation-damage analysis with a one-way coupling. Finally, Section 10 will present conclusions and possible future work.

2. Configurations of Interest

Textile composites are commonly utilized in high performance structural applications such as those in the aerospace industry. Such materials exhibits higher strength-to-weight ratios than traditional metallic materials. Furthermore, the use of the textile architecture can ease in the manufacture and layup of composite structures compared to that of one dimensional laminates. However, this advantage is accompanied by an increased complexity in the response of the material due to the more complex architecture compared to tape laminates. A variety of weave types exist with varying complexities. This section will discuss weave types in general and focus on details of a plain weave composite. Furthermore, modeling of a textile composite on a fiber-matrix scale is impractical from a computational point of view. Thus, homogenized properties of a tow should be developed such that the woven architecture may be modeled discretely on a tow-matrix scale while still characterizing the behavior of the actual composite material.

2.1. Weave types

Textile composites provide a more effective manufacturing process compared to tape laminates and a range of weave architectures exist. Figure 2.1 shows a variety of weave types that may be considered for a textile composite. The plain weave type is relatively simple, while the various harness satin weaves and twill weaves have a more complex architecture. These weaves are considered two-dimensional in the sense that there is no through-thickness stitching or weaving of tows. However, it should be made clear that two-dimensional weave types do have a three-dimensional spatial variation of architecture. Due to the relative simplicity of the architecture, the plain weave composite was selected for this study. This weave type also has a much smaller repeating unit cell that serves to significantly reduce the size of the problem being analyzed.

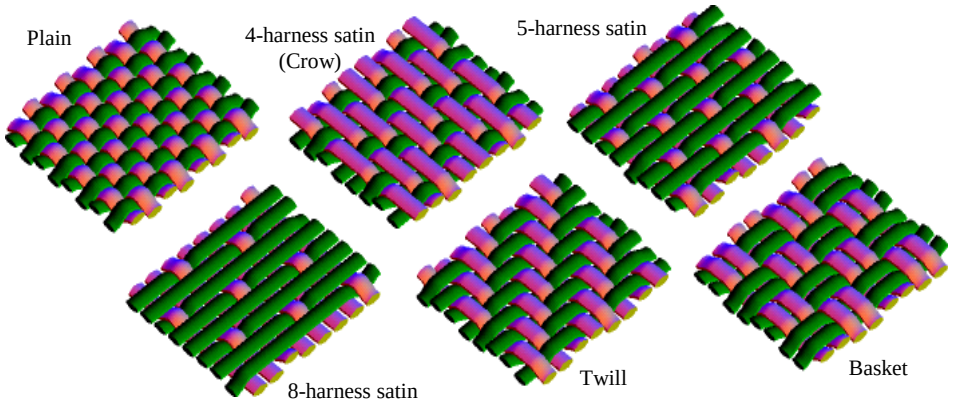

Figure 2.1: Examples of weave types utilized in textile composite materials

2.2. Description of the plain weave unit cell

The relative simplicity of the plain weave unit cell makes it an ideal candidate for studying the effect of a thermo-oxidative environment on textile composites. This section describes the physical dimensions, waviness ratio (WR), and tow volume fractions for the plain weave configuration. Waviness ratio is defined herein as the thickness (h) of a woven mat divided by the wavelength (λ) of the undulation of a tow. A composite laminate can be constructed by the duplication and translation of a basic unit cell (see Figure 2.2). The matrix is shown transparent in the figures to reveal the tow architecture. The term *M* will represent the basic unit cell for a simply stacked plain weave. The term $\bar{M}$ will represent the mirror of *M* about $x_3 = h$. Therefore, a symmetrically stacked unit cell may be denoted by the stacking sequence $[\bar{M} / M]$. In all cases the plain weave tow undulation was sinusoidal and the cross-section was lenticular with sinusoidal shaped boundaries. For the configuration considered in this study a waviness ratio of 1/3 and fiber volume fraction of 55.6% were utilized.

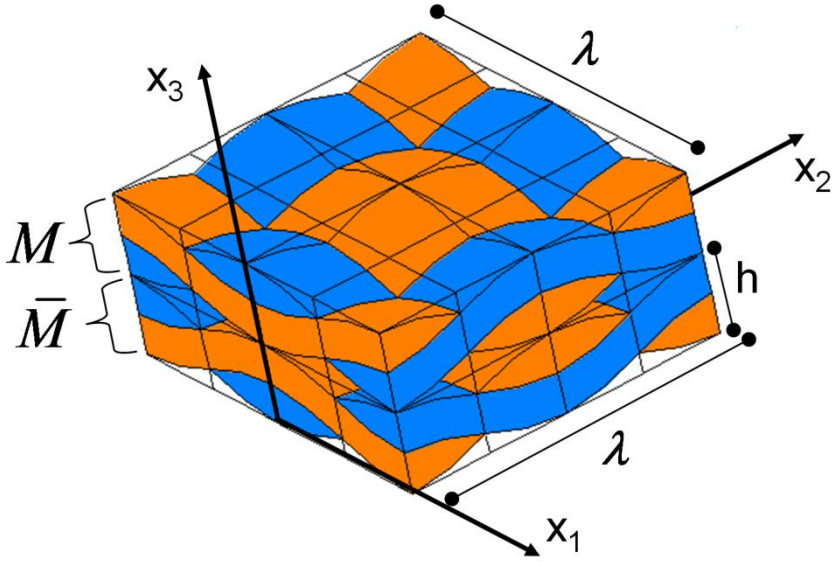

Figure 2.2 Description of plain weave unit cell

2.3. Description of the fiber-matrix unit cell

The woven architecture for a plain weave composite is well defined in the previous section. However, in reality the tows are composed of discrete fibers and matrix which are impractical to model in the woven configuration. Thus, effective properties for the tows are determined by the consideration of a fiber-matrix unit cell which may be duplicated and translated to produce the configuration of a tow. Figure 2.3 illustrates the multi-scale analysis involved when considering textile composites. The particular fiber volume fraction may be accounted for by increasing the size of the fiber relative to the surrounding matrix. For lower fiber volume fractions a square unit cell is sufficient. However, for higher fiber volume fraction with closer packing of fibers a hexagonal unit cell is necessary. For this study a square array of fibers was used to obtain

homogenized/effective properties of the tows. The process of obtaining and validating effective properties is discussed in Section 7 of this report.

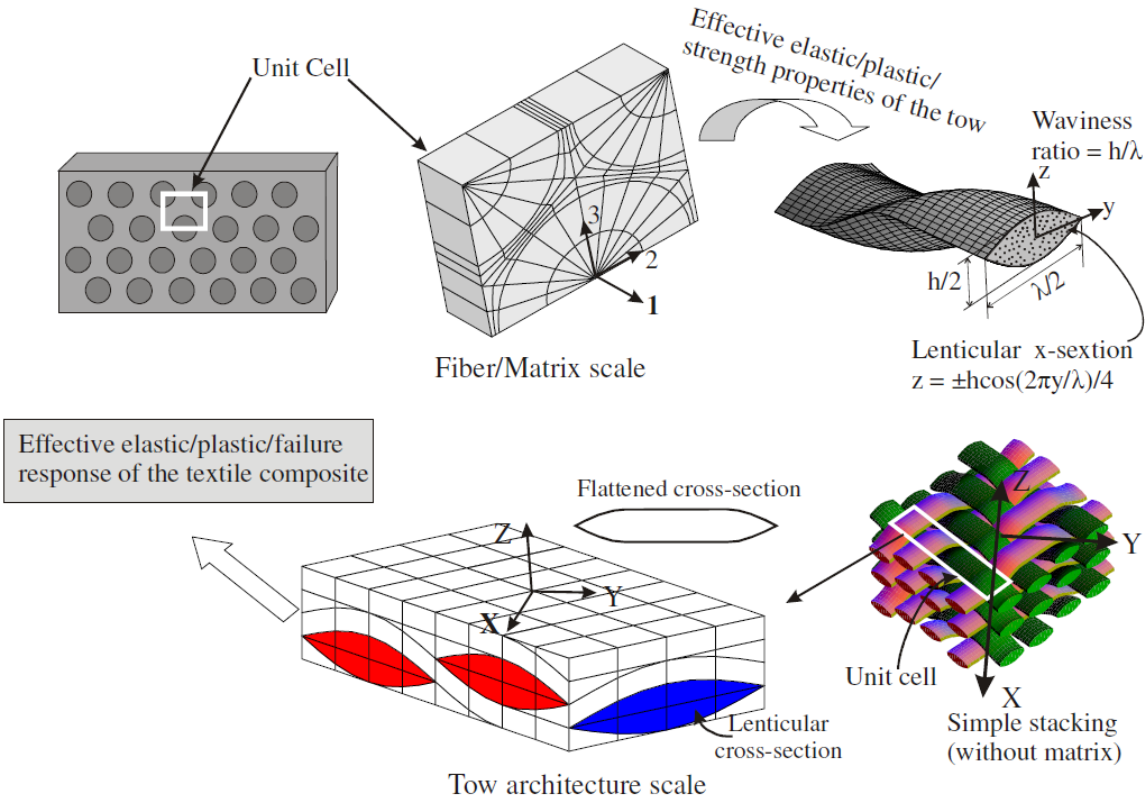

Figure 2.3: Multi-scale analysis of textile composites

2.4. Summary

This section has presented a variety of weave types commonly utilized in textile composites. A plain weave type was chosen for the relative simplicity of the architecture and the ability to significantly reduce the problem size at hand for the oxidation analysis of the configuration. The parameters used to describe the plain weave unit cell were explained. The necessity of considering a fiber-matrix unit cell was explained, and the usage of these configurations are explained later in this report.

3. Theory and Formulation

This section discusses the theory and formulation for diffusion and oxidation using finite element analysis. The general issue of boundary conditions for periodic microstructures is discussed as well as an algorithm for addressing damage initiation and growth. Then the theory and finite element formulation for diffusion and oxidation are discussed in detail. An approach for the coupling of oxidation to mechanical analysis is presented, and constitutive relationships are discussed.

3.1. Boundary conditions for periodic microstructures

Periodic configurations can be analyzed by using a representative volume element (RVE) or unit cell. They can also be used to obtain effective properties for the periodic configuration or microstructure. The unit cell is a region within the microstructure which can be used to generate the entire microstructure by just duplication and translation of the unit cell. Once the unit cell is chosen for the periodic microstructure, the certain characteristics can be determined based on the fact that each of the unit cells will behave in the same manner. For elasticity, the periodic conditions state that the displacement of one unit cell differ from the other unit cells only by a constant offset, which depends on the volume averaged displacement gradients [43-4]. Furthermore the strains and stresses are identical in all of the unit cells. This can be expressed as

$$u_i\left(x_\alpha + d_\alpha\right) = u_i\left(x_\alpha\right) + \left\langle \frac{\partial u_i}{\partial x_\beta} \right\rangle d_\beta \tag{3.1}$$

$$\varepsilon_{ij}\left(x_\alpha + d_\alpha\right) = \varepsilon_{ij}\left(x_\alpha\right) \tag{3.2}$$

$$\sigma_{ij}\left(x_\alpha + d_\alpha\right) = \sigma_{ij}\left(x_\alpha\right) \tag{3.3}$$

where d_α is a vector of periodicity [43-44]. The vector of periodicity is a vector from a point in one unit cell to an equivalent point in an adjacent unit cell.

Additional computational savings can be obtained by exploiting symmetries within the unit cell [43]. The periodic boundary conditions and symmetry conditions are imposed by using multi-point constraints in the finite element analysis.

3.2. Damage initiation and progression

The damage progression analysis performed in this work is based on a continuum damage strategy. This strategy degrades the strength or stiffness of a material point in

the finite element mesh based on the failure criteria for the material point. The damage analysis differs with respect to linear elastic analysis lies in how the constitutive relations evolve as the load on the configuration changes. This section will describe the algorithm for the damage progression analysis used in this work followed by the failure criteria and the property degradation scheme used.

All the analyses performed in this work assume that the configuration is loaded with an increasing strain load. Figure 3.1 shows the flowchart for the algorithm used in this work. The configuration is assumed to behave linearly until damage is initiated. The failure criterion can be used to determine the load at which damage initiates. This is done by applying an arbitrary load on the model and calculating the expressions in the failure criterion. Since the model is initially linear elastic until the first instance of damage, it is possible to calculate the initial failure load by scaling the load to the point where failure is just triggered. The configuration is then loaded with a load that is a small fraction larger than the load at which damage initiated. This is done to ensure that round-off errors during the numerical calculations do not affect the simulation. This ensures that the load is increased to a value that definitely causes new damage to occur. This point in the algorithm can be considered the beginning of a new load step. The displacement field corresponding to this load is solved for, by assuming that no damage has initiated yet.

The displacement field is used to apply the failure criterion at all the Gauss quadrature (or integration) points. For all the locations that damage is found, the mechanical properties at that integration point are degraded based on the property degradation scheme. The model is solved for the new displacement field based on the new material properties at each integration point. The model is checked again for damage and this procedure is repeated until no new damage is detected. The next step before moving on to the next load step is determining the load for the next load step. Since we have converged to a damage state for this current load step, the configuration can be likened to a new linear elastic material till the load is increased and new damage is found. Thus, just as the load for initial failure was determined, the load value for the next occurrence of new damage is determined using the failure criteria. In this manner, the load is increased and the simulation proceeds through the load steps until a specified maximum strain load is reached. Throughout this process, the damage state is recorded and new damage is tracked as the load on the configuration is increased. Other post-process data such as the volume averaged stresses and strains are also recorded. Figure 3.2 gives a schematic of what the stress-strain response would look like as the simulation progresses. The following sections describe the failure criteria and the property degradation scheme that were used in this work.

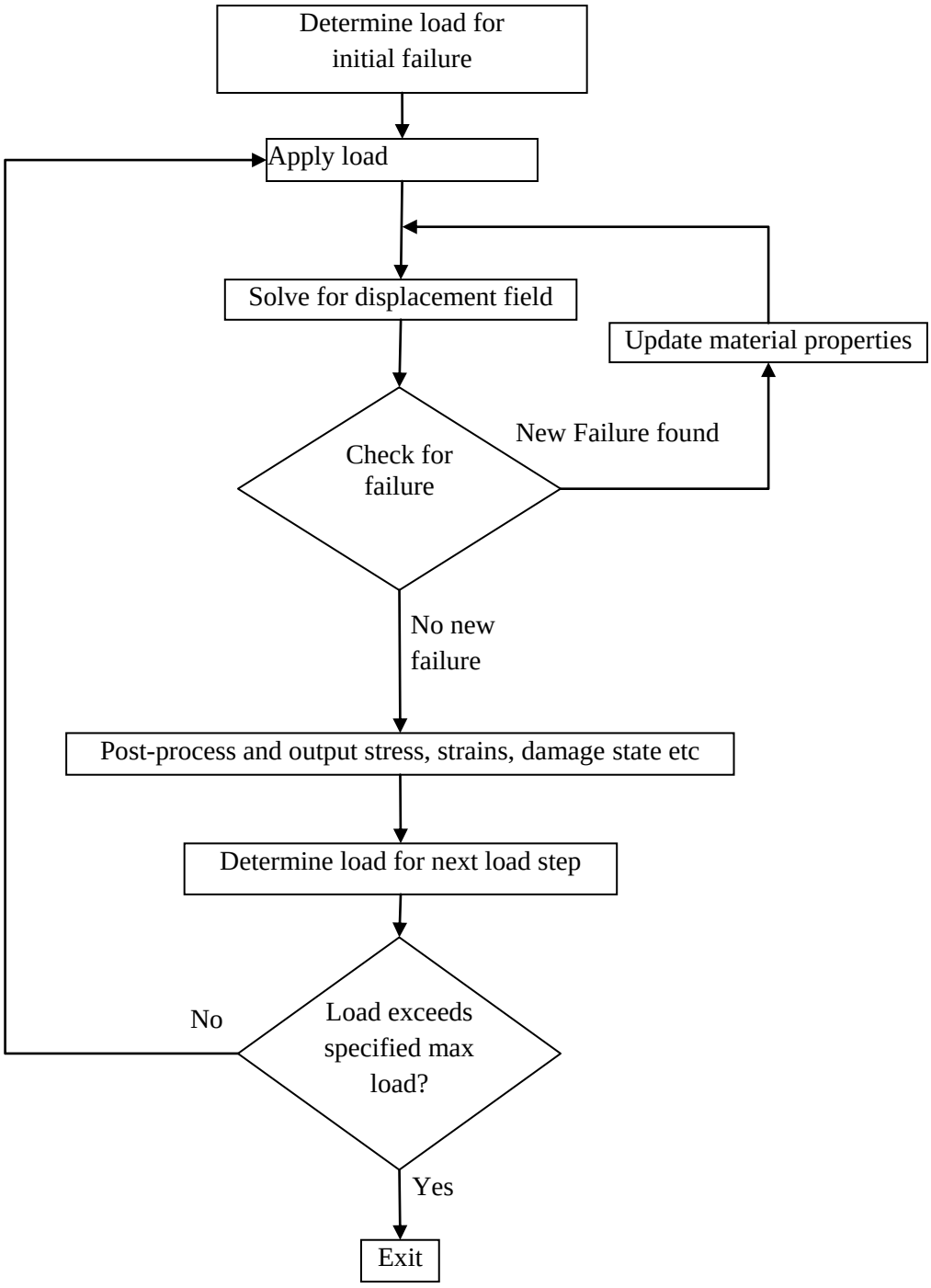

Figure 3.1: Flowchart for damage progression analysis

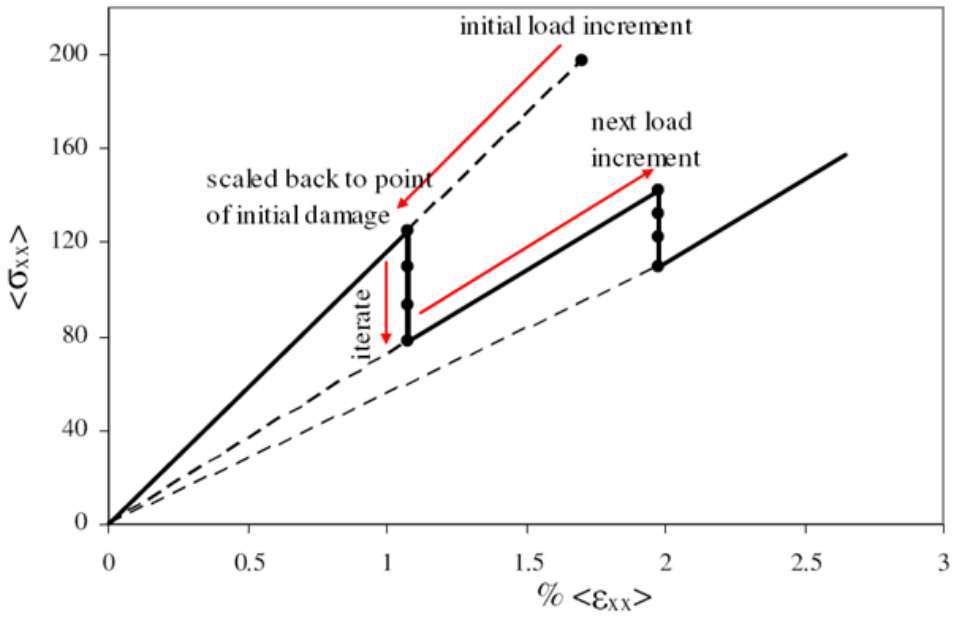

Figure 3.2: Schematic of stress-strain response

3.2.1. Failure criteria

There are various failure criteria such as the maximum strain criterion and the maximum stress criterion. Any of these criteria or a combination of these criteria can be used in the damage progression analysis. For the analyses in this research work, the maximum stress failure criteria are used. This means that failure has occurred when any of the stress components in the material coordinates has exceeded its corresponding strength, i.e. when $\sigma_{ij} / S_{ij} > 1$ where σ_{ij} is the stress component in the material coordinates and S_{ij} is the corresponding strength for σ_{ij} . Section 9 gives a detailed description of the failure criteria that are utilized to simulate the microscopic damage progression in this work.

3.2.2. Property degradation scheme

Typical property degradations models degrade the engineering properties whenever failure is detected. Some degradation models look at the properties (such as stress, strain) at the center of the element. In this work, the failure criteria and property degradation scheme is applied on each integration point of all the elements in the model. The stresses and strains at any material point in the material coordinate system are related by Hooke's law given by Eq.(3.4). The compliance matrix for an orthotropic material is given by Eq.(3.5).

$$\sigma_i = C_{ij}(\varepsilon_i - \varepsilon_i^t)$$
$$or\ \varepsilon_i = S_{ij}\sigma_i + \varepsilon_i^t \tag{3.4}$$

$$S_{ij} = \begin{bmatrix} \frac{1}{E_{11}} & \frac{-\upsilon_{12}}{E_{11}} & \frac{-\upsilon_{13}}{E_{11}} & 0 & 0 & 0 \\ \frac{-\upsilon_{21}}{E_{22}} & \frac{1}{E_{22}} & \frac{-\upsilon_{23}}{E_{22}} & 0 & 0 & 0 \\ \frac{-\upsilon_{31}}{E_{33}} & \frac{-\upsilon_{32}}{E_{33}} & \frac{1}{E_{33}} & 0 & 0 & 0 \\ 0 & 0 & 0 & \frac{1}{G_{12}} & 0 & 0 \\ 0 & 0 & 0 & 0 & \frac{1}{G_{23}} & 0 \\ 0 & 0 & 0 & 0 & 0 & \frac{1}{G_{13}} \end{bmatrix} \tag{3.5}$$

Let E_{ij}, G_{ij} and υ_{ij} be the original extensional moduli, shear moduli and Poisson's ratio respectively and $\overline{E}_{ij}$, $\overline{G}_{ij}$ and $\overline{\upsilon}_{ij}$ be the degraded extensional moduli, shear moduli and Poisson's ratio respectively. Say, $a_i, (i = 1..9)$ are the degradation parameters, which specify the amount of degradation. Then a typical property degradation scheme will look like:

$$\begin{aligned} &\overline{E_{11}} = E_{11}/a_1, \quad \overline{E_{22}} = E_{22}/a_2, \quad \overline{E_{33}} = E_{33}/a_3 \\ &\overline{G_{12}} = G_{12}/a_4, \quad \overline{G_{23}} = G_{23}/a_5, \quad \overline{G_{13}} = G_{33}/a_6 \\ &\overline{\upsilon_{12}} = \upsilon_{12}/a_7, \quad \overline{\upsilon_{23}} = \upsilon_{23}/a_8, \quad \overline{\upsilon_{13}} = \upsilon_{33}/a_9 \end{aligned} \tag{3.6}$$

For example, if a_1=8, that implies that the E_{11} modulus is decreased by a factor of 8 from its current value if the material point fails. Note that in this general framework, the diagonal as well as non-diagonal entries of the compliance matrix can be affected independently. The specific details of property degradation scheme used in this work including the degradation factors used for the different materials will be given in Section 9.

3.3. Diffusion

This section describes the governing equations and the finite element formulation for simulating the diffusion behavior in materials. The diffusion behavior through heterogeneous materials was analyzed in this work. This section starts by listing the equations for the common analysis procedure. This is followed by the derivation of the weak form and its discretization to obtain the finite element formulation.

3.3.1. Conservation laws

The conservation of mass law for diffusion yields the following equation

$$\frac{\partial C}{\partial t} + \frac{\partial J_i}{\partial x_i} = 0 \tag{3.7}$$

where C is the concentration of diffusing material and J_i is the diffusion flux.

The differential equation described in Eq.(3.7) holds for a material point. When the material being analyzed is homogenous, the concentration field is continuous throughout the domain and can be solved without any modifications. When the governing equation is applied to a configuration that has heterogeneous regions with dissimilar solids, the concentration is generally not continuous across the interface between the different solids. This issue of discontinuous concentrations is addressed in Ref.[12], where a thermodynamic potential is introduced. The thermodynamic potential is considered to be what drives the flow of a diffusing material through another material. This potential is continuous across the material interface and the concentration is then defined as a function of the thermodynamic potential. When this function is assumed to be linear with C=0 when the potential=0, the function is of the form

$$C = a\bar{C} \tag{3.8}$$

where $\bar{C}$ is the thermodynamic potential and *a* is a material property. $\bar{C}$ is assumed to have a range from 0 to 1, which means that the concentration is maximum when the potential has a value of 1. That determines *a* to be the saturation mass concentration of the diffusing material in the solid, denoted by C^{∞}. Therefore, the thermodynamic potential is the concentration in the material normalized by the saturation concentration of the solid, hereafter referred to as the normalized concentration,

$$\bar{C} = \frac{C}{C^{\infty}} \tag{3.9}$$

The governing equation can now be rewritten as

$$C^{\infty}\frac{\partial \bar{C}}{\partial t}+\frac{\partial}{\partial x_i}J_i=0 \tag{3.10}$$

3.3.2. Concentration gradients

Unlike the strain-displacement relationship in solid mechanics, the diffusion analysis uses simple gradients of the concentration, $\frac{\partial C}{\partial x_i}$

3.3.3. Constitutive relations

The relationship between flux and the concentration gradient is given by Fick's first law,

$$J_i=-D_{ij}\frac{\partial C}{\partial x_j} \tag{3.11}$$

where D_{ij} is the 2nd order diffusivity tensor. The Latin subscripts *i* and *j* denote the coordinate direction and range from 1 to 3 for a three dimensional formulation.

When Eq.(3.11) is re-written in terms of the normalized concentration,

$$J_i=-C^{\infty}D_{ij}\frac{\partial \bar{C}}{\partial x_j} \tag{3.12}$$

3.3.4. Boundary conditions

The flux boundary conditions are given by

$$\hat{q}=-n_i J_i \quad \text{on S} \tag{3.13}$$

And the normalized concentration boundary conditions are given by

$$\bar{C}=\overline{C} \text{ on } \hat{S} \tag{3.14}$$

where $\overline{C}$ is the specified normalized concentration on the boundary $\hat{S}$.

3.3.5. Weak form

The equation of conservation mass is multiplied by a variation of the normalized concentration and integrated over the volume to obtain the weighted integral form,

$$\int_V \delta\bar{C}\left[C^\infty \frac{\partial \bar{C}}{\partial t} + \frac{\partial}{\partial x_i} J_i \right] dV = 0 \tag{3.15}$$

where $\delta\bar{C}$ is an arbitrary variation of the normalized concentration.

Integration by parts gives the weak from,

$$\int_V \left[\delta\bar{C} C^\infty \frac{\partial \bar{C}}{\partial t} - \frac{\partial \delta\bar{C}}{\partial x_i} J_i \right] dV + \int_S \delta\bar{C} n_i J_i dS = 0 \tag{3.16}$$

Using Eq.(3.12) and Eq.(3.13) in Eq.(3.16) gives the basis for the finite element formulation,

$$\int_V \left[\delta\bar{C} C^\infty \frac{\partial \bar{C}}{\partial t} + \frac{\partial \delta\bar{C}}{\partial x_i} C^\infty D_{ij} \frac{\partial \bar{C}}{\partial x_j} \right] dV = \int_S \delta\bar{C} \hat{q} dS \tag{3.17}$$

3.3.6. Discretization of weak form and time integration

Over a typical finite element, the normalized concentration is approximated by

$$\bar{C}(x,t) = N_\alpha(x)\bar{C}_\alpha(t) \tag{3.18}$$

where N_α are the interpolation functions and $\bar{C}_\alpha$ are the nodal normalized concentrations. The subscripts with Greek letters range from 1 to the number of interpolation functions.

After discretizing the weak form using Eq.(3.18) and $\delta\bar{C} = N_\alpha \delta\bar{C}_\alpha$, the following set of equations are obtained,

$$\int_V \left[N_\alpha C^\infty N_\beta \frac{\partial \bar{C}_\beta}{\partial t} + \frac{\partial N_\alpha}{\partial x_i} C^\infty D_{ij} \frac{\partial N_\beta}{\partial x_j} \bar{C}_\beta \right] dV = \int_S N_\alpha \hat{q} dS \tag{3.19}$$

In matrix form this can be written as

$$M_{\alpha\beta}\dot{q}_\beta + K_{\alpha\beta} q_\beta = F_\alpha \tag{3.20}$$

where

$$M_{\alpha\beta} = \int_V \left[N_\alpha C^\infty N_\beta \right] dV \tag{3.21}$$

$$K_{\alpha\beta} = \int_V \left[\frac{\partial N_\alpha}{\partial x_i} C^\infty D_{ij} \frac{\partial N_\beta}{\partial x_j} \right] dV \tag{3.22}$$

$$F_\alpha = \int_S N_\alpha \hat{q} dS \tag{3.23}$$

$$q_\alpha = \bar{C}_\alpha \text{ and } \dot{q}_\alpha = \frac{d\bar{C}_\alpha}{dt} \tag{3.24}$$

Note that Eq.(3.19) contains a time derivative term. In order to numerically solve this set of equations, an approximation is used for the time derivative term whereby the solution at a particular instant in time is determined based on the solution history. The following describes this 'time-marching' procedure used to numerically solve Eq.(3.19). For the sake of convenience, the following generally uses matrix notation and dispenses with the indices. Let the subscript *s* denote the solution at time *s* and the subscript *s+1* denote the solution at time $s + \Delta t$. Using Eq.(3.20), the following equations can be written for two consecutive time steps, $t=t_s$ and $t=t_{s+1}$,

$$M\dot{q}_s + K_s q_s - F_s = 0 \tag{3.25}$$

$$M\dot{q}_{s+1} + K_{s+1} q_{s+1} - F_{s+1} = 0 \tag{3.26}$$

Using the alpha family of approximations[45] gives

$$(1-\alpha)\dot{q}_s + \alpha\dot{q}_{s+1} = \Delta q / \Delta t \tag{3.27}$$

Multiplying Eq.(3.27) by ΔtM gives

$$(1-\alpha)\Delta tM\dot{q}_s + \alpha\Delta tM\dot{q}_{s+1} = M\Delta q \tag{3.28}$$

Rearranging the terms in Eq.(3.28) gives an expression for $\alpha\Delta tM\dot{q}_{s+1}$

$$\alpha\Delta tM\dot{q}_{s+1} = M\Delta q - (1-\alpha)\Delta tM\dot{q}_s \tag{3.29}$$

Multiplying Eq.(3.26) throughout by $\alpha\Delta t$ gives

$$\alpha\Delta t M\dot{q}_{s+1} + \alpha\Delta t\left[K_{s+1}q_{s+1} - F_{s+1}\right] = 0 \tag{3.30}$$

Substituting Eq.(3.29) into Eq.(3.30) gives,

$$M\Delta q - (1-\alpha)\Delta t M\dot{q}_s + \alpha\Delta t\left[K_{s+1}q_{s+1} - F_{s+1}\right] = 0 \tag{3.31}$$

And substituting for $M\dot{q}_s$ from Eq.(3.25) in Eq.(3.31) gives the governing equations

$$M\Delta q - (1-\alpha)\Delta t\left[-K_s q_s + F_s\right] + \alpha\Delta t\left[K_{s+1}q_{s+1} - F_{s+1}\right] = 0 \tag{3.32}$$

Using

$$a1 = \alpha\Delta t \tag{3.33}$$

$$a2 = (1-\alpha)\Delta t \tag{3.34}$$

in Eq.(3.32) gives

$$M\Delta q - a2\left[-K_s q_s + F_s\right] + a1\left[K_{s+1}q_{s+1} - F_{s+1}\right] = 0 \tag{3.35}$$

Assuming that the diffusivity does not change with respect to time, we have

$$\left[K_{s+1}\right] = \left[K_s\right] \tag{3.36}$$

Using Eq.(3.36), Eq.(3.35) can be re-written as

$$M\Delta q - a2\left[-K_s q_s + F_s\right] + a1\left[K_s q_s + K_s\Delta q - F_{s+1}\right] = 0 \tag{3.37}$$

Rearranging to bring all the terms involving the unknowns to the left side gives

$$\left[M + a1K_s\right]\Delta q = -(a1+a2)\left[K_s q_s\right] + a2\left[F_s\right] + a1\left[F_{s+1}\right] \tag{3.38}$$

Eq.(3.38) is solved to obtain the solution for the *s+1* time step. Therefore, the finite element formulation for this diffusion model can be described by the following equations

$$\bar{M}\Delta q = \bar{F} \tag{3.39}$$

where

$$\bar{M} = \left[M + a1K_s\right] \tag{3.40}$$

$$\bar{F} = -(a1+a2)\left[K_s q_s\right] + a2\left[F_s\right] + a1\left[F_{s+1}\right] \tag{3.41}$$

3.3.7. Boundary conditions for diffusion of periodic microstructures

Periodic configurations can be analyzed by using just a representative volume element (RVE) or unit cell. Similar to how solid mechanics models can be homogenized, RVE models of periodic microstructures can also be used to obtain effective diffusivities. One noticeable difference with the solid mechanics models described in the earlier sections is that they deal with static mechanics whereas the diffusion model described in the previous section simulates a transient behavior. In order to calculate the effective diffusivities, the concentration distribution in the model at steady-state conditions is required. This means that the transient part of Eq.(3.17) is omitted making it a static model.

Once the unit cell is chosen for the periodic microstructure, certain characteristics can be determined based on the fact that each of the unit cells will behave in the same manner. For diffusion at steady-state, the periodic conditions state that the concentration gradient and flux distributions are identical in all of the unit cells. This can be expressed as

$$C\left(x_\alpha + d_\alpha\right) = C\left(x_\alpha\right) + \left\langle \frac{\partial C}{\partial x_\beta} \right\rangle d_\beta \tag{3.42}$$

$$\frac{\partial C}{\partial x_i}\left(x_\alpha + d_\alpha\right) = \frac{\partial C}{\partial x_i}\left(x_\alpha\right) \tag{3.43}$$

$$q_i\left(x_\alpha + d_\alpha\right) = q_i\left(x_\alpha\right) \tag{3.44}$$

where d_α is a vector of periodicity [43-44]. The vector of periodicity is a vector from a point in one unit cell to an equivalent point in an adjacent unit cell.

The configurations analyzed in this work are in general heterogeneous and as mentioned in the previous section, continuity of the normalized concentrations is imposed in order to resolve the issue of discontinuous concentrations at the interface of two different base materials. Therefore all the formulations and models are defined based on normalized concentrations, $\overline{C}$. The actual concentrations can of course always be calculated using Eq.(3.9). In some ways this is different from the typical homogenization procedure in solid mechanics. The primary variable in solid mechanics is displacements whereas in diffusion, the typical primary variable is concentration, which is generally discontinuous across different base materials. This, as mentioned earlier necessitates the use of normalized concentrations, which is continuous across different base materials. To explain the subtle differences when dealing with normalized concentrations, the procedure to determine the effective diffusivity properties of a composite with circular fibers in a periodic square array is described. This procedure is also used to perform some of the analyses in this work.

The approach described herein is consistent with Whitcomb and Tang's work[137] but some notations have been changed to make it clearer. Consider a discrete unit cell of a periodic square array as shown in Figure 3.3 and assume that the diffusing mass is macroscopically flowing in the horizontal direction and therefore there is no flux across the top and bottom edges. Although the fiber is considered to be impermeable in this work, this formulation is developed assuming that both the matrix and fiber are permeable and have saturation concentrations of D_m, C_m^∞ and D_f, C_f^∞ respectively. The matrix is assumed to be isotropic and the fibers are assumed to be transversely isotropic. Since the constituents are isotropic in the transverse plane and the fibers are arranged in a square array, the resulting microstructure will have the same effective diffusivity in the x and y directions, denoted by D_{eff}. Therefore, in order to obtain the effective

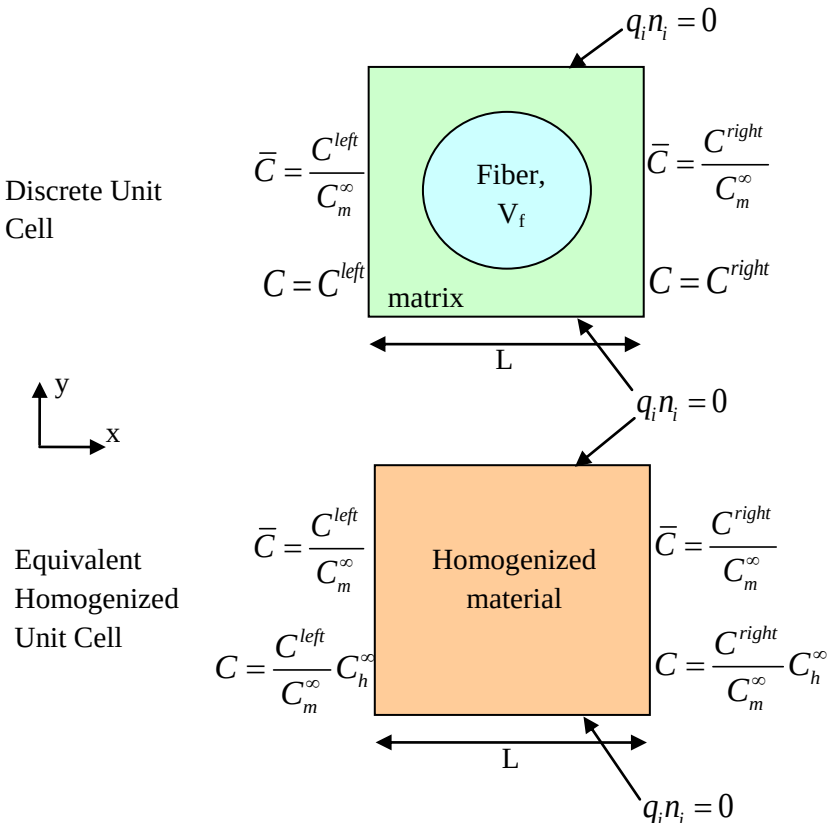

Figure 3.3: Boundary conditions for the discrete unit cell and the equivalent homogeneous unit cell

diffusivity for the microstructure, only one type of configuration needs to be analyzed with an imposed concentration gradient in the x direction. Suppose the concentrations on the left and right are C^{left} and C^{right}, respectively. The respective normalized concentrations are obtained by dividing the concentrations by C_m^∞. The finite element

model of the configuration can be analyzed by imposing the corresponding normalized concentrations on the left and right edges. The results will show a continuous variation of the normalized concentration across the domain as expected but the actual concentrations will have a discontinuity at the interface between the fiber and the matrix, if they have different saturation concentrations. It is convenient to define an effective property, d for the unit cell in terms of volume averaged values of the flux in the x direction, q_x and the normalized concentration gradient, $\frac{\partial \bar{C}}{\partial x}$.

$$\langle q_x \rangle = -d \left\langle \frac{\partial \bar{C}}{\partial x} \right\rangle \tag{3.45}$$

where the angle brackets indicate the volume average of the bracketed term.

The solution can be post-processed to give the volume averaged flux over the unit cell. For this simple geometry and boundary conditions, the volume-averaged normalized concentration gradient is simply $\left(\bar{C}^{right} - \bar{C}^{left}\right)/L$, although for more complicated models, the value can be obtained by post-processing the solution.

An equivalent homogenized material will have a saturation concentration value which is the volume-averaged value of the constituent saturation concentrations.

$$C_h^\infty = V_m C_m^\infty + V_f C_f^\infty \tag{3.46}$$

In the corresponding homogenized unit cell, the normalized concentrations at the right and left will be the same as that in the discrete unit cell as indicated in Figure 2.3. The actual concentrations at the right and left edge in the homogenized unit cell are obtained by using Eq.(3.9). Therefore the corresponding concentration on the left and right will be $C_h^\infty \frac{C^{left}}{C_m^\infty}$ and $C_h^\infty \frac{C^{right}}{C_m^\infty}$ respectively as shown in Figure 3.3. The equivalent concentration gradient can be written as

$$\left\langle \frac{\partial C}{\partial x} \right\rangle = \frac{\left(C_h^\infty \frac{C^{right}}{C_m^\infty} - C_h^\infty \frac{C^{left}}{C_m^\infty} \right)}{L} = C_h^\infty \frac{\left(\frac{C^{right}}{C_m^\infty} - \frac{C^{left}}{C_m^\infty} \right)}{L} \tag{3.47}$$

This can be rewritten in terms of the volume averaged normalized concentration gradients, $\left\langle \frac{\partial \bar{C}}{\partial x} \right\rangle$

$$\left\langle \frac{\partial C}{\partial x} \right\rangle = C_h^\infty \left\langle \frac{\partial \bar{C}}{\partial x} \right\rangle \tag{3.48}$$

Combining Eq.(3.45) and Eq.(3.48) gives,

$$\langle q_x \rangle = -\frac{d}{C_h^\infty}\left\langle \frac{\partial C}{\partial x} \right\rangle \tag{3.49}$$

which gives the expression for effective diffusivity as

$$D_{eff} = \frac{d}{C_h^\infty} \tag{3.50}$$

When the fiber is assumed to be impermeable, i.e. $D_f = 0, C_f^\infty = 0$, the expression for the effective diffusivity simplifies to

$$D_{eff} = \frac{d}{V_m C_m^\infty} \tag{3.51}$$

Under such an assumption, it is observed[12] that the ratio $\frac{d}{D_m C_m^\infty}$ is constant for a fixed fiber fraction, regardless of the value of the matrix diffusivity. Let this ratio be defined by the following,

$$\bar{D} = \frac{d}{D_m C_m^\infty} \tag{3.52}$$

A master curve can be obtained showing the variation of $\bar{D}$ with fiber fraction. This master curve shown in Figure 3.4 is valid as long as the diffusion follows Fick's law. The same is true for hexagonal arrays of impermeable fibers and Ref.[12] gives a simple curve fit for both master curves. This makes it convenient to obtain the effective diffusivity of a composite with impermeable circular fibers for various fiber fractions using the following,

$$D_{eff} = \frac{\bar{D} D_m}{V_m} \tag{3.53}$$

where $\bar{D}$ is obtained using the curve in Figure 2.4, which also describes the formula for the curve fit.

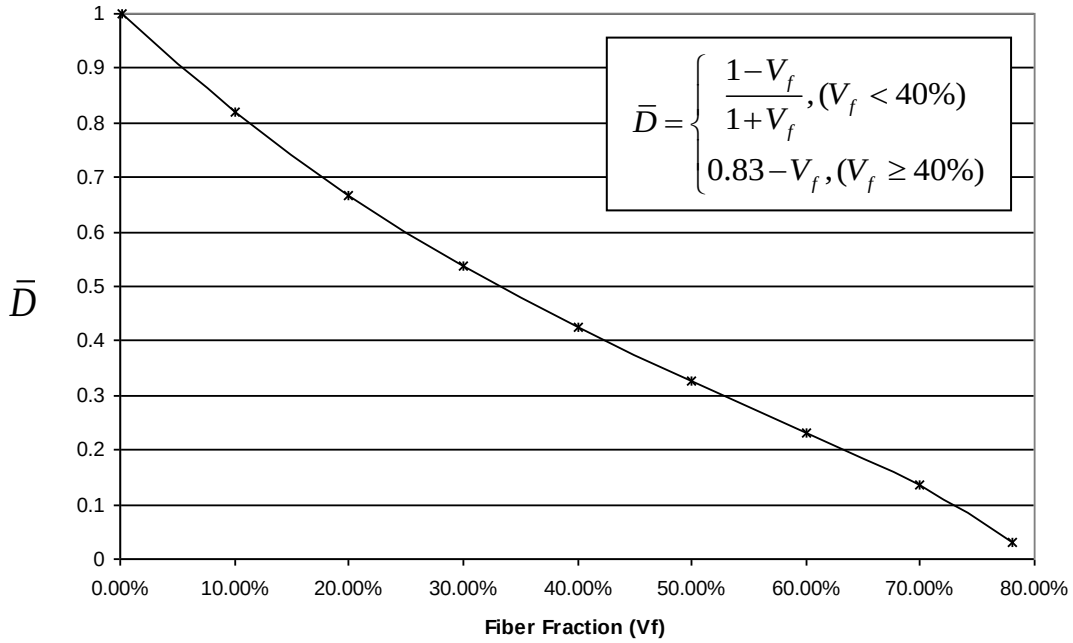

Figure 3.4: Master curve for impermeable circular fibers in square array showing variation of $\bar{D}$ with fiber fraction V_f (refer to eq(3.52) for definition of $\bar{D}$)

3.4. Oxidation

This section describes the governing equations and the finite element formulation for simulating the oxidation behavior in pure resin and in composites. The oxidation model can be considered an extension of the diffusion model as they are both based on the same conservation law. Some of the issues such as using normalized concentration as the primary variable are common to this analysis as well. The common aspects between the two analyses will be highlighted while describing the special circumstances that make this analysis different. This section will follow the same format as the section on diffusion and starts by listing the equations for the common analysis procedure. This is followed by the derivation of the weak form and its discretization to obtain the finite element formulation.

3.4.1. Conservation laws

The oxidation process in a polymer is a combination of the diffusion of oxygen and its consumption by reaction, which also results in the creation of by-products such as carbon dioxide. For the purposes of modeling the oxidation of polymers, the process is assumed to be dominated by the diffusion of oxygen into the polymer. The oxidation

model that is used in this research effort is primarily based on the work by Pochiraju et al[24-26] in which they used the conservation of mass law for diffusion with a term to model the rate of consumption of the diffusing oxygen during chemical reaction. The governing equation can be expressed as

$$\frac{\partial C}{\partial t} + \frac{\partial J_i}{\partial x_i} + R = 0 \tag{3.54}$$

where C is the concentration of oxygen, J_i is the diffusion flux and R is the reaction rate term.

This section is also used to completely define the reaction rate term and the related quantities. The reaction rate, R, in general, would depend on the concentration of oxygen, temperature and the availability of un-oxidized polymer. As the oxygen reacts with the polymer, the amount of polymer available for oxidation depletes and the oxygen will continue to diffuse to the interior of the polymer to react. Depending on the type of polymer, the process also leads to a reduction in the molecular weight of the material due to chemical bond breakage and the release of the oxidation by-products[26]. The amount of polymer available for oxidation is defined by an oxidation state variable called ϕ. The value of the oxidation state variable at which the polymer is considered to be completely oxidized with no more polymer available for reaction is defined as ϕ_{ox}. The oxidation state can be physically defined to be the ratio of the current weight of the material over its original un-oxidized weight. Therefore, the oxidation state ϕ has a range from ϕ_{ox} to 1 where an oxidation state value of 1 denotes the un-oxidized polymer. An oxidation state value between ϕ_{ox} and 1 indicates that the material is partly oxidized and can still undergo more oxidation. To illustrate this, three zones were defined by Pochiraju et al[24-26] as shown in Figure 2.5. Consider that the left end of the idealized material shown in the figure is exposed to oxygen and the oxidation propagates to the right. Zone III is the region of the material that is un-oxidized with an oxidation state of 1 and as the oxidation continues, this zone gets smaller while Zone I which denotes the fully oxidized material with an oxidation state of ϕ_{ox} increases. The zone in between where the oxidation state is between ϕ_{ox} and 1 is called the active zone and is denoted by Zone II. The expression for calculating the oxidation state variable is described later in this section.

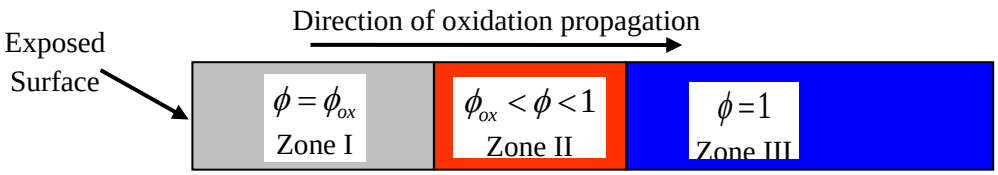

Figure 3.5: Oxidation zones and corresponding values of the oxidation state variable

When $\phi = \phi_{ox}$ at a material point, $R = 0$ and the process simplifies to just diffusion at that point. It is assumed that the effects of ϕ, T and C on R are separable such that the function R can be expressed as

$$R = \left(\frac{\phi - \phi_{ox}}{1 - \phi_{ox}} \right) f(C) R_0(T) \tag{3.55}$$

$R_0(T)$ is the "saturated reaction rate" (as described in Ref.[26]), which describes the dependence of the reaction rate on the temperature under saturation conditions. The polymer is considered saturated when it has the maximum amount of oxygen possible for the given temperature and pressure. The leading factor and $f(C)$ in the expression both have a range from 0 to 1. The leading factor models the dependence of the reaction rate on the availability of polymer that can be oxidized such that R is maximum when ϕ has a value of 1 and linearly decreases to zero when $\phi = \phi_{ox}$. The function $f(C)$ models the dependence of the reaction rate on the oxygen concentration. For modeling oxidation in polyimide resin systems like PMR-15 as implemented by Pochiraju, the function $f(C)$ is taken from the work by Colin et al[46-47].

$$f(C) = \frac{2\beta C}{1 + \beta C} \left[1 - \frac{\beta C}{2(1 + \beta C)} \right] \tag{3.56}$$

The value of β is determined by using weight loss data obtained from specimens aged at two different oxygen partial pressures i.e. at two different saturation conditions, typically in pure oxygen and air. The details of this procedure are given in Ref.[26]. The following ratio is obtained from the experimental work by Abdeljaoued[40],

$$\frac{\text{weight loss}_{\text{air}}}{\text{weight loss}_{\text{pure oxygen}}} = 0.7 \tag{3.57}$$

Assuming that the weight loss is proportional to the reaction rates, the ratio of the weight loss from the two specimens would be the same as the ratio of the reaction rates and would give the following equation,

$$\frac{R(C=0.79\,mol/m^3, 288°C)}{R(C=3.74\,mol/m^3, 288°C)} = \frac{R_0(288°C)\,f(C=0.79\,mol/m^3)}{R_0(288°C)\,f(C=3.74\,mol/m^3)} = 0.7 \qquad (3.58)$$

This can be solved to obtain three roots for β of which only one is non-zero and has a value of 0.919.

For modeling neat PMR-15 resin, ϕ_{ox} has a value of 0.187, which is taken from Pochiraju's work [24-26]. This value is determined from experimental weight loss data and the method is described in Ref. [26]. The oxidation state variable can be related to the weight loss of the material as follows

$$\frac{d\phi}{dt} \propto \frac{dW}{dt} \qquad (3.59)$$

where W is the weight of the material.

Assuming that the rate of change of weight is proportional to the reaction rate gives,

$$\frac{dW}{dt} \propto -R \qquad (3.60)$$

Combining Eq.(3.59) and Eq.(3.60) gives the following,

$$\frac{d\phi}{dt} = -\alpha R \qquad (3.61)$$

where α is a proportionality parameter that is, in general, time and temperature dependent.

Using Eq.(3.61), the following expression for calculating ϕ can be obtained

$$\phi = \max\left\{\phi_{ox}, \left(1 - \int_0^t \alpha(\varsigma) R(\varsigma)\, d\varsigma\right)\right\} \qquad (3.62)$$

An issue that arises when analyzing oxidation in heterogeneous materials is that although the oxidation state value for any material has an upper limit of 1, its lower limit for different materials is not necessarily the same. This makes it inconvenient to make comparisons as to how much oxidation has taken place. For example, the same oxidation state value for two different materials need not imply that they are equally close to being fully oxidized or that they have the same amount of material left to oxidize. In order to

make this comparison easier, a new variable is introduced called the oxidation level denoted by Φ. The oxidation level variable linearly scales the oxidation state variable so that all materials have an oxidation level that ranges from 0 to 1. This relation is given by,

$$\Phi = \frac{\phi - \phi_{ox}}{1 - \phi_{ox}} \tag{3.63}$$

For the same reasons described in Section 3.3.1, the differential equation described in Eq.(3.54) is re-written in terms of normalized concentrations,

$$C^{\infty} \frac{\partial \bar{C}}{\partial t} + \frac{\partial}{\partial x_i} J_i + R = 0 \tag{3.64}$$

3.4.2. Concentration gradients

Just as in the diffusion analysis, the oxidation analysis uses simple gradients of the concentration, $\frac{\partial C}{\partial x_i}$

3.4.3. Constitutive relations

The relationship between flux and the concentration gradient is given by Fick's first law,

$$J_i = -D_{ij} \frac{\partial C}{\partial x_j} \tag{3.65}$$

where D_{ij} is the 2nd order diffusivity tensor. The Latin subscripts *i* and *j* denote the coordinate direction and range from 1 to 3 for a three dimensional formulation. The constitutive relationship is different from that in the diffusion analysis described in Section 3.3.3 and that is because the diffusivities of the un-oxidized and oxidized polymer, in general, will be different. The diffusivity of the polymer in the active oxidizing zone (where $\phi_{ox} < \phi < 1$) is assumed to vary linearly between the un-oxidized polymer diffusivity and the fully oxidized polymer diffusivity and is given the following expression

$$D_{ij} = \left\langle D_{ij} \right\rangle_{un} \left(\frac{\phi - \phi_{ox}}{1 - \phi_{ox}} \right) + \left\langle D_{ij} \right\rangle_{ox} \left(\frac{1 - \phi}{1 - \phi_{ox}} \right) \tag{3.66}$$

Again, Eq.(3.65) is re-written in terms of the normalized concentration

$$J_i = -C^{\infty} D_{ij} \frac{\partial \bar{C}}{\partial x_j} \tag{3.67}$$

3.4.4. Boundary conditions

The boundary conditions are defined in the same manner as the diffusion analysis. The flux boundary conditions are given by

$$\hat{q} = -n_i J_i \quad \text{on S} \tag{3.68}$$

And the normalized concentration boundary conditions are given by

$$\bar{C} = \bar{C} \text{ on } \hat{S} \tag{3.69}$$

where $\bar{C}$ is the specified normalized concentration on the boundary $\hat{S}$.

3.4.5. Weak form

The same procedure is applied as described in Section 3.3.5 for the derivation of weak form for diffusion analysis. The difference is in the inclusion of the reaction rate term in the case of the oxidation analysis. The equation of conservation mass is multiplied by a variation of the normalized concentration and integrated over the volume to obtain the weighted integral form,

$$\int_V \delta\bar{C} \left[C^{\infty} \frac{\partial \bar{C}}{\partial t} + \frac{\partial}{\partial x_i} J_i + R \right] dV = 0 \tag{3.70}$$

where $\delta\bar{C}$ is an arbitrary variation of the normalized concentration.

Integration by parts gives the weak from,

$$\int_V \left[\delta\bar{C} C^{\infty} \frac{\partial \bar{C}}{\partial t} - \frac{\partial \delta\bar{C}}{\partial x_i} J_i + R\delta\bar{C} \right] dV + \int_S \delta\bar{C} n_i J_i dS = 0 \tag{3.71}$$

Using Eq.(3.67) and Eq.(3.68) in Eq.(3.71) gives the basis for the finite element formulation,

$$\int_V \left[\delta\bar{C} C^{\infty} \frac{\partial \bar{C}}{\partial t} + \frac{\partial \delta\bar{C}}{\partial x_i} C^{\infty} D_{ij} \frac{\partial \bar{C}}{\partial x_j} + R\delta\bar{C} \right] dV = \int_S \delta\bar{C} \hat{q} dS \tag{3.72}$$

3.4.6. Discretization of weak form and time integration

Again, the same basic procedure is applied as described in Section 3.3.6 for the derivation of finite element formulation. On the other hand, there are some details that are quite different from the diffusion analysis. This is because of the reaction rate term and the non-linear expression of the diffusivity in the weak form.

Over a typical finite element, the normalized concentration is approximated by

$$\bar{C}(x,t) = N_\alpha(x)\bar{C}_\alpha(t) \tag{3.73}$$

where N_α are the interpolation functions and $\bar{C}_\alpha$ are the nodal normalized concentrations. The subscripts with Greek letters range from 1 to the number of interpolation functions.

After discretizing the weak form using Eq.(3.73) and $\delta\bar{C} = N_\alpha \delta\bar{C}_\alpha$, the following set of equations are obtained,

$$\int_V \left[N_\alpha C^\infty N_\beta \frac{\partial \bar{C}_\beta}{\partial t} + \frac{\partial N_\alpha}{\partial x_i} C^\infty D_{ij} \frac{\partial N_\beta}{\partial x_j} \bar{C}_\beta + N_\alpha R \right] dV = \int_S N_\alpha \hat{q} dS \tag{3.74}$$

In matrix form this can be written as

$$M_{\alpha\beta}\dot{q}_\beta + K_{\alpha\beta} q_\beta + R^*_\alpha = F_\alpha \tag{3.75}$$

where

$$M_{\alpha\beta} = \int_V \left[N_\alpha C^\infty N_\beta \right] dV \tag{3.76}$$

$$K_{\alpha\beta} = \int_V \left[\frac{\partial N_\alpha}{\partial x_i} C^\infty D_{ij} \frac{\partial N_\beta}{\partial x_j} \right] dV \tag{3.77}$$

$$R^*_\alpha = \int_V \left[N_\alpha R \right] dV \tag{3.78}$$

$$F_\alpha = \int_S N_\alpha \hat{q} dS \tag{3.79}$$

$$q_\alpha = \bar{C}_\alpha \text{ and } \dot{q}_\alpha = \frac{d\bar{C}_\alpha}{dt} \tag{3.80}$$

Just as in the case of the diffusion analysis, an approximation is used for the time derivative term in Eq.(3.74) whereby the solution at a particular instant in time is determined based on the solution history. The same 'time-marching' procedure from Section 3.3.6 is used to numerically solve Eq.(3.74). Using Eq.(3.75), the following equations can be written for two consecutive time steps, $t=t_s$ and $t=t_{s+1}$,

$$M\dot{q}_s + K_s q_s + R_s^* - F_s = 0 \tag{3.81}$$

$$M\dot{q}_{s+1} + K_{s+1} q_{s+1} + R_{s+1}^* - F_{s+1} = 0 \tag{3.82}$$

Using the alpha family of approximations[45] gives

$$(1-\alpha)\dot{q}_s + \alpha\dot{q}_{s+1} = \Delta q / \Delta t \tag{3.83}$$

Multiplying Eq.(3.83) by $\Delta t M$ gives

$$(1-\alpha)\Delta t M\dot{q}_s + \alpha\Delta t M\dot{q}_{s+1} = M\Delta q \tag{3.84}$$

Rearranging the terms in Eq.(3.84) gives an expression for $\alpha\Delta t M\dot{q}_{s+1}$

$$\alpha\Delta t M\dot{q}_{s+1} = M\Delta q - (1-\alpha)\Delta t M\dot{q}_s \tag{3.85}$$

Multiplying Eq.(3.82) throughout by $\alpha\Delta t$ gives

$$\alpha\Delta t M\dot{q}_{s+1} + \alpha\Delta t\left[K_{s+1} q_{s+1} + R_{s+1}^* - F_{s+1}\right] = 0 \tag{3.86}$$

Substituting Eq.(3.85) into Eq.(3.86) gives,

$$M\Delta q - (1-\alpha)\Delta t M\dot{q}_s + \alpha\Delta t\left[K_{s+1} q_{s+1} + R_{s+1}^* - F_{s+1}\right] = 0 \tag{3.87}$$

And substituting for $M\dot{q}_s$ from Eq.(3.81) in Eq.(3.87) gives the governing equations

$$M\Delta q - (1-\alpha)\Delta t\left[-K_s q_s - R_s^* + F_s\right] + \alpha\Delta t\left[K_{s+1} q_{s+1} + R_{s+1}^* - F_{s+1}\right] = 0 \tag{3.88}$$

Using Eq.(3.33) and Eq.(3.34) in Eq.(3.88) gives

$$M\Delta q - a2\left[-K_s q_s - R_s^* + F_s\right] + a1\left[K_{s+1} q_{s+1} + R_{s+1}^* - F_{s+1}\right] = 0 \tag{3.89}$$

A Taylor Series expansion is used on the terms in Eq.(3.89) that are dependent on the unknown solution, (q_{s+1}), which are $K_{s+1}q_{s+1}$ and R^*_{s+1}. Indices will be used in the next few steps in order to make the operations involved clear. Ignoring the higher order terms in the Taylor Series expansion gives the following expression,

$$\left(K_{\alpha\beta}\right)_{s+1}\left(q_\beta\right)_{s+1}+\left(R^*_\alpha\right)_{s+1}\approx\left(K_{\alpha\beta}\right)_s\left(q_\beta\right)_s+\left(R^*_\alpha\right)_s+\frac{\partial\left[\left(K_{\alpha\beta}\right)_s\left(q_\beta\right)_s\right]}{\partial q_\zeta}\Delta q_\zeta+\frac{\partial\left(R^*_\alpha\right)_s}{\partial q_\beta}\Delta q_\beta \tag{3.90}$$

The partial derivatives in the expression above are very complex and therefore the aim is to obtain an approximation for the expression. It is assumed that for sufficiently small time steps, the error is minimal and certain approximations can be made. Similar approximations have been made in Pochiraju's oxidation model [24-26]. One approach to obtain an approximate expression for $\frac{\partial\left(R^*_\alpha\right)_s}{\partial q_\beta}$ is by assuming that only $f(C)$ from Eq.(3.55) depends on C. This would make it simpler to take a derivative of R^*_α with respect to the nodal variables, q_β. This approach will be evaluated in future work but for this work, it is assumed that if the time step is sufficiently small that $\left(R^*_\alpha\right)_{s+1}$ in Eq.(3.90) can be approximated by $\left(R^*_\alpha\right)_s$ (or mathematically, $\frac{\partial\left(R^*_\alpha\right)_s}{\partial q_\beta}=0$). The remaining partial derivative in Eq.(3.90) can be expressed as

$$\frac{\partial\left[\left(K_{\alpha\beta}\right)_s\left(q_\beta\right)_s\right]}{\partial q_\zeta}=\left(K_{\alpha\beta}\right)_s\frac{\partial\left(q_\beta\right)_s}{\partial q_\zeta}+\left(q_\beta\right)_s\frac{\partial\left(K_{\alpha\beta}\right)_s}{\partial q_\zeta} \tag{3.91}$$

The term $\frac{\partial\left(K_{\alpha\beta}\right)_s}{\partial q_\zeta}$ is not convenient to compute because $K_{\alpha\beta}$ depends on ϕ, which is a complex function of the solution (see Eq.(3.62)). Again, it is assumed that for sufficiently small time steps, Eq.(39) can be approximated by assuming $\frac{\partial\left(K_{\alpha\beta}\right)_s}{\partial q_\zeta}=0$. Thus Eq.(3.91) becomes

$$\frac{\partial\left[\left(K_{\alpha\beta}\right)_s\left(q_\zeta\right)_s\right]}{\partial q_\zeta}=\left(K_{\alpha\zeta}\right)_s \tag{3.92}$$

Therefore Eq.(3.90) becomes

$$\left(K_{\alpha\beta}\right)_{s+1}\left(q_{\beta}\right)_{s+1}+\left(R_{\alpha}^{*}\right)_{s+1}\approx\left(K_{\alpha\beta}\right)_{s}\left(q_{\beta}\right)_{s}+\left(R_{\alpha}^{*}\right)_{s}+\left(K_{\alpha\beta}\right)_{s}\Delta q_{\beta} \qquad (3.93)$$

Substituting Eq.(3.93) in Eq.(3.89) gives

$$M\Delta q-a2\left[-K_{s}q_{s}-R_{s}^{*}+F_{s}\right]+a1\left[\left(K_{s}q_{s}+R_{s}^{*}\right)+K_{s}\Delta q-F_{s+1}\right]\approx 0 \qquad (3.94)$$

Rearranging to bring all the terms involving the unknowns to the left side gives

$$\left[M+a1K_{s}\right]\Delta q\approx-(a1+a2)\left[K_{s}q_{s}+R_{s}^{*}\right]+a2\left[F_{s}\right]+a1\left[F_{s+1}\right] \qquad (3.95)$$

Eq.(3.95) is solved to obtain the solution for the *s+1* time step. For sufficiently small time steps, it is seen that this approximation is reasonable because a parametric study with different time step sizes showed the model appearing to converge to the same solution. Therefore, the finite element formulation for this oxidation model can be described by the following equations

$$\bar{M}\Delta q=\bar{F} \qquad (3.96)$$

where

$$\bar{M}=\left[M+a1K_{s}\right] \qquad (3.97)$$

$$\bar{F}=-(a1+a2)\left[K_{s}q_{s}+R_{s}^{*}\right]+a2\left[F_{s}\right]+a1\left[F_{s+1}\right] \qquad (3.98)$$

To arrive at this formulation, a number of approximations were made to simplify the nonlinearity. Typically, when solving a nonlinear equation numerically, a 'residual' is driven to zero by iterating. In this implementation, there is no iterating at each time step in order to drive a 'residual' to zero. This is because it was found that the even without iterating, the results were found to be reasonably close to that from Pochiraju's model.

An important part of the oxidation analysis is post-processing the results of the simulation to provide a measure of the oxidation behavior. The oxidation behavior is visualized in terms of the growth of the oxidation layer. The oxidation layer initiates from the surfaces exposed to the oxygen and grows into the interior as the material becomes oxidized. Although ideally the material is said to have started oxidizing when the oxidation level drops below 1, the oxidation layer thickness is defined by the point at which the oxidation level, Φ, dips below 0.99, indicating that 1% of the oxidizable material has oxidized. Therefore, an element is assumed to have started oxidizing if the oxidation level at each of the material integration points falls below 0.99. If the oxidation state is above 0.99, the element is assumed to be un-oxidized and if it is below 0.01 it is assumed to be fully oxidized. A post-processing routine was written that calculated the growth of the oxidation layer in the 1D model. This involved

extrapolating the oxidation state values from the integration points to the nodal points, averaging the extrapolated values at a node if the node shared elements of the same material and solving for the location in the model where the oxidation level value met the specified upper and lower limits. This routine was also generalized to work for 2-D and 3-D models. Note that the prescribed upper and lower limits of 0.99 and 0.01 respectively are valid only for a completely oxidizable material such as neat resin. When dealing with homogenized material such as a tow, the entire material does not oxidize because the fibers are assumed to be inert and therefore the prescribed limits will be different. In such a case, the upper limit that defines the oxidation layer thickness is the oxidation level when 1% of the resin in a homogenized tow material point is oxidized. This upper limit is given by

$$\Phi_{upper} = 1 - 0.01 V_m \tag{3.99}$$

The model described in this section was implemented and the oxidation layer growth was simulated for neat PMR-15 resin using a 1D model. The results were compared with that from Pochiraju's simulation. For a 200-hr simulation, it was found that both models agree closely in predicting the Zone I thickness. The difference is negligible in the beginning of the simulation and grows to a maximum difference at 200 hours when the current model predicts a thickness 107 microns compared to 104 microns predicted by Pochiraju's model. Both models predict the Zone II thickness to be almost constant throughout the 200 hr simulation. Pochiraju's model gives a Zone II thickness of 19 microns while the current model under predicts by 21% with a value of 15 microns. The cause of this difference could be the implementation of the two models. Pochiraju's 1D model[26] uses a modified implementation of *ode15s* and *Pdepe* solvers in MATLAB to solve the governing equation, Eq.(3.54). The current model on the other hand uses a standard one-dimensional finite element implementation based on Eq.(3.96). For the purposes of investigating the effect of oxidation on the mechanical response of the composites using this material system, it is assumed that the thickness of Zone I alone or the overall thickness (Zone I + II) that is of primary concern. Thus, if the overall thickness is considered, the difference between the two models is around 21% in the beginning and drops to about 2% at 200 hours, which is assumed to be negligible for the purposes of this particular research effort.

The various material input properties required for specifying the equations in the oxidation model are:

1. The diffusivities for the oxidized and un-oxidized material, D_{ox}, D_{unox}
2. Saturated reaction rate, R_0
3. Dependence of reaction rate on concentration, $f(C)$ and the constant β
4. Value of oxidation state when fully oxidized, ϕ_{ox}
5. Weight-reaction proportionality parameter, α

3.4.7. Boundary conditions for oxidation of periodic microstructures and homogenization

The oxidation response in polymers and PMCs is a nonlinear transient behavior. Just as in the case of diffusion, in order to simulate oxidation for periodic microstructures, the transient part of the behavior needs to be removed effectively looking at the microstructure at steady-state conditions. Under oxidation behavior, steady-state conditions imply that all the material in the microstructure is oxidized. But when all the material is oxidized, the behavior reverts to typical steady-state diffusion behavior. Therefore, it is not practical to obtain the effective oxidation material properties in this manner. Instead, other strategies are explored for simulating oxidation in periodic microstructures.

In order to model oxidation in a textile composite, it is necessary to obtain effective properties for the tows because it is impractical or even impossible to discretely model the entire microstructure. This section will describe approaches for obtaining effective oxidation material properties for tows.

When trying to replace a heterogeneous material with a homogenized material in model, it is reasonable to assume that some or possibly all of these properties might change. It can also be expected that there could be more than one way that these properties can change to demonstrate the same overall behavior as a discretely modeled heterogeneous microstructure. There are at least two approaches for achieving this goal. One is to use a multi-scale analysis that keeps track of the 'local' information such as oxidation state and actual average concentration in the constituent matrix in the homogenized material. Given this information, it would be possible to calculate the reaction rate R at a particular material point in the tow's constituent matrix using Eq.(3.55). Next, the effective reaction rate for the larger scale homogenized tow is determined by a simple rule of mixtures and plugged into the governing equations. When the equations for a time step are solved, the calculated concentrations are transformed back to the local scale using a rule of mixtures in order to keep track of the oxidation state of the constituent matrix. Thus, a continuous transfer of information between the two scales needs to be maintained throughout the simulation. For this work, another approach is used where effective oxidation properties for the homogenized material are determined thereby eliminating the need to go back and forth between the two scales. A few assumptions are made in order to determine the effective material properties, D_{ox}, D_{unox}, R_0, $f(C)$, β, ϕ_{ox} and α. These assumptions and the procedure to determine the properties are described in the remainder of this section.

In this work, the fibers in the tows are idealized to be in a square array and the fibers are assumed to be impermeable and do not oxidize. While there are other factors that can influence the oxidation behavior in composites such as the properties of the fiber/matrix interface or interphase, they are not taken into account for the homogenization model described in this work. Cracks in the matrix or along the fiber/matrix interface can also

affect the oxidation behavior by allowing rapid ingress. Depending on the type of damage that is observed in these composites, it might be possible to account for their effects in the homogenized model. For example, if the damage is diffuse, the homogenized properties can be degraded appropriately or if the damage is confined to certain areas, cracks can be introduced in the homogenized model. Since this model does not consider factors such as the effect of damage, fiber/matrix interface or cracks in the composites, the only oxidation material property that is different when considering axial and transverse growth is the diffusivity. The axial diffusivity is largely governed by a rule of mixtures and exhibits simple behavior. Therefore, particular attention is not paid to the axial oxidation behavior. Moreover, in realistic applications, the surfaces exposed to oxidizing environments are mostly parallel to the fibers. The laminate configurations that are analyzed in this work are chosen based on these considerations and therefore, the oxidation behavior depends on the transverse oxidation material properties.

3.4.8. Oxidation parameters

This sub section will describe some of the effective material properties mentioned in the previous sub section related to boundary conditions for oxidation of periodic microstructures.

3.4.8.1. Diffusivities for the oxidized and un-oxidized material D_{ox}, D_{unox}

The diffusivities on its own only define the mass flow of oxygen in the material. It will be assumed that the oxidation state continues to have a linear effect on the effective diffusivities of the homogenized material. The effective diffusivity can be determined by just modeling the diffusion without the need for modeling the oxidation behavior. The procedure for determining effective diffusivity as described in Section 3.3.7 is used to obtain the effective diffusivities for the oxidized and un-oxidized material.

3.4.8.2. Saturated reaction rate, R_o

Since the matrix is the only material that is oxidizing, the effective saturated reaction rate would be expected to be related to the amount of matrix in the unit cell. It is assumed that the relationship follows a rule of mixtures (with the fiber having a reaction rate of zero). That is

$$R_0 = V_m R_0^{matrix} \tag{3.100}$$

3.4.8.3. Dependence of concentration on reaction rate on $f(C)$ *and* β

The term $f(C)$ models the dependence of the reaction rate on the oxygen concentration. Colin's expression[46-47] given in equation (3.56), which is used as $f(C)$ to model the neat PMR-15 polymer will be used for the homogenized tow as well. It is assumed that

the same expression models the behavior of the homogenized tow. As mentioned in the previous section, to determine the value of β the ratio of the weight loss of the material at two different saturation conditions is needed. Due to lack of access to experimental data on oxidation weight loss for unidirectional laminates, it is assumed that the ratio of weight loss is the same as that of the neat PMR-15 polymer. Therefore, β has the same value as that of the neat resin, which is 0.919.

3.4.8.4. Oxidation state when fully oxidized, ϕ_{ox}

This is a property that is calculated by determining the weight loss of the material when oxidized. For example, a value of 0.2 implies that the fully oxidized material weighs about 20% of its original weight. Due to lack of access to weight loss data for unidirectional laminates, an estimate for ϕ_{ox} is obtained based on the assumption that the fiber does not lose weight during oxidation. Therefore, the effective ϕ_{ox} would be given by

$$\phi_{ox}^{eff} = 1-(1-\phi_{ox}^{m})V_m \tag{3.101}$$

3.4.8.5. Weight-reaction proportionality parameter, α

In general, the proportionality parameter α is time and temperature dependent. The value of α for the neat resin is determined by examining the oxidation layer growth. On comparison of the simulation results with the experimental results, Pochiraju [9] found that the oxidation behavior was better simulated when the proportionality parameter was linearly decreased over time from 0.01 to 0.0033 for the first 40 hours of oxidation and then remains constant at 0.0033. The value of α for the homogenized tow is assumed to follow the same as that of the neat PMR-15 resin.

3.5. Coupled mechanical-oxidation analysis

A coupled mechanical-oxidation analysis model was developed to predict damage initiation and progression in textile composites under an oxidizing environment. Although the analyses performed in this work assumes only one-way coupling, the underlying analysis model forces no such restriction and can account for full coupling between the mechanical and oxidation analysis. This section describes the coupled analysis model used in this work followed by the constitutive relations used to the couple the two analyses.

One component of the coupled analysis is the oxidation analysis that simulates the diffusion of oxygen into the composite and tracks how much the material has oxidized. The second component is the damage progression analysis that can track the damage in the material and degrade the properties of the damaged regions. The theory and finite element formulation behind both the oxidation analysis and the damage progression analysis is provided in the previous sections and they are adapted to use in this coupled

analysis model. The coupling between the two analyses is enabled by constitutive relations. The full coupling requires a constitutive relation relating the oxidation state to the mechanical properties and another constitutive relation relating the mechanical state to the oxidation material properties. In this work, all the configurations that were analyzed assumed only a one-way coupling with the oxidation state affecting the mechanical properties of the model. The remainder of this section describes the algorithm for this one-way coupled model. The implementation and the details involved with performing an actual coupled analysis on a textile composite configuration will be explained in a later section.

Since the analysis assumes only one-way coupling and the mechanical state does not affect the oxidation material properties, the oxidation analysis can be performed independent of the damage progression analysis. Therefore, the output from the oxidation simulation can be used by the model as needed. The oxidation analysis output contains the oxidation state distribution in the configuration at different times in the simulated oxidation time period. The damage progression analysis described is a quasi-static analysis where the loading is ramped up but is essentially time-independent. On the other hand, all the coupled models analyzed in this work assume a constant mechanical loading while the configuration is undergoing oxidation. Therefore, the damage progression analysis cycles through each of the time data-points in the simulated oxidation time period and performs the following steps – Load the oxidation state for the particular time data-point, modify the mechanical properties and iterate to converge upon the final damage state for the corresponding time data-point. This is illustrated in the flowchart for the algorithm shown in Figure 3.6.

3.6. Constitutive Relations

Experimental results show that oxidation causes damage in the oxidized material which can ultimately affect the mechanical properties of the composite [26]. Oxidation is found to affect the mechanical properties of fibers [26]. But it is not trivial to characterize the damage and its effects on the mechanical properties of the composites. The underlying mechanisms and the properties of the fiber/matrix interface and interphase have not been fully understood yet. Shrinkage of the matrix due to oxidation is theorized to be among the factors causing delaminations on the fiber matrix interface [30]. These cracks can further affect the oxidation behavior by allowing oxygen to penetrate the material faster. But the effects of the mechanical or physical damage on the oxidation behavior are not being considered in the simulations used in this work. This section will describe the type of constitutive relations used in the simulations that were performed in this work.

This constitutive relation or degradation scheme is similar in some respect to the property degradation scheme based on mechanical damage. They are similar in the sense that the engineering moduli are modified to account for the effect of the oxidation. The constitutive relation quantifies the amount of damage in terms of strength and stiffness degradation based on the oxidation level of the material in the composite (see Eq.(3.63)).

Let E_{ij}, G_{ij} and ν_{12} be the original extensional moduli, shear moduli and Poisson's ratio respectively and $\overline{E}_{ij}$, $\overline{G}_{ij}$ and $\overline{\upsilon}_{ij}$ be the degraded extensional moduli, shear moduli and Poisson's ratio respectively. b_i $(i=1..9)$ are the percentages by which the nine engineering properties change when the material is completely oxidized. Remember that the oxidation level, Φ ranges from 1, which means un-oxidized to 0, which means fully oxidized. The amount of degradation is assumed to vary linearly with the oxidation level. Therefore, a typical property degradation scheme will look like:

$$\begin{aligned}
&\overline{E_{11}} = (1+(1-\Phi)b_1)E_{11}, \quad \overline{E_{22}} = (1+(1-\Phi)b_2)E_{22}, \quad \overline{E_{33}} = (1+(1-\Phi)b_3)E_{33} \\
&\overline{G_{12}} = (1+(1-\Phi)b_4)G_{12}, \quad \overline{G_{23}} = (1+(1-\Phi)b_5)G_{23}, \quad \overline{G_{13}} = (1+(1-\Phi)b_6)G_{33} \\
&\overline{\upsilon_{12}} = (1+(1-\Phi)b_7)\upsilon_{12}, \quad \overline{\upsilon_{23}} = (1+(1-\Phi)b_8)\upsilon_{23}, \quad \overline{\upsilon_{13}} = (1+(1-\Phi)b_9)\upsilon_{33}
\end{aligned} \tag{3.102}$$

For example, if E_{11} is reduced by 20% when the material is fully oxidized, then $b_1 = -0.2$. If the E_{11} property needs to be degraded for a material that has an oxidation level of 0.3, the new modulus, according to Eq.(3.102) would be given by

$$\overline{E_{11}} = (1+(1-\Phi)b_1)E_{11} = (1-0.7\times 0.2)E_{11} = 0.86E_{11} \tag{3.103}$$

Note that in this general framework, the diagonal as well as non-diagonal entries of the compliance matrix can be affected independently.

Similarly, the strength can also be degraded based on the amount of oxidation the material has undergone. In this work, the strengths under compression are assumed to be the same as the strengths under tension. Let S_i, $(i=1..6)$ denote the original strengths of the material in the different stress components (in Voigt notation) and $\overline{S_i}$, $(i=1..6)$ be the degraded strengths. Let the strength degradation parameters, d_i, $(i=1..6)$ be the corresponding factors by which the strengths would be degraded if the material was fully oxidized. Again, a linear dependence on the oxidation level, Φ is assumed. Therefore, the strength degradation scheme will look like the following

$$\overline{S_i} = (1+(1-\Phi)d_i)S_i \tag{3.104}$$

The specific details of property degradation scheme used in this work including the degradation factors used for the different materials will be given in Section 9.

The two degradation schemes involved with the coupled analysis, that is, one based on the stress state/mechanical damage, and the other based on the oxidation, need to be aggregated to provide the overall mechanical properties of the material based on the oxidation level and the mechanical damage. At each time step, this overall set of properties will be used to perform the stress analysis in the damage progression model, and then check for new damage based on the failure criteria. In this work, a procedure

has been implemented to combine the two degradation schemes. This procedure in the coupled analysis algorithm would correspond to the box in Figure 3.6 that is labeled 'Modify mechanical properties based on current oxidation state and damage state'. Let us consider the procedure for a material point in the configuration. The procedure takes the initial mechanical properties for the material and the current oxidation and damage state as input and returns the modified mechanical properties. The procedure is as follows. The initial mechanical properties are modified following the degradation scheme based on the oxidation level. At the end of this first step, the compliance matrix has been modified according to Eq..(3.102), and the strengths have been modified according to Eq.(3.104) In the second step the new properties are then modified again based on the degradation scheme based on mechanical damage. Therefore, at the end of the second and final step, the properties obtained from the first step are then modified according to Eq.(3.6). In reality, the order of the steps do not matter and the overall elastic moduli can be summarized as follows

$$\begin{aligned}
&\overline{E_{11}} = \left[\frac{(1+(1-\Phi)b_1)}{a_1}\right]E_{11}, \quad \overline{E_{22}} = \left[\frac{(1+(1-\Phi)b_2)}{a_2}\right]E_{22}, \quad \overline{E_{33}} = \left[\frac{(1+(1-\Phi)b_3)}{a_3}\right]E_{33} \\
&\overline{G_{12}} = \left[\frac{(1+(1-\Phi)b_4)}{a_4}\right]G_{12}, \; \overline{G_{23}} = \left[\frac{(1+(1-\Phi)b_5)}{a_5}\right]G_{23}, \quad \overline{G_{13}} = \left[\frac{(1+(1-\Phi)b_6)}{a_6}\right]G_{33} \\
&\overline{\upsilon_{12}} = \left[\frac{(1+(1-\Phi)b_7)}{a_7}\right]\upsilon_{12}, \quad \overline{\upsilon_{23}} = \left[\frac{(1+(1-\Phi)b_8)}{a_8}\right]\upsilon_{23}, \quad \overline{\upsilon_{13}} = \left[\frac{(1+(1-\Phi)b_9)}{a_9}\right]\upsilon_{33}
\end{aligned} \tag{3.105}$$

The overall strengths would be simply those given by Eq..(3.104) because the degradation scheme based on mechanical damage does not modify the strengths of the material.

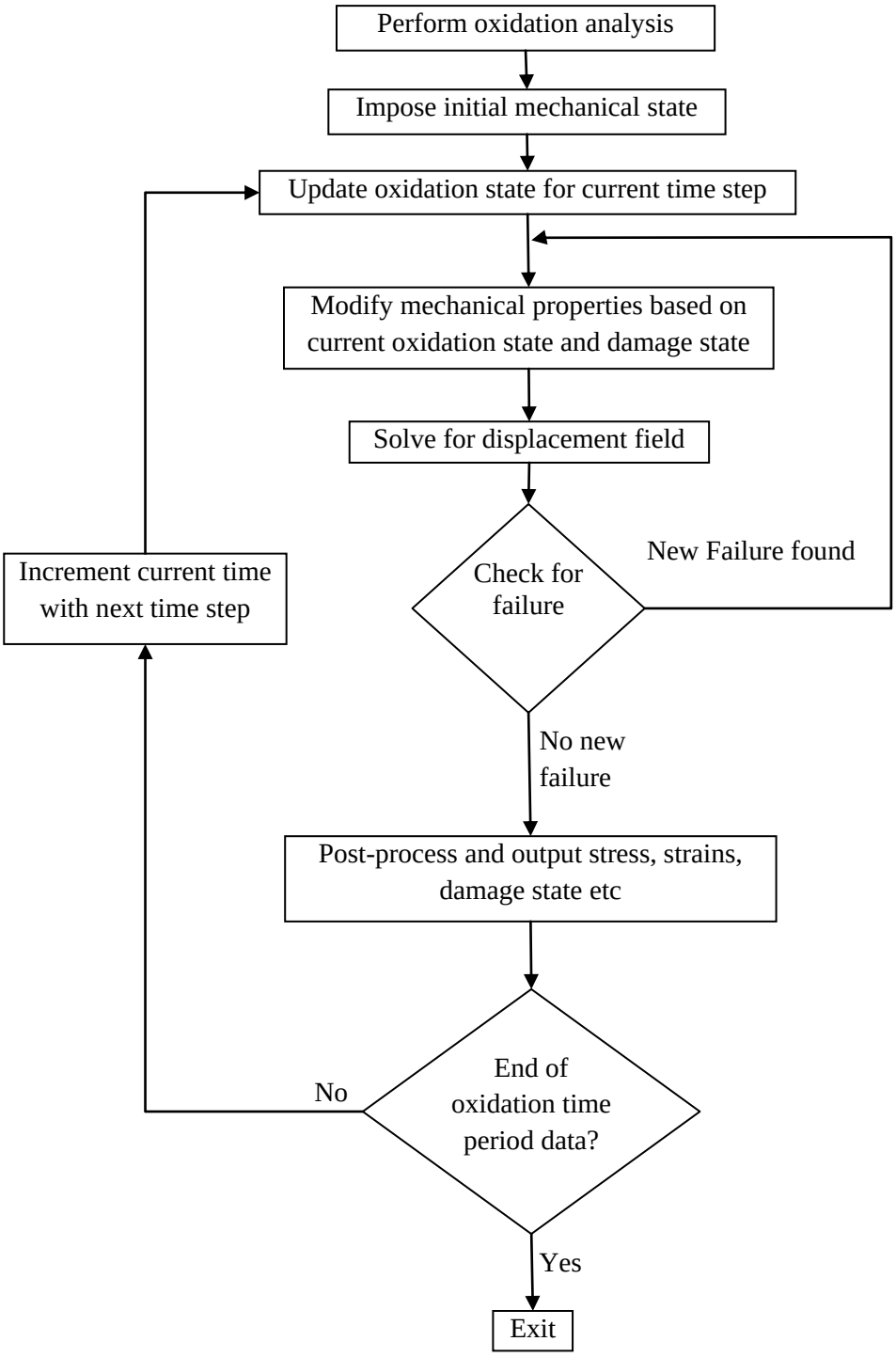

Figure 3.6: Algorithm for one-way coupled oxidation-damage progression analysis

3.7. Summary

The common aspects of some of diffusion and oxidation analyses were discussed in this section and a common analysis procedure was determined that can be used to help design an analysis framework. The procedure is then used to derive the theory and equations involved in the different analysis models used in this work. The finite element formulations for the models were derived and the algorithms for the analysis were discussed. It also discusses the strategies involved in analyzing periodic configurations and obtaining effective properties for periodic microstructures. The models described in this section are implemented in a finite element analysis framework as described in the next section.

4. Implementation

This section describes the implementation of the finite element formulation presented in Section 3. The overall challenges of implementing an oxidation analysis into a finite element code will be discussed. An overall analysis algorithm will be presented, followed by more detailed algorithms for various subroutines including assembly, calculation of the stiffness matrix and load vector, and post-processing to update oxidation state.

4.1. Challenges

The finite element modeling of oxidation is a transient procedure that requires the modeling the mechanisms of diffusion of oxygen through a material as well as oxidation which acts as a sink in which reaction consumes oxygen. Modeling diffusivity is relatively straightforward with the main challenges pertaining to oxidation. These challenges include:

- Modeling the oxidation process (reaction rate) at a point
- Modifying the diffusivity due to changes caused by oxidation
- Developing a metric (oxidation state) to characterize how much oxidation has occurred at a point

4.2. Overall analysis algorithm

This subsection gives the basic algorithm that drives the oxidation analysis. For simplicity this algorithm is for manual time stepping using predefined time step sizes. There is no check for the suitability of a particular time step to give an acceptable change in the solution. For efficiency concerns, it is likely that an adaptive time step procedure will need to be used.

For a particular time step, the time integration parameters a_1 and a_2 must be calculated using Eqs. (3.33) and (3.34)). Next the equations are set up by assembling the elemental $\bar{M}$ and $\bar{F}$ (calculated using Eqs. (3.97) and (3.98)) into the global system of equations to which boundary conditions are applied. The system of equations is solved, with the solution being the increment in the solution between the current time step and the previous time step. From this change in solution, the current solution is calculated. Using the current solution, the oxidation state is updated which will be used in post-processing as well as the calculation of diffusivities and reaction rates.

FOR s = 1 to # of time steps

- Calculate time integration parameters
- Set up equations

Assemble $\bar{M}$ *and* $\bar{F}$

Apply boundary conditions

- Solve $\bar{M}\Delta q = \bar{F}$
- $q_{s+1} = q_s + \Delta q$
- Update oxidation state
- Output (if desired)

END FOR

4.3. Assembly

This subsection gives the algorithm that assembles the equations for the finite element implementation of the oxidation analysis. For a particular element, the degree of freedom (DOF) list which relates the local DOF numbering of the element to the corresponding global DOF is calculated. The element K matrix is calculated using Eq. (3.77) . This calculation is dependent on diffusivity which is now updated to reflect the most recently available oxidation state at the time the K matrix is calculated. The element M matrix is calculated using Eq. (3.76) which is independent of material properties and remains constant (for each element) throughout the analysis. The element reaction vector R* is calculated using Eq. (3.78) and is dependent on temperature and oxygen concentration. The element K, M, and R* are utilized to form $\bar{M}$ and $\bar{F}$ as shown in Eqs. (3.97) and (3.98). The degree of freedom list is then used to assemble the element matrix and vector in the global system of equations.

FOR i = 1 to # of elements

- Calculate DOF List
- Calculate Element K
- Calculate Element M
- Calculate Element R*

- Form element $\bar{M}$ and $\bar{F}$
- Assemble $\bar{M}$ and $\bar{F}$

END FOR

4.4. Stiffness matrix calculation

This subsection details the calculation of the elemental K matrix (Eq. (3.77)). As typical with finite element formulations, shape function derivatives and volumes associated with the an integration point must be calculated. In particular, the diffusivity of a particular integration point must be calculated. This is done by scaling between unoxidized and oxidized diffusivities using the oxidation state at the integration point (see Eq. (4.1)). Using this and the aforementioned calculation, the particular integrations points contribution to the elemental K matrix may be calculated.

$$D_{ij} = \left(\frac{\phi - \phi_{ox}}{1 - \phi_{ox}} \right) D_{ij_{unoxidized}} + \left(\frac{1 - \phi}{1 - \phi_{ox}} \right) D_{ij_{oxidized}} \tag{4.1}$$

FOR j = 1 to # of integration points
- Calculate volume associated with integration point
- Calculate shape function derivatives
- Calculate integration point diffusivity
- Calculate integration point's contribution to element K

END FOR

4.5. Reaction vector calculation

This subsection describes the elemental calculation of the reaction vector R* (Eq. (3.78)). Again the volume associated with the integration point and the shape function values are calculated. The most recent nodal concentrations are then interpolated for the concentration at the integration point. This concentration is used to evaluate the function $f(C)$ using the material parameter β (Eq.(3.56)). This function is then used with the temperature dependent reaction rate R_o, and the oxidation state at the integration point to calculate a reaction rate (Eq. (3.55)) which reflects the most recent oxygen concentration, oxidation state, and temperature.

FOR j = 1 to # of integration points
- Calculate volume associated with integration point
- Calculate shape function values
- Interpolate element's nodal concentration values at integration point
- Evaluate *f(C)* function
- Calculate reaction rate with oxidation state, *f(C),* and R_o

END FOR

4.6. Updating oxidation state

This section describes the post-processing step of updating the oxidation state. After the solving step is completed, the oxidation state must be updated for every integration point in the model. This requires an integration point loop nested inside a element loop as shown in the algorithm below. For a particular integration point, an updated reaction rate will be calculated which incorporates the most current oxygen concentration and oxidation state (as well as temperature) for the integration point of interest. The proportionality parameter α is calculated for the particular time as described in Section 3.4.8. Next the oxidation state integral is updated to reflect the current time step (Eq. (4.2)) and the oxidation state is calculated using Eq.(3.62) .

$$\int_{t_s}^{t_{s+1}} \alpha(\zeta) R(\zeta) d\zeta \approx a(t_{s+1}) R(t_{s+1}) \Delta t \tag{4.2}$$

FOR i = 1 to # of elements
FOR j = 1 to # of integration points
- Evaluate integration point's reaction rate
- Calculate proportionality parameter at current time
- Evaluate current time step's contribution to oxidation state integral
- Calculate oxidation state (Eq. 3.62)
END FOR
END FOR

4.7. Summary

Section 3 provided a detailed finite element formulation for oxidation analysis. This section has provided the details for implementing such a formulation into a finite element code. The challenges of such an implementation were addressed. Implementation algorithms were provided that outlined the more challenging details of the implementation that were unique from a typical finite element implementation. With the implementation of an oxidation finite element formulation complete, the next section will focus on ways to expedite an oxidation finite element analysis.

5. Strategies to Expedite Analysis

Restriction on element and time step size can make diffusion and oxidation analysis time consuming. Oxidation analysis requires a longer analysis time due to the reaction of oxygen with the polymer which serves to slow the progression of oxygen. In order to expedite the analysis a variety of strategies were considered. These include optimization of element size and time step size, an adaptive meshing strategy, and a decoupled subdomain strategy for textiles. The use of approximate boundary conditions was also considered to reduce the size of the analysis region. An adaptive time stepping algorithm has also been developed. Finally, the efficiency of the implementation has been increased mainly through parallel algorithms and the exploitation of direct solver characteristics.

5.1. Optimization of element size and time step size

As with typical mechanical analyses, the accuracy of the solution depends on several factors, one of which is the element size. In the case of transient analyses like diffusion or oxidation, the solution also depends on the time step size. Depending on the material properties and other values in the finite element formulas, there are limits to the element size and time step size beyond which meaningless results are obtained. Analyses were performed using COMSOL Multiphysics to confirm that other finite element packages had the same limitations. In addition to the basic approximation for the time integrations, there are several approximations made in the finite element formulation to handle the nonlinearity in the governing equations. The accuracy of these approximations depends on parameters such as the time step size as well.

In general, the optimal time step size need not be constant throughout the simulation because of the nonlinear oxidation behavior. This means that the time step size can potentially be ramped up or down as the simulation is in progress so as to maintain the optimal time step size. To summarize, the following optimizations can be made to an oxidation simulation in order to make it run more efficiently:

1. Optimal element size
2. Optimal time step size
3. Optimal time step size ramping

Parametric studies were conducted to determine the optimized parameters for the materials that would be analyzed in this work. The latter part of this section will discuss the results of these parametric studies.

The remainder of this section describes the oxidation behavior in neat PMR-15 resin. Certain characteristics of the oxidation behavior can be exploited to develop a strategy to speed up the analysis. For this purpose, oxidation of a simple configuration is considered. The simple configuration is a block of neat resin that is exposed to oxygen on one pair of opposite surfaces that are 40 mm apart and protected from oxygen on the

other surfaces. This configuration can be analyzed using a 1-D model. Moreover, taking advantage of symmetry, only half of the block needs to be modeled. Table 5.1 gives the material properties used to model the neat PMR-15 resin. For a complete description of the different oxidation material properties, refer to Section 3.4.8. A uniform element size of 1micron and time step size of 0.15 minute was used for the simulation.

Figure 5.1 shows the predicted oxidation layer growth for the configuration over a period of 200 hours. Section 3.4.6 describes how the oxidation layer growth is determined. It can be seen that the resin oxidizes very quickly in the initial 20 hours or so and then gradually slows down to where the oxidation layer grows almost linearly. Also note that the thickness of zone II or the active zone remains fairly constant throughout the entire process.

Table 5.1: Oxidation material properties for neat PMR-15 resin

	Neat PMR-15 resin
Diffusivity D_{unox} D_{ox}	 53.6×10^{-6} mm^2/min 78.22×10^{-6} mm^2/min
R_0	3.5 mol/(m^{3}min)
ϕ_{ox}	0.187
C^{∞}	0.79 mol/m^3
α	0.01-0.0067(t/40) : t < 40 0.0033 : t > 40 (t in hours)
$f(C)$	$\frac{2\beta C}{1+\beta C}\left[1-\frac{\beta C}{2(1+\beta C)}\right]$
β	0.919

The difference between oxidation and diffusion-only is that for oxidation, the oxygen molecules do not diffuse as quickly because they are consumed in oxidizing the material. Thus, the reaction term in the governing equations gives the effect of a 'moving barrier' that allows almost no oxygen to cross over to the other side of the active zone until there is a sufficient level of oxidation within the active zone. This is evident by looking at the concentration profiles across the model at different snap shots during the simulation. Figure 5.2 shows the concentration profiles in the model at t=2.5 hrs, 50 hrs and 100 hrs. It can be seen that all the profiles have a similar shape. The profiles drop almost linearly from the exposed edge up to the 'moving barrier' and the concentration is practically zero for the rest of the model. The difference in each profile is that as time passes, the location of the 'moving barrier' shifts in the direction of the oxygen flow. This movement of the barrier is very slow compared to the diffusion-only process. This is

illustrated in Figure 5.2 by the concentration profile of the corresponding diffusion model at 15 minutes. It shows that with only 15 minutes of diffusion, the oxygen concentration at every point in the model has already surpassed that of the oxidation model at 2.5 hours. Even after 100 hours of oxidation, the oxygen concentration is still practically zero past 0.06 mm whereas the corresponding concentration from the diffusion model after 15 minutes is more than 0.025 at 0.06 mm. This also explains why there is a close to linear drop of the concentration from the exposed edge to the 'moving barrier'. In each snapshot of concentration profile in the oxidation process, the region to the left of the moving barrier can be considered as a diffusion only region with fixed concentration boundary conditions – the specified concentration at the exposed boundary and zero concentration at the location of the barrier. Since the barrier is moving very slowly, the concentration profiles at the various time steps look very similar to that for the corresponding diffusion-only problem at steady-state, which is a nearly linear variation of the concentration. Examination of this behavior gave way to a strategy to further expedite the oxidation simulation. This strategy was called the "Adaptive Meshing Strategy" and is described in detail in the next section.

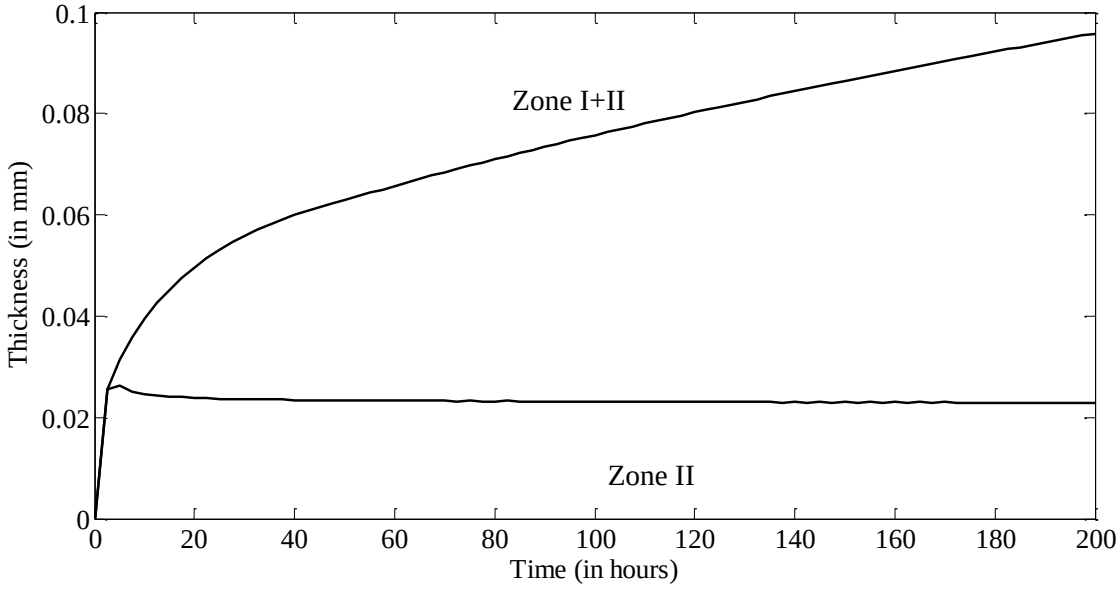

Figure 5.1: Predicted oxidation layer growth (Zone I+II, Zone II) in neat PMR-15 resin

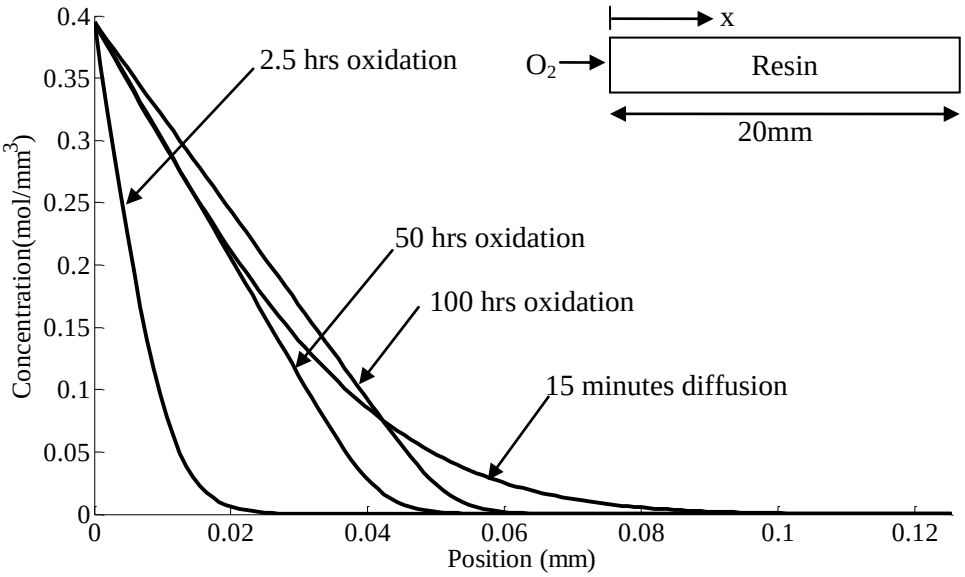

Figure 5.2: Concentration profiles for oxidation and diffusion models.

5.2. Adaptive meshing strategy

The fact that the concentration of oxygen in the un-oxidized region of the material is practically zero can be exploited to speed up the analysis by constraining the degrees of freedom(DOF) in most of the un-oxidized region to zero. This can lead to a considerable reduction in the number of unknowns to be solved for, especially in the initial period of oxidation because most of the material is un-oxidized at that time. The challenge is in determining which regions of the material should be constrained and developing an efficient algorithm so that this can be automated. The regions very close to the active zone should not be constrained since the active zone is slowly moving to the interior of the material with each time step and that can affect the solution. Also, the regions should not be permanently constrained because that implies that those regions will never get oxidized, which is not the case.

Based on these requirements, the following algorithm was developed to automatically determine the regions to be constrained. A very small concentration value close to zero is chosen, say C^0, in order to determine which regions are to be constrained. If the concentration at a node is more than C^0, then that location is assumed to be inside the oxidation layer or close to it and therefore the DOF for that node is left unconstrained. On the other hand, if the concentration at a node is less than C^0, then the node is assumed to be in the un-oxidized region and far enough from the active zone, therefore that DOF is constrained. This check is not performed at every time step. Instead, the

check is performed every 15 or 20 time steps or some optimal number of time steps (say, *N*) chosen depending on the rate the active zone is moving. Therefore, once a check is performed, the constrained DOFs remain constrained for the subsequent time steps until the time step right before the next check. In this time step preceding the check, all the artificial constraints are removed and the full system of equations is solved. This allows a minute amount of oxygen to enter the previously constrained region. In the next time step, the check is performed, at which time some of the previously constrained DOFs will be unconstrained because the oxygen concentration has increased by a small amount. This cycle is repeated throughout the simulation. This strategy speeds up the analysis by a large factor because in the standard analysis, every time step involves solution of the entire system of equations whereas in the adaptive mesh analysis, the entire system of equations is solved only every *N* time steps. During the other time steps, the system of equations solved is much smaller. The check to determine the region to be constrained is also performed only every *N* time steps and the computation effort used for the check is miniscule compared to the savings obtained by solving a smaller set of equations. In addition to those savings, whenever the check is performed and a region of the un-oxidized material is constrained, the corresponding elements are also deactivated thereby speeding up the finite element assembly process as well.

The choice of the value of C^0 has an effect on the analysis because if the value is too large, regions that are close to the active zone will be constrained whereas if the value is too small, a smaller region is constrained and the strategy is not used to its maximum potential. Similarly, the number of time steps that is skipped before a check, *N*, also has an effect on the efficiency of the simulation. Parametric studies were performed by varying the two parameters, C^0 and *N* on 1-, 2- and 3-D models. The results of this parametric study are presented in the validation section of this report.

5.3. Decoupled subdomain strategy

Textile composites have multiple microstructural scales – the fiber/matrix scale, the tow architecture scale and laminate scale. As mentioned in the previous sections, it is not practical to discretely model all the fibers in the composite because of modeling and computational challenges. Effective oxidation material properties that are derived in Section 3 and validated in Section 7 are used to model the tows in the textile composite. The adaptive meshing strategy described in Section 5.2 gives considerable savings compared to the standard finite element method but unfortunately, it is not enough to make the 3-D analysis of textile composites feasible. Given the length scales involved and the limitations on the element size, the mesh would require a huge number of elements. This would make generating the models extremely challenging, and analyzing the models practically impossible. Moreover, considering that the overall goal of this research effort is to couple the oxidation analysis with the damage progression analysis, the combination would be prohibitively expensive. In an effort to make this more

feasible, a decoupled subdomain strategy was developed to make the oxidation analysis more efficient.

The strategy applies to composite laminates that are exposed to oxygen from the top or bottom (or both) surfaces, but not the lateral surfaces. The strategy is illustrated in Figure 5.3, which shows a $1/8^{th}$ unit cell of a plain weave symmetrically stacked 2-ply laminate. The decoupled subdomain strategy takes the three-dimensional model and divides it up into individual analysis domains in the in-plane dimensions as shown in Figure 5.3. The strategy assumes that because of the boundary conditions applied on the model, the oxidation behavior will be such that the neighboring domains do not have an effect on each other, essentially assuming that oxygen does not flow from one domain to another. Therefore, the individual domains can be analyzed separately. Each individual domain is a three dimensional heterogeneous analysis region with curved material boundaries because of the undulation of the tows in the textile composite.

The strategy assumes that the change in the diffusivity due to the undulation is not significant because the rotation angles in actual composites are relatively small. The analysis also assumes that the undulations of the tows are not significant enough to cause an impact on the oxidation behavior. This assumption has been validated and is discussed in the next section. Based on this assumption, the individual 3-D domain can be converted into an equivalent domain with straight horizontal material boundaries based on the volume fraction of the different constituents in the domain as illustrated in Figure 5.3. Since the new equivalent domain has no inclined material boundaries, it can be analyzed with a simple 1-D model. Thus, the 3-D model shown in Figure 5.3 can be replaced by an array of 64 1-D models, thereby reducing analysis time significantly. The decoupled subdomain strategy is implemented in the finite element analysis package in such a way that the input to the model is the same as the conventional 3-D model. Additional pre-processing work is not required and the array of 1-D models is automatically generated and analyzed without the need for human interaction. Moreover, the 1-D models can be run in parallel on multi-core processors, thereby increasing the efficiency even further. This modeling strategy was validated by using a 2-D configuration. The validation including discussion of some of the oxidation behavior is described in the next section.

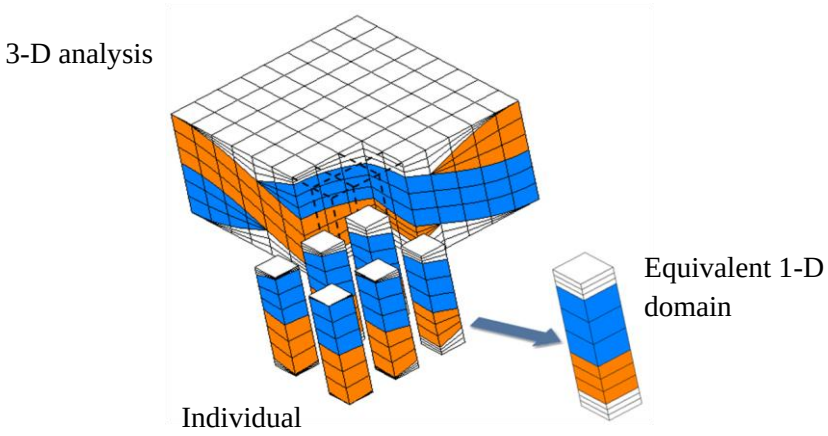

Figure 5.3: Schematic of hybrid model for analyzing textile composites

5.4. Use of approximate boundary conditions

Restrictions on element size, time step size, and longer analysis times proved to be computationally demanding. The unit cell for a symmetrically stacked plain weave is shown in Figure 5.4. In the case that the top and bottom surfaces are exposed to an oxidizing environment, one may exploit symmetries and reduce the size of the analysis region to 1/8 of a unit cell as shown in Figure 5.5. This reduction does not violate any of the boundary conditions imposed on the unit cell since symmetry is being exploited. Thus it is said to have "exact boundary conditions". However, element size restrictions combined with complex weave architecture still resulted in a highly refined mesh that made timely analysis prohibitive. Therefore, the analysis region was further reduced to 1/32 of the original unit cell size (see Figure 5.6). This further reduction significantly decreases the analysis region but does not allow for cross-flow of oxygen between regions as the 1/8 model does. Thus it is said to have "approximate boundary conditions". However, this may be an acceptable approximation if the cross-flow for particular configurations is minimal. Validation tests will assess the severity of this approximation. Figure 5.7 shows the typical mesh refinement that is used in an oxidation analysis which results in a relatively high number of degrees of freedom given the transient nature of the analysis.

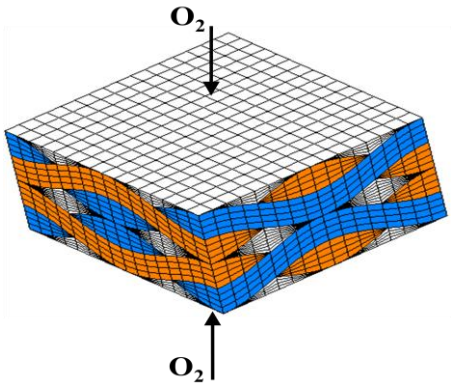

Figure 5.4: Description of plain weave unit cell

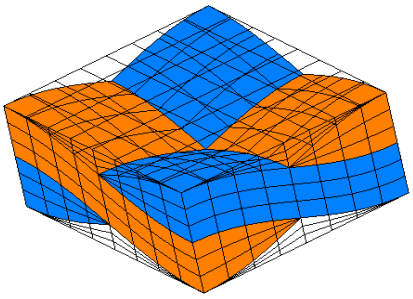

Figure 5.5: 1/8 unit cell compatible with exact boundary conditions

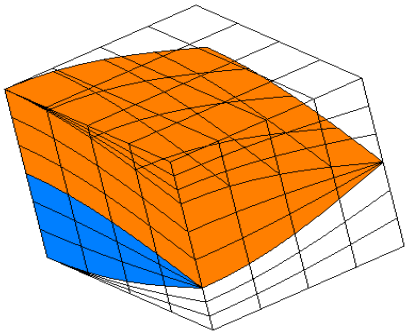

Figure 5.6: 1/32 unit cell compatible with approximate boundary conditions

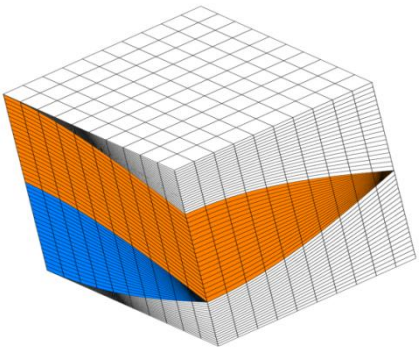

Figure 5.7: Typical mesh refinement for 1/32 unit cell (36000 DOF)

5.5. Adaptive time stepping

Manual time step specification and time step ramping allows for particular segments of a transient analysis to be performed with varying time step sizes which may be adjusted to maintain a desired level of accuracy (compared to a reference solution with relatively small time steps) while increasing the overall efficiency of an analysis. However, the drawback to manual time stepping is that previous knowledge of the transient behavior of a configuration is typically required. Furthermore, the optimal time stepping determined for one configuration may be different for configurations with different geometry or constituents.

Since manual time stepping may essentially require parametric studies to be performed to choose optimal parameters for a given configuration, an alternative approach is preferable. An adaptive time stepping approach that actively modifies time step size to maintain a maximum value of change in solution per time step can increase efficiency

while maintaining accuracy. The proposed adaptive time stepping algorithm ensures that the maximum change in any nodal value of the primary variable does not change by more than a user specified tolerance during a single time step. If a selected time step does not fulfill the requirement imposed by the tolerance, the time step is rejected and a new time step is selected based off of Eq.(5.1). This procedure is repeated until a successful time step is executed at which point the analysis continues.

The new time step is computed using Eq.(5.1) by multiplying the old time step by the ratio of the specified TOL and the maximum absolute change in the primary variable. The factor γ is used to increase the efficiency of the analysis and is set to 0.7 in the current implementation to slightly reduce the new time step with the goal of preventing unsuccessful time steps.

$$\Delta t_{new} = \gamma \, \Delta t_{old} \frac{TOL}{\max(|\Delta q|)} \tag{5.1}$$

5.6. Efficiency improvements

Even with optimization of element size and time step size through ramping or adaptive time stepping, the oxidation analysis of all but the simplest of configurations proved to be quite computationally intensive. Therefore, further increases in efficiency were sought. To this end, the code was re-examined for inefficiencies. Many modifications were made, but the most significant improvement came through the use of parallel algorithms and the exploitation of some characteristics of direct solvers.

5.6.1. Parallel algorithms

The relatively recent increase of parallel computing resources makes the use of parallel algorithms advantageous for increases in efficiency. The solvers which are available for oxidation analysis are parallel. Since the solving step is typically the most significant portion of analysis such a capability provides an obvious advantage over solving a system of equations in serial. The assembly of equations is typically the second most expensive portion of a finite element analysis. Parallel algorithms were developed using OpenMP, which also allow for the use of multi-point constraints.

The use of multi-point constraints creates an increased coupling in the system of equations for a finite element analysis. Typically coupling of equations is more or less governed by the connectivity of a mesh. However, multi-point constraints can couple two degrees of freedom which have no geometric connectivity from the mesh. Therefore, the typical use of domain decomposition to split the mesh between processors is not as useful when multi-point constraints are involved. Therefore, a new parallel algorithm was developed that would actually split the system of equations among the processors instead of the elements. Figure 5.4 visualizes the assignment of equations to four processors. While there may be some overlap in element calculations among the processors, this method ensures multi-point constraints will remain intact during parallel assembly.

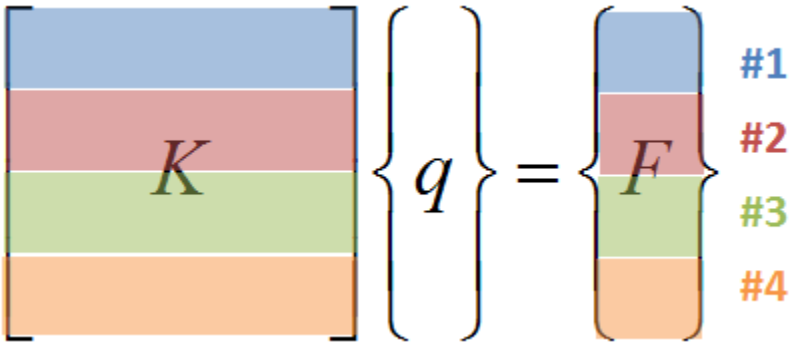

Figure 5.4: Assignment of equations to processors

With this methodology two parallel assembly algorithms were developed. The first algorithm is referred to as the "Elemental Storage Algorithm" (ESA). This algorithm splits the elements evenly among processors for calculation and stores the elemental data in memory. A second element list for every processor lists the elements required to assemble the equations assigned to that processor. There will typically be some overlap in the element list for assembly among the processors. However, there are no concerns regarding memory access since no processor will write to another processor's equations an no processor will calculate the same element as another processor. While it is possible that multiple processors could simultaneously access the stored elemental data from the calculation phase, there is still no concern since the processors will only be reading the same block of memory and not attempting to write to it. The elemental storage algorithm has the advantages of scaling very well with the number of processors since there is no overlap in the element calculations. Furthermore, no synchronization of the processors is required. However, storage of elemental data can be impractical for larger problems due to memory restrictions. This algorithm is best suited for small to moderate sized problems such as progressive damage or transient analysis. The elemental storage algorithm is currently implemented for oxidation analysis.

The second algorithm is referred to as the "On-the-Fly Algorithm" (OFA). As the name suggests, the calculation of elemental data is performed on the fly as needed for assembly and is not stored. Therefore, the same element could have calculations performed multiple times among the various processors. The possibility of multiple processors attempting to calculate the same element must be prevented by some synchronization steps which can reduce the efficiency of the algorithm. For small and moderate sized problems OFA does not scale as well as ESA with respect to the number of processors. However, as the problem size becomes larger there is significantly less overlap among processors and the speed up approaches that of ESA. Another advantage of OFA is that there are no memory concerns for larger models.

5.6.2. Exploitation of direct solvers

Direct equation solvers are commonly used for moderately sized system of equations and can offer good performance compared to an iterative solver for the same system of equations. For significantly larger systems (greater than 1 million unknowns), memory limitations often prevent the use of direct solvers, and iterative solvers can typically solve larger systems in less time than direct solvers. However, if the problem size permits the use of a direct solver, there are characteristics that may be exploited to further increase the efficiency.

A direct solver typically has three phases:

1. Reordering of equations
2. Factorization/decomposition of equations
3, Back substitution to solve the system of equations.

The first and last phases are typically cheaper than the second phase. Throughout the oxidation analysis, the left hand side matrix will be updated and change numerous times. Therefore the factorization and back substitution phases will be necessary for every solve step. However, the reordering phase depends more on the structure of the matrix than the actual values of the matrix. Since the general structure and sparsity of the matrix is dictated by mesh connectivity and boundary conditions this structure will remain constant throughout the typical analysis. Therefore, the reordering may be performed once and stored. This can be a significant portion of the analysis for larger systems.

5.7. Summary

This section has detailed some of the attempts and methodologies utilized to increase the efficiency of oxidation analysis. This includes concerns regarding the optimal element size and time step size along with the use of time step ramping to define different time step sizes over different segments of the analysis. An adaptive meshing strategy was also proposed that would essentially decrease the size of the system of equations depending on how far oxygen has diffused into the analysis region. In the case of textile composite oxidation analysis, a decoupled subdomain strategy was developed which converted a three-dimensional model into multiple one-dimensional domains. Use of approximate boundary conditions to reduce the problem size and expedite analysis was considered. To provide another time stepping alternative, an adaptive time stepping algorithm was proposed which would actively change the time step size while maintaining a minimum change in solution per time step. Finally, efficiency improvements including the use of parallel algorithms and the exploitation of direct solvers was discussed.

6. Validation of Strategies to Expedite Analysis

Section 5 discussed strategies to expedite oxidation analysis. This section discusses the validation that was performed on such strategies. Also, as discussed in Section 3 homogenized properties will be utilized in textile oxidation analysis due to the difficulty and expense of modeling the microstructure of textiles.

6.1. Optimal element size and time step size

Parametric studies were conducted to determine the optimal element size and time step size as well as the time step size ramping. In order to make comparisons, parametric studies were also conducted on corresponding diffusion models. Optimal element size and time step size were determined by analyzing the same configuration described in Section 5.1. The diffusivity of the material for this parametric study was assumed to be 53.6×10^{-6} mm^2/min, which is the diffusivity of the un-oxidized PMR-15 resin. It is important to note that this parametric study is not extensive and does not look all the possible parameters. Therefore, the results from this parametric study, in essence, are valid only for material properties and other model parameters used in the study. In order to analyze other material systems, it would be advisable to determine the optimal parameters for that specific system.

One-dimensional models were analyzed using various element sizes and time step sizes. The reference solution was assumed to be that obtained from using linear elements with a size of 1 micron and a time step size of 0.15 minutes. The variation of average concentration in the model with time was compared for the different models. It was observed that the effect of the element size and time step size on the results were independent of each other. The element size was kept constant at 1 micron and models were analyzed with varying time step sizes and it was found that the time step size could be raised to over 10 minutes before any noticeable difference in the results were observed. When the time step size was kept constant at 0.15 minutes, the element size could be increased to at least 40 microns without any noticeable change in the results. A model with an element size of 40 microns and a time step size of 10 minutes also yielded the same behavior as the reference model. This behavior was seen for both linear and quadratic elements. In some instances, the nodal concentrations drop below zero but they are still considered numerical zeros and these negative concentrations do not have any significant effect on the results. The same results were obtained when a parametric study was conducted on two dimensional models with eight-node quadratic elements. A parametric study was also conducted to determine the effect of diffusivity on the allowable time step size. As expected, when the diffusivity is increased, the oxygen takes less time to saturate the material and the optimum time step size required in order to get a converged solution becomes smaller. It was also found that increasing the element size while keeping the time step size and diffusivity constant, eventually results in negative nodal concentrations.

Similar to what was done for the diffusion analysis, the optimal mesh size and time step size were determined by analyzing the configuration described in Section 5.1 using the

material properties in Table 5.1. The reference solution was assumed to be that obtained from using linear elements with a size of 1 micron and a time step size of 0.15 minutes. The oxidation layer thicknesses were calculated for all the models and compared to determine the accuracy. The oxidation layer consists of a fully oxidized layer (Zone I) and the active reaction layer (Zone II). Although the Zone II layer is defined by having an oxidation level in between 0 and 1, for all the oxidation models described in this paper, a tolerance of 1% is allowed on those limits. Therefore, an element is assumed to have started oxidizing and is in Zone II if the oxidation level at each of the material integration points falls within a lower limit of 0.01 and an upper limit of 0.99. If the oxidation state is above 0.99, the element is assumed to be un-oxidized and if it is below 0.01 it is assumed to be fully oxidized. A post-processing routine was written that calculated the growth of the oxidation layer along a line in a model. This involved extrapolating the oxidation state values from the integration points to the nodal points, averaging the extrapolated values at a node if the node shared elements of the same material and solving for the location on the prescribed line where the oxidation level value met the specified upper and lower limits.

Figure 6.1 shows the effect of the size of linear elements on the oxidation layer growth with a constant time step size of 0.15 minutes. It shows that the models using 4-micron and 8-micron size elements closely agree with the model using 1-micron elements whereas the model using 12-micron elements over predicts the thickness. The model with 8-micron elements shows a distinct oscillation in the curve. This is believed to be caused due to errors from extrapolation of the oxidation state values from the integration points to the nodal points. Nevertheless, it can be seen that upper bound of the curve is very close to the results of the 1-micron size model. The model with 4-micron elements shows slight oscillations as well but it is able to predict the thickness growth very well.

The effect of the time step size was also investigated by keeping the element size constant and varying the time step size. Figure 6.2 shows the oxidation layer growth for different models when the element size is kept constant at 2 microns and the time step size varies from 0.15 mins to 0.8 mins. It can be seen that the time step size can be doubled from 0.15 mins to 0.3 mins without any perceivable effect on the results. When the time step size is raised to 0.5 mins, some difference can be seen in the initial part of the simulation while the latter part still predicts the oxidation growth fairly well. Increasing the time step size to 0.8 mins affects the results considerably especially during the initial part of the simulation. This kind of behavior for the effect of time step size on the predicted oxidation growth was seen for both linear and corresponding quadratic elements. The trends also show that the time step size is more critical to the initial part of the simulation where the oxidation growth is nonlinear. For many of these models, the nodal concentrations calculated would be numerical zeroes that go below zero. When the program encounters such values, they are converted to zero so that it

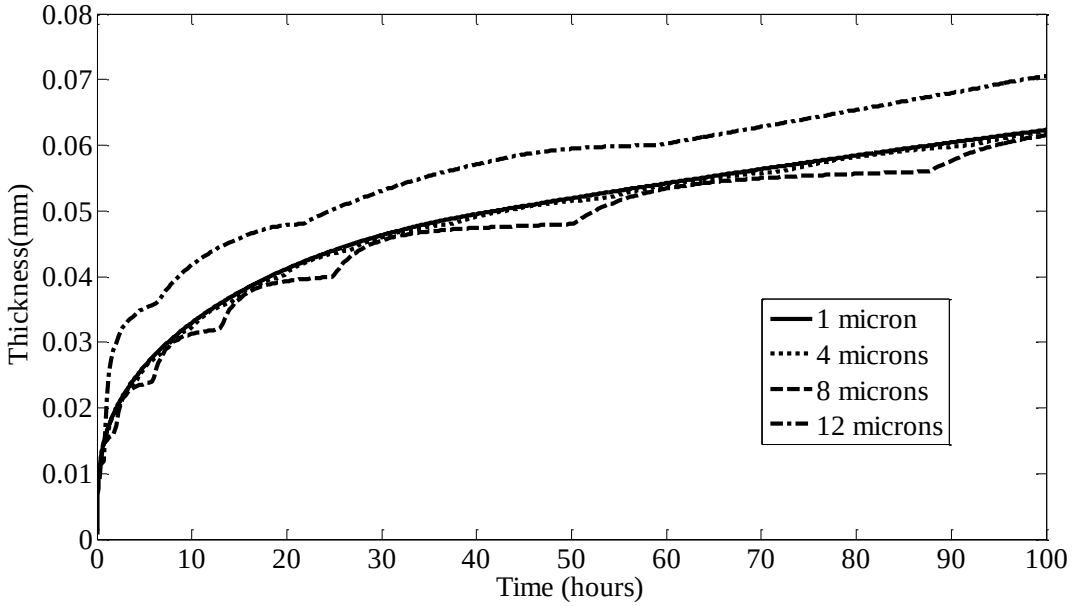

Figure 6.1: Effect of element size on oxidation layer growth (Zone I+II) for neat resin (using linear elements and time step size of 0.15 mins)

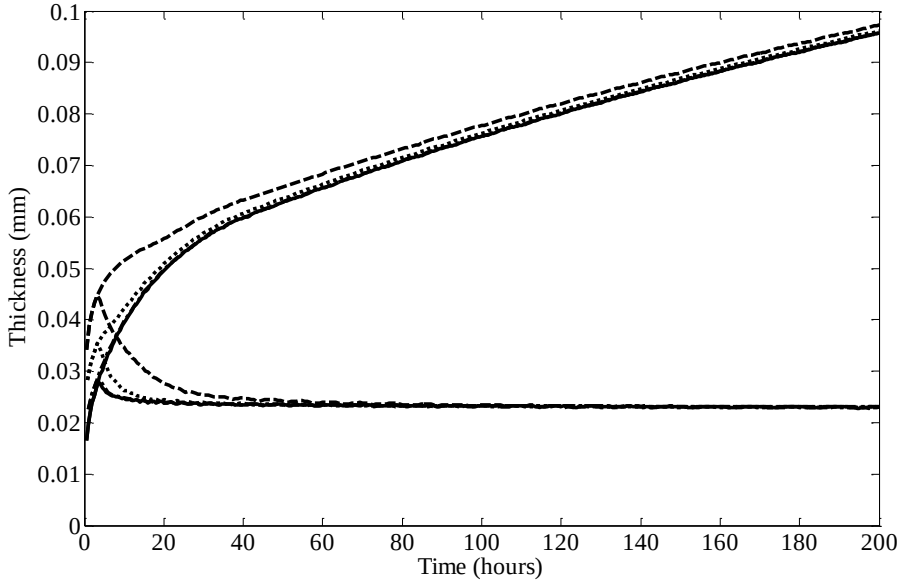

Figure 6.2: Effect of time step size on oxidation layer growth for neat resin (using 2 micron linear elements)

does not use negative concentrations in the calculation of the reaction terms and the oxidation state, which would physically mean a reversal of the oxidation process.

In order to speed up the analysis, the behavior of the model when the time step size is gradually increased was investigated. As seen from the results of the previous parametric study, a time step size of no more than 0.3 minutes was required to accurately model the initial part of the simulation where layer growth is highly nonlinear. The layer growth behavior becomes close to linear once the model has undergone oxidation for 40 hours, which is when the time-dependent material property, α changes from decreasing linearly with respect to time to a constant value of 0.0033. Based on this, a parametric study was conducted where the models used a time step size of 0.3 mins for the initial 40 hours of the simulation and for the other 160 hours, the different models used different time step sizes. The reference model used a time step size of 0.15 mins for the entire 200 hours. All the models used elements with a size of 2 microns. Figure 6.3 shows that when the time step size is ramped up from 0.3 minute to 1 minute, the predicted oxidation growth curve is barely distinguishable from that of the reference model. The results are fairly reasonable even when the time step size is ramped up to 5 mins. As shown in Figure 6.3,

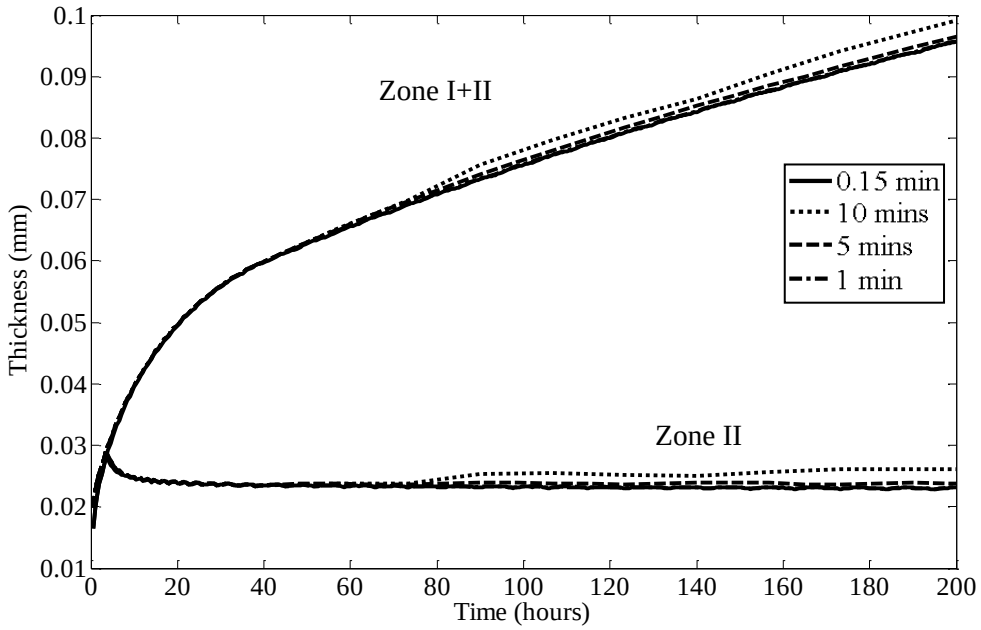

Figure 6.3: Oxidation layer growth (Zone I+II, Zone II) for neat resin (using 2 micron linear elements and time step size of 0.30 mins for the first 40 hours and different ramped time step sizes thereafter)

the differences in the curves are considerable when the time step size is ramped to 10 mins. Figure 6.3 show that the models also predict the Zone II thickness fairly well. Ramping up the time step size tremendously reduces the computational time required for the analysis compared to using a constant time step size of 0.3 minutes. A constant time

step size of 0.3 mins used for simulating 200 hours of oxidation takes up 40,000 time steps whereas using a model that uses 0.3 mins for the first 40 hours and 5 mins for the remaining 160 hours takes up only 9920 time steps. This makes a computational savings of over 75%.

6.2. Adaptive meshing strategy

Parametric studies were performed to determine the optimal parameters for the Adaptive Meshing Strategy as well as potential computational savings. The one-dimensional configuration in section 5.1 is analyzed using the Adaptive Meshing Strategy described in Section 4.2. The two parameters that were varied were C^0 and N. All the models in this particular parametric study use 1 micron size elements and time step size ramping where the first 40 hours use 0.3 minute time steps and the remaining 160 hours use 1 minute time steps. The oxidation layer growth from the different models is compared with a reference model that uses the standard oxidation analysis. Figure 6.4 shows the oxidation layer growth for models that have a constant C^0 of 0.01 and three different N values of 50, 100 and 200. It shows that for N values of 50 and 100, the oxidation layer growth predicted is very close to that of the reference model. Even for the model with an N value of 200, it is seen that there is close agreement till about 40 hours after which the time step size is ramped up to 1 minute. This indicates that the value of the threshold concentration, C^0 is too high and that the oxidation front is creeping up to the constrained region and the active region of the mesh is not re-evaluated quickly enough. That is why for lower N values such as 50 or 100, the prediction of oxidation layer growth is much better. This means that if the threshold concentration, C^0 is lowered, that would make the constrained region smaller thereby taking it longer for the oxidation front to reach the region. Therefore, lowering C^0 should allow increasing N while maintaining the accuracy. This was validated by analyzing a similar set of models as earlier except with a C^0 value of 1e-3. Figure 6.5 shows that N value of 200 does a very good job of predicting the oxidation layer growth whereas when C^0 had a value of 1e-2, an N value of 200 did a very poor job of predicting the layer growth. Moreover, even an N value of 300 does a good job and it is only when it is increased to 400 that the accuracy of the prediction even starts to deteriorate. This same trend was seen when the C^0 was lowered even further to 10^{-4} and 10^{-5}. On the other hand, when C^0 is lowered, the constrained region is reduced and the maximum potential of the Adaptive Meshing Strategy is not achieved. Figure 6.6 shows computational time savings achieved when the Adaptive Meshing Strategy compared to the corresponding standard analysis with time step size ramping. The computation time savings is defined by using

$$\text{computational time savings} = \left(1 - \frac{\text{time taken by Adaptive Meshing Strategy}}{\text{time taken by standard analysis}}\right) \times 100$$

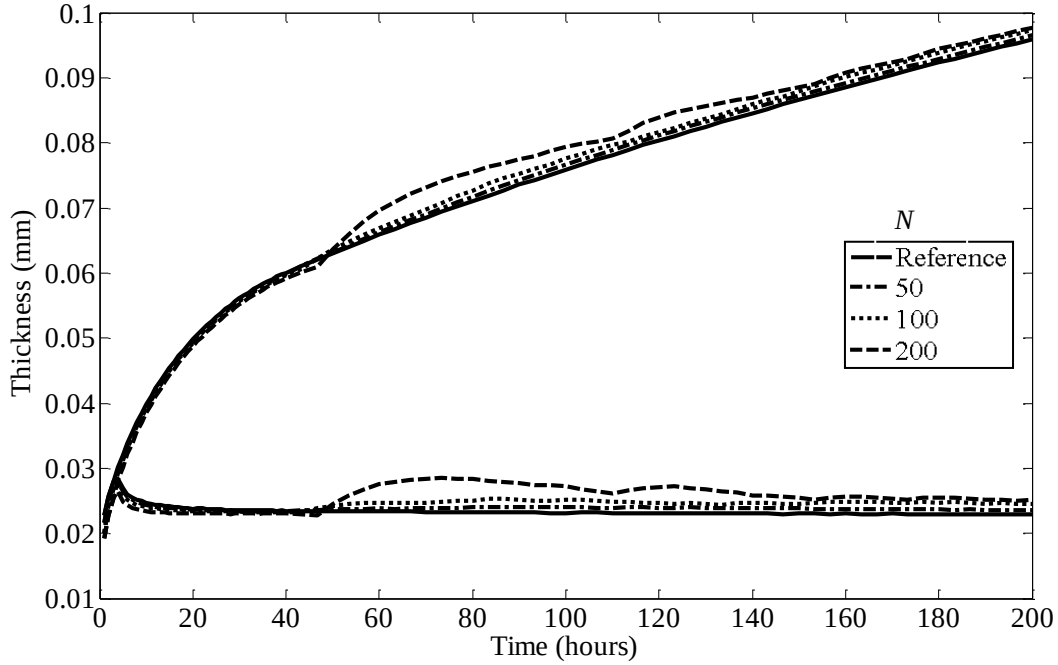

Figure 6.4: Oxidation layer growth (Zone I+II, Zone II) for neat resin (using $C^0=10^{-2}$ and different N values)

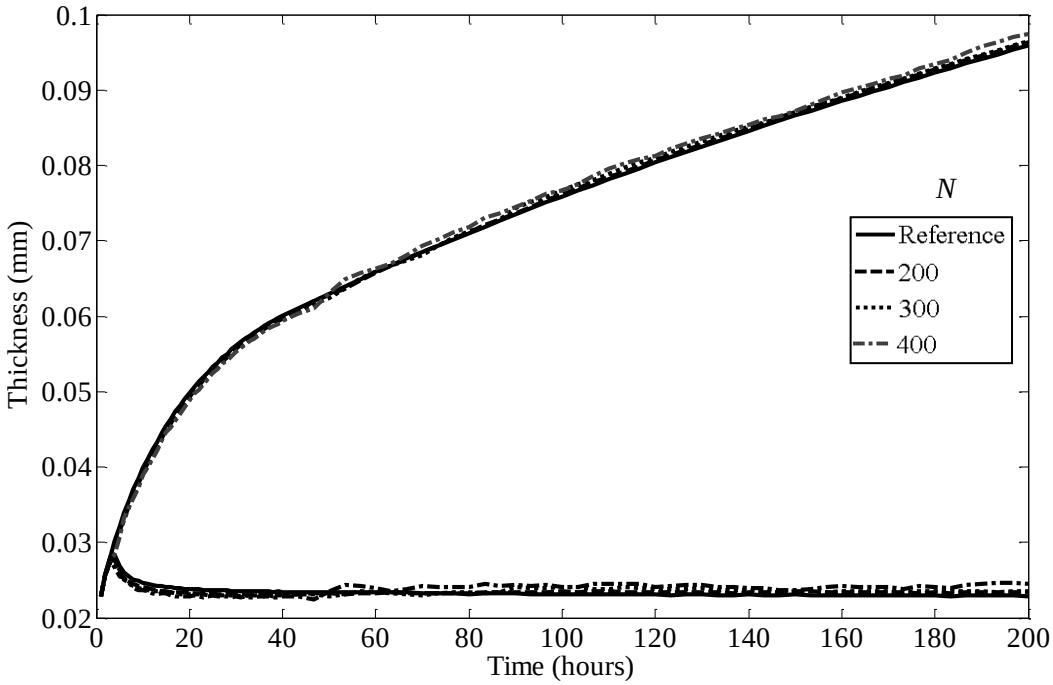

Figure 6.5: Oxidation layer growth (Zone I+II, Zone II) for neat resin (using $C^0=10^{-3}$ and different N values)

Due to constraints with the computational resources, it was not possible to obtain accurate timings of the analysis but it still gives a good sense for the trends in the savings achieved when the value of C^0 is lowered. As illustrated in the figure, as the value of C^0 is lowered from 1e-2 to 1e-5, the computation time savings decreased from ~68% to ~58%.

In order to see how this analysis strategy fares when the dimensionality of the model is increased, the same configurations were analyzed using 2D and 3D models. The 2D mesh had dimensions of 200 x 10 elements using 8-noded 2D elements of size 1 micron. The 2D model had a total of 6421 DOFs. The 3D model had dimensions of 5 x 5 x 200 elements using 20-noded brick elements of size 1 micron. The 3D model had a total of 26496 DOFs. Again constraints on the computational resources prevented accurate timings of the analyses but it did give the same kind of trend for all the models analyzed. Figure 6.7 shows the computational time savings achieved when C^0 was kept at a constant value of 1e-3 and the value of *N* has been varied for the corresponding 1D, 2D and 3D models. The results were not conclusive enough to determine any strong trends. In general, it was seen that the percentage savings reduced for the 2D model compared to the 1D model. On the other hand, the 3D models generally gave a better percentage savings compared to the 1D models. It is estimated that this trend is due to the nature of the system of equations related to 1D, 2D and 3D models. For all the analyses performed in this work other than this parametric study, C^0 was chosen to be 0.0001 mol/m^3 and *N* was chosen to be 20 time steps.

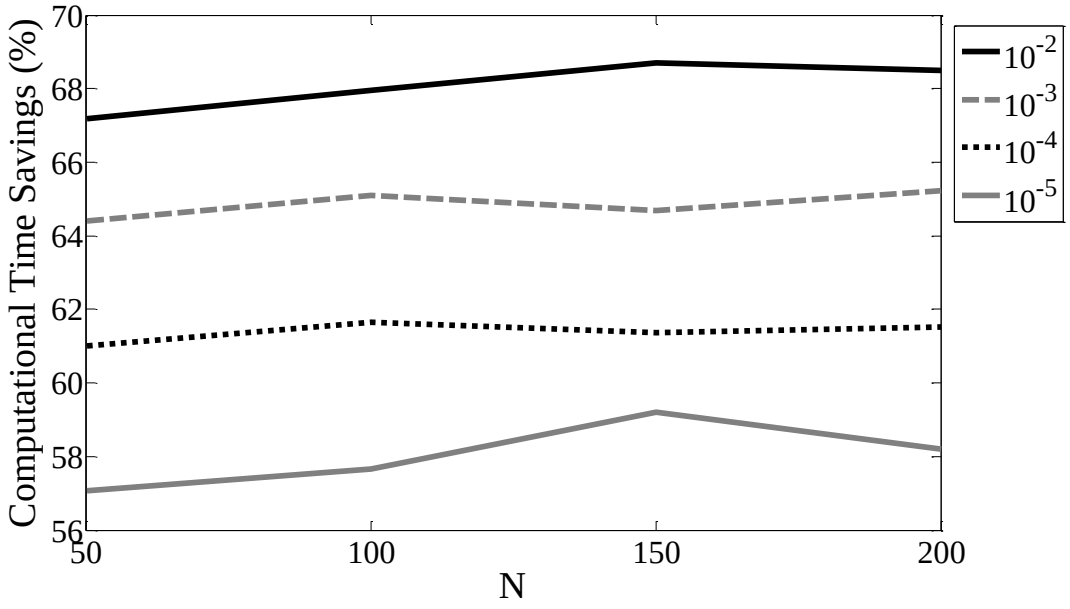

Figure 6.6: Computational time savings for parametric study of 1D expedited analysis models with various C^0 and *N* values)

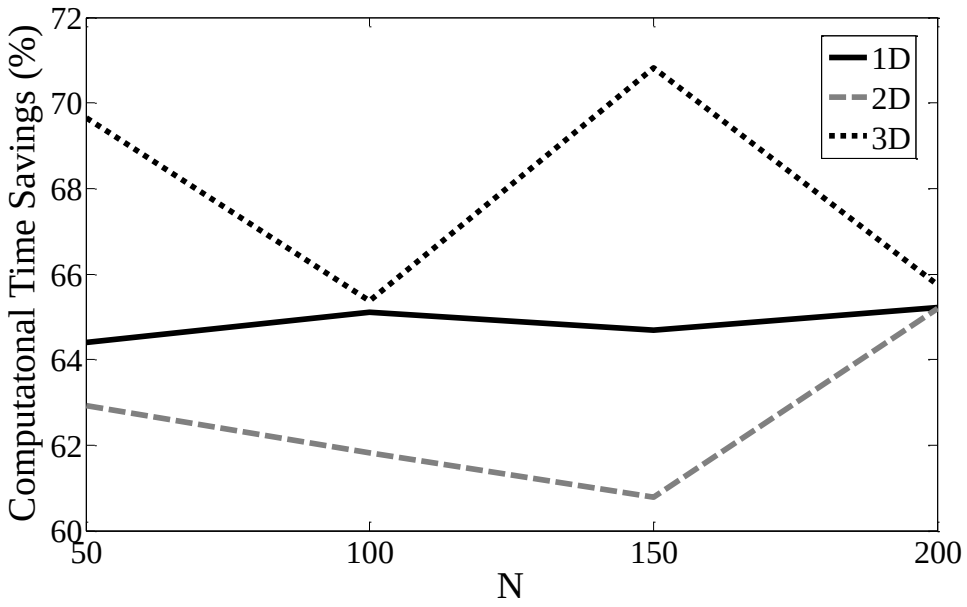

Figure 6.7: Computational time savings for parametric study of 1D, 2D and 3D expedited analysis models with $C^0=10^{-3}$ and various N values)

6.3. Decoupled subdomain strategy

The decoupled subdomain strategy was examined to assess the ability of the method to characterize a two-dimensional or three-dimensional oxidation analysis through the use of multiple one-dimensional domains. At the time the method was developed, a two-dimensional validation was performed since the initial efficiency of the implementation prohibited oxidation analysis of three-dimensional weave models. However, recent advancements in the efficiency have allowed for this method to be validated against three-dimensional results. It was found the decoupled subdomain strategy predicts the results of an oxidation analysis very well compared to a three-dimensional solution.

6.3.1. 2D Validation

A simple 2-D heterogeneous configuration with two materials was chosen where the material boundary is straight but at an angle to the horizontal edge as shown in Figure 6.8(a). The bottom edge is assumed to be exposed to oxygen whereas the other three edges are assumed to be impermeable. The configuration has the dimensions 200 microns x 100 microns. The material in the lower region is assumed to be neat PMR-15 resin and the other material is assumed to be a homogenized graphite/PMR-15 tow with a fiber fraction of 55.6%. The 2D plane in the configuration is assumed to be the plane perpendicular to the fiber axis in the tow and therefore only the transverse diffusivities of the tow will be used in the 2D analysis. The material properties of the tow are

calculated using the formulas described in Section 3.4.7. The material properties of the resin are given in Table 5.1 and that of the homogenized tow using the aforementioned formulas are given in Table 6.1. The region is first divided into two domains and

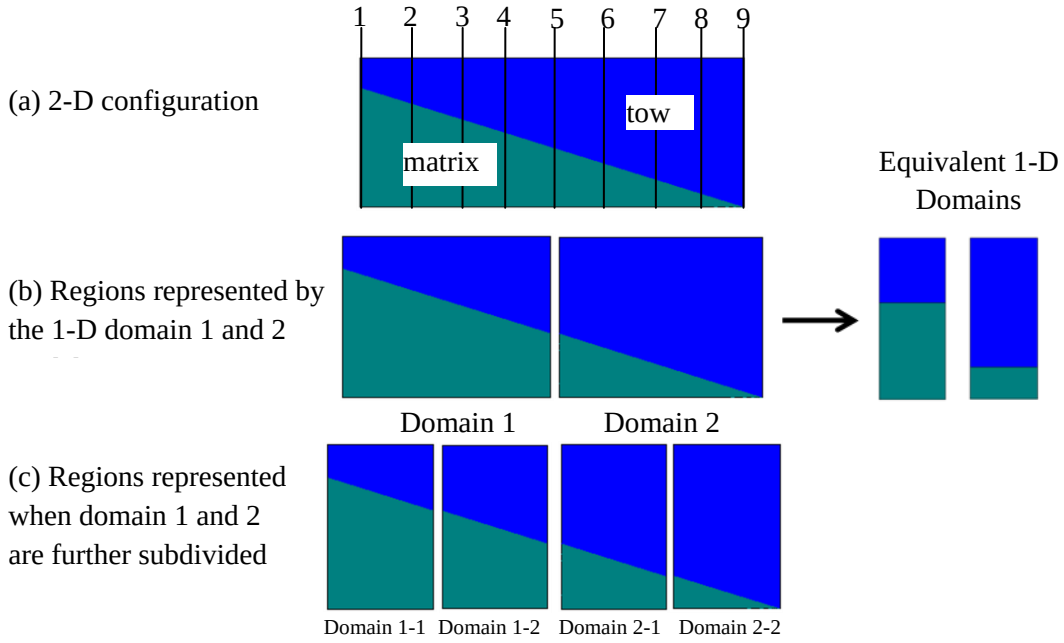

Figure 6.8: 2-D configuration for validating hybrid model

converted into equivalent 1-D models as shown in Figure 6.8(b). To compare the oxidation layer growth predicted by the 1-D models with the behavior in the actual 2-D model, the oxidation layer growths along different vertical lines (numbered in Figure 6.8(a)) in the 2-D model are compared. Figure 6.9(a) plots the oxidation growth given by the equivalent 1-D domain 1 model along with that along lines 1, 3 and 5. It shows that the 1-D result agrees very closely with that of line 3 and not so much with that of lines 1 and 5, which are on the extreme edges of domain 1. Similar trends are seen in Figure 6.9(b), which shows corresponding plots for domain 2. The domains are then further subdivided into domains 1-1, 1-2, 2-1 and 2-2 as shown in Figure 6.8(c). The corresponding oxidation growth plots for domains 1-1, 2-1, 1-2, and 2-2 are shown in Figure 6.9(c), (d), (e), and (f) respectively. As expected, these results show that the equivalent 1D domain models perform better at simulating the oxidation layer growth when the domain size is reduced.

Table 6.1: Oxidation material properties for the homogenized tow (V_f=55.6%)

	Homogenized tow (Vf=55.6%)
Transverse Diffusivity D_{unox} D_{ox}	33.07 x10^{-6} mm^2/min 48.27 x10^{-6} mm^2/min
R_0	1.554 mol/(m^3min)
ϕ_{ox}	0.639
C^{∞}	0.3507 mol/m^3
α	0.01-0.0067(t/40) : t < 40 0.0033 : t > 40 (t in hours)
$f(C)$	$\frac{2\beta C}{1+\beta C}\left[1-\frac{\beta C}{2(1+\beta C)}\right]$
β	0.919

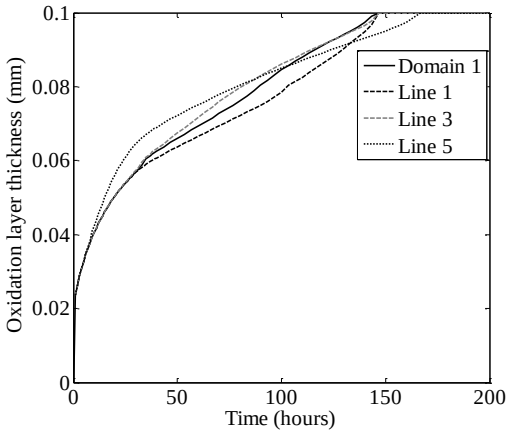

(a) Domain 1

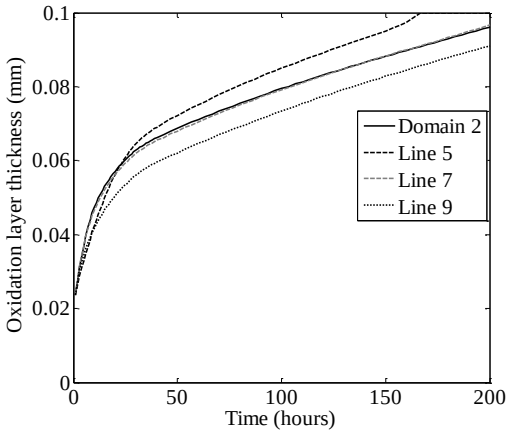

(b) Domain 2

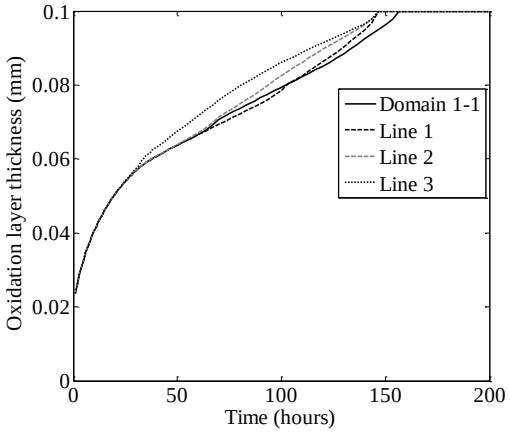

(c) Domain 1-1

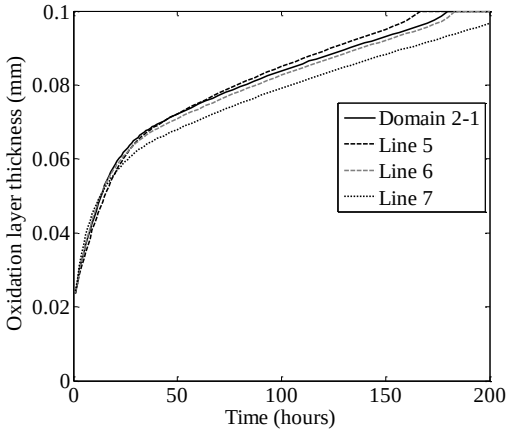

(d) Domain 2-1

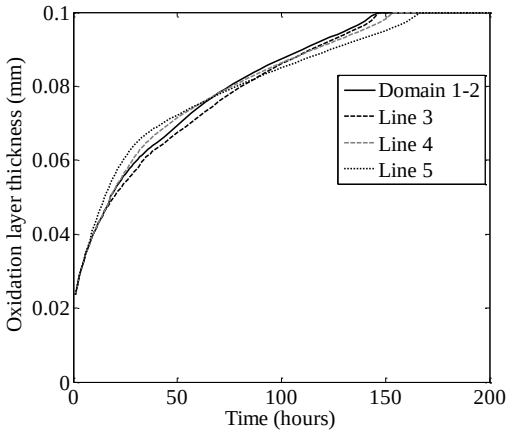

(e) Domain 1-2

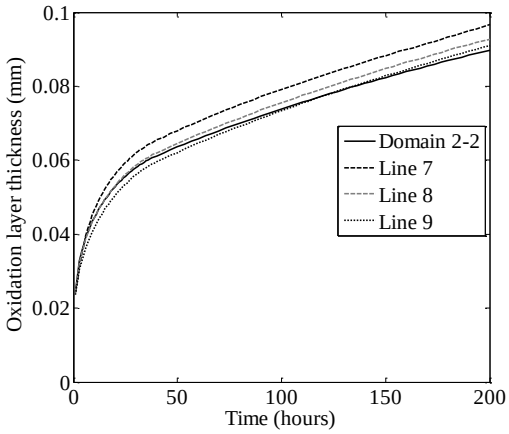

(f) Domain 2-2

Figure 6.9: Comparison of the oxidation layer growth from the different 1-D models with the growth in the 2D configuration

One interesting behavior that was noticed during the validation was that when simulating oxidation of a heterogeneous model with neat matrix and tow, the predicted oxidation growth seems counter-intuitive when compared to that of a model with neat matrix alone. Consider the equivalent 1-D configuration for domain 1 shown in Figure 6.10, which is a heterogeneous model with neat resin and homogenized tow. Figure 6.11 compares the predicted oxidation layer growth for the configuration in Figure 6.10 with that of a pure resin model. One would intuitively expect that since the model with the tow is assumed to have inert and impermeable fibers, this would slow down the oxidation layer growth compared to a neat resin model that has no fibers. But Figure 6.11 shows that the model with the resin and tow has a faster oxidation layer growth.

Figure 6.10: Equivalent 1D configuration for domain 1

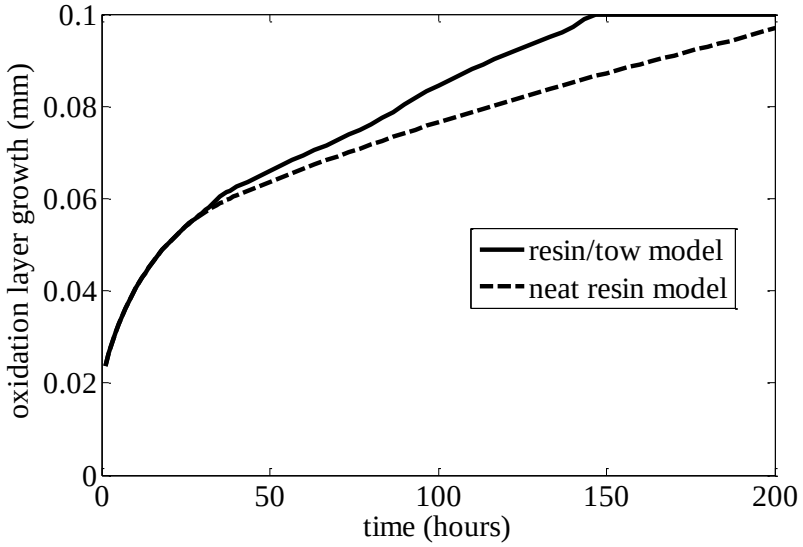

Figure 6.11: Comparison of oxidation layer growth in the domain 1 (resin/tow) model and neat resin model

On further investigation, it was seen that a number of factors influence this behavior. The tow in the model acts like a pseudo-barrier allowing the resin to saturate with oxygen much faster than the tow. Until the oxidation front reaches the vicinity of the material boundary, both the models behave in the same manner because the tow has no

effect on the matrix that is being oxidized ahead of it. But once the tow begins to oxidize as well, the interface conditions regulate the flow of oxygen from the matrix into the tow and free oxygen starts to build up in the matrix. This is evidenced in Figure 6.12 which shows the oxygen concentration profile in the model at 100 hours. Figure 6.12 shows that the resin region in the resin/tow model (from 0 to 0.06 mm) has more oxygen than the same region in the neat resin model. The oxygen in the tow region (from 0.06 to 0.1 mm) is also more than that in the same region for the neat resin model. This could be due to a combination of factors. First, note that at 100 hours, the oxidation front has crossed the material boundary but is not too far from it. The material boundary is at 0.06mm and the oxidation front at 100 hours can be considered to be around 0.08mm, beyond which the oxygen concentration is practically zero. Secondly, the tow has less amount of resin that can be oxidized and therefore the maximum reaction rate is also less than that of the neat

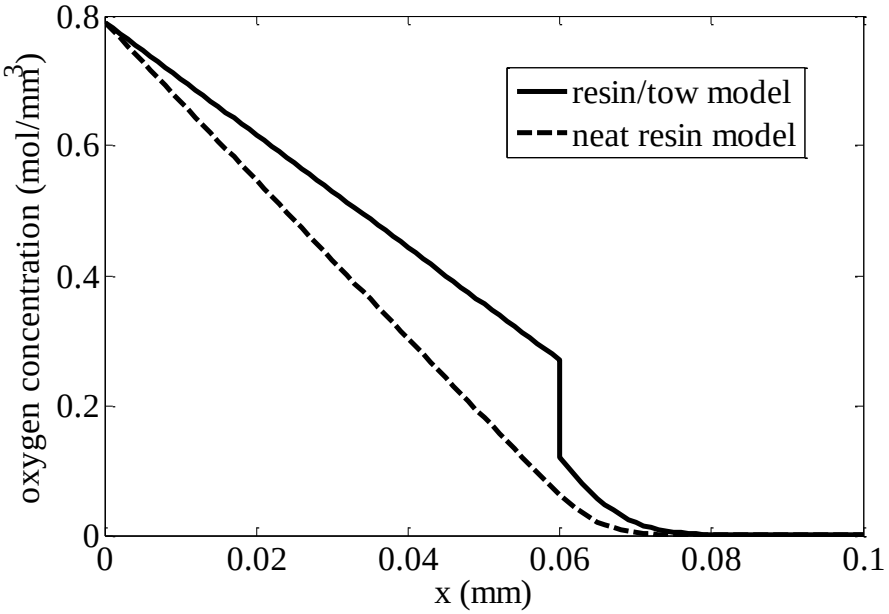

Figure 6.12: Comparison of concentration profile in the resin/tow model and neat resin model at 100 hours

resin. That also means that the region consumes less oxygen (for oxidation) than the neat resin. Since the reaction rate in the tow is less than that in the neat resin and the oxidation front is fairly close to the material boundary, the tow region between the material boundary and the oxidation front also starts accumulating more oxygen than the corresponding region in the neat resin. Figure 6.13 gives the amount of free oxygen in the model throughout the simulation. It shows that until about 60 hours, the resin/tow model and the neat resin model have the same amount of free oxygen, but after 60 hours the

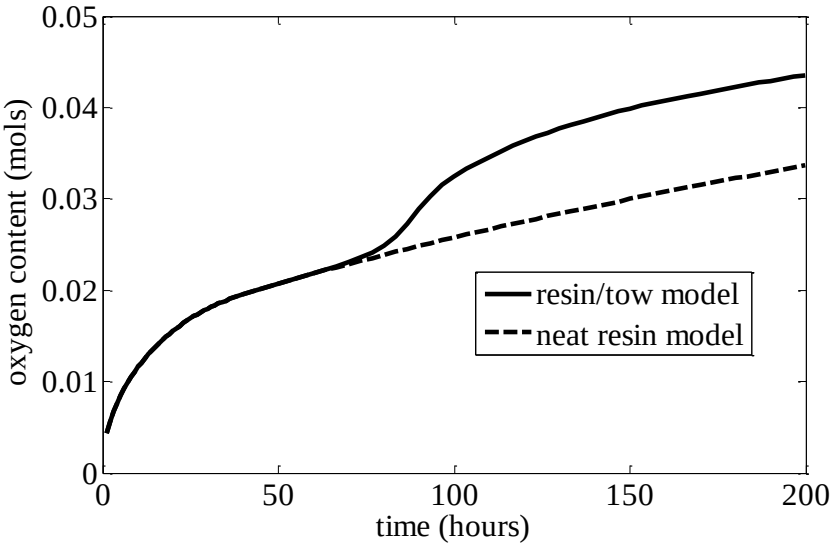

Figure 6.13: Comparison of amount of free oxygen in the resin/tow model and neat resin model

resin/tow model builds up more oxygen in its material. This is not to be confused with the amount of oxygen consumed in oxidizing the polymer in the resin and tow regions. The neat resin model is expected to consume more oxygen than the resin/tow model because it has more material that can be oxidized and this is shown in Figure 6.14. Once the oxygen starts to build up in the matrix, it becomes fully oxidized more quickly and all the incoming oxygen is directed into the tow region, which is then used up to oxidize the polymer in the tow. Also note that an oxidation level of 0.99 at a material point in the neat resin region indicates that 1% of the resin in the material has oxidized. On the other hand, saying that 1% of the resin in a material point in the tow region corresponds to an oxidation level defined by Eq.(3.99), which for this model is 0.99556. Figure 6.15 shows the oxidation level profile in the model at 100 hours. The inset plot in Figure 6.15 shows a close up of the oxidation state of the two models between 0.08mm and 0.095mm. It shows that the oxidation level in the resin/tow model dips below 0.99556 at about 0.085mm (at location A) whereas in the neat resin model, it dips below 0.99 at about 0.077mm (at location B). This snapshot of the simulation at 100 hours shows what the oxidation profile in the two models looks like when the oxidation layer thickness in the resin/tow model is larger than that in the neat resin model. Overall, this oxidation behavior in the resin/tow model is due to a combination of factors such as the effective oxidation properties of the tow as well as the diffusion behavior in heterogeneous models and the relatively slow movement of the oxidation

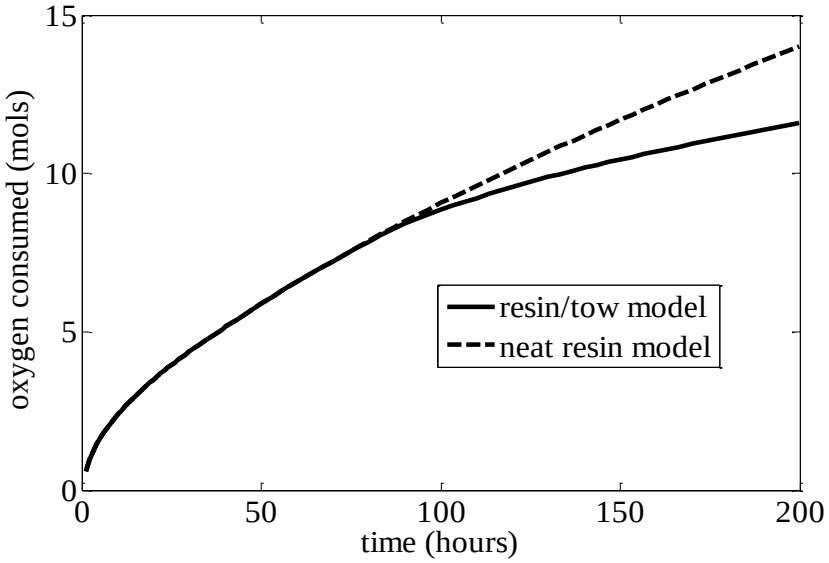

Figure 6.14: Comparison of amount of oxygen consumed in the resin/tow model and neat resin model

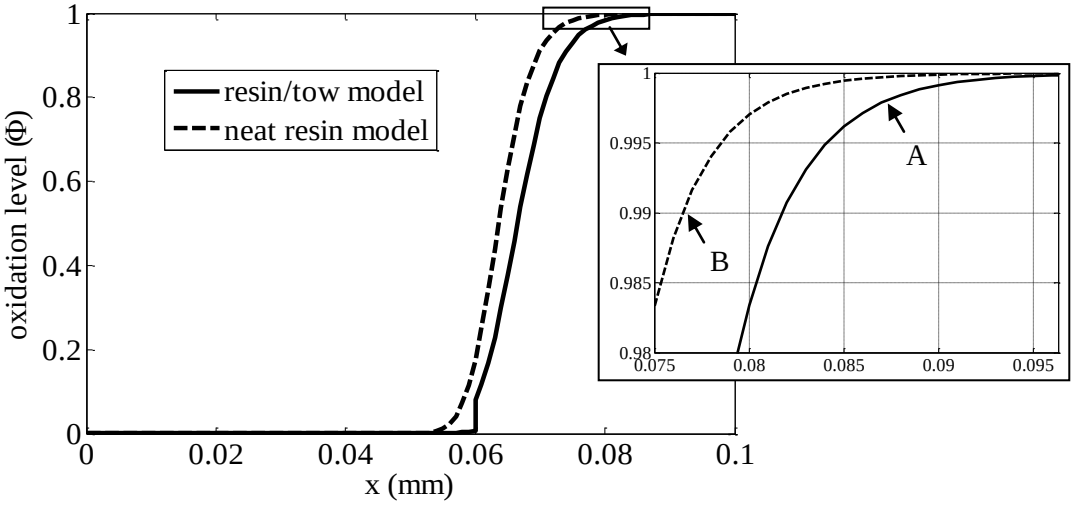

Figure 6.15: Comparison of oxidation level (Φ) profile in the resin/tow model and neat resin model at 100 hours

front into the interior of the material. It would also depend on the volume fraction of the constituent materials and the configuration of the materials in the heterogeneous model. Therefore, the location of the material boundary in the configuration also has an impact on the oxidation behavior.

6.3.2. 3D Validation of DSS and use of approximate boundary conditions

Increases in efficiency made oxidation analysis of three-dimensional weave models feasible. However, analysis still came with significant computational expense. Therefore, an approximate boundary condition strategy was utilized to reduce the problem size to approximately 1/4 of that using exact boundary conditions. Figure 5.4 shows a unit-cell for the configuration of interest for oxidation analysis of a plain weave 2-ply symmetric laminate. Oxygen is entering from the top and bottom surfaces and all other surfaces have zero flux due to periodicity. Figure 5.5 shows the analysis region (1/8 unit cell) with exact boundary conditions once symmetries in the configuration are exploited. Here oxygen is flowing from the top surface and all other surfaces have zero flux due to symmetry. Figure 5.6 shows the 1/32 unit cell using approximate boundary conditions assuming all surfaces except for the top have zero flux. Note that oxidation meshes used were much more refined than that shown in Figures 5.6 and 5.7. This was done to more clearly illustrate tow architecture. Figure 5.8 shows a typical mesh refinement used for oxidation analysis of a three-dimensional weave model. This mesh contains a maximum element thickness of 5 microns, resulting in approximately 36000 degrees of freedom (DOF).

With results available for a three-dimensional weave model, the approximate boundary condition strategy, as well as the previously developed decoupled subdomain strategy can now be evaluated. For the oxidation analysis of textile composites, the oxidation layer growth (essentially how deep oxidation is occurring in the composite with time) is determined along various lines through the thickness. The oxidation envelope is defined as the minimum and maximum oxidation layer thickness at a given time. Figure 6.16 shows the comparison of oxidation envelopes for a 2-ply symmetric plain weave laminate.

The relative difference between the minimum and maximum oxidation layer thickness that remains approximately constant with respect to time up to 160 hours. At 50, 100, and 150 hours the maximum layer thickness increases 28-29% over the minimum layer thickness. At 200 hours the maximum layer thickness increases 37% over the minimum layer thickness. However, note that after 160 hours there is a sharp increase in the maximum oxidation layer thickness. This is believed to be due to mesh refinement and weave architecture in a certain region. More refined meshes will need to be analyzed to investigate oxidation behavior in this region.

The results for exact boundary conditions, approximate boundary conditions, and the decoupled subdomain strategy agree remarkably well. While there are noticeable differences in the distributions, it is emphasized that these differences are typically less than the maximum element thickness used in a model. Therefore, more mesh convergence studies should be conducted before trying to explain the relatively minimal differences in oxidation layer growth distributions. The three-dimensional results also serve to assess the severity of the assumptions in the decoupled subdomain strategy. Considering all of the uncertainties in this complex process, the highly efficient

decoupled subdomain strategy yields results that should be considered quite acceptable for the current configuration. Also, if more accurate results are required, the decoupled subdomain strategy provides a quick way to identify the most important cases to study further with fully 3-D analysis.

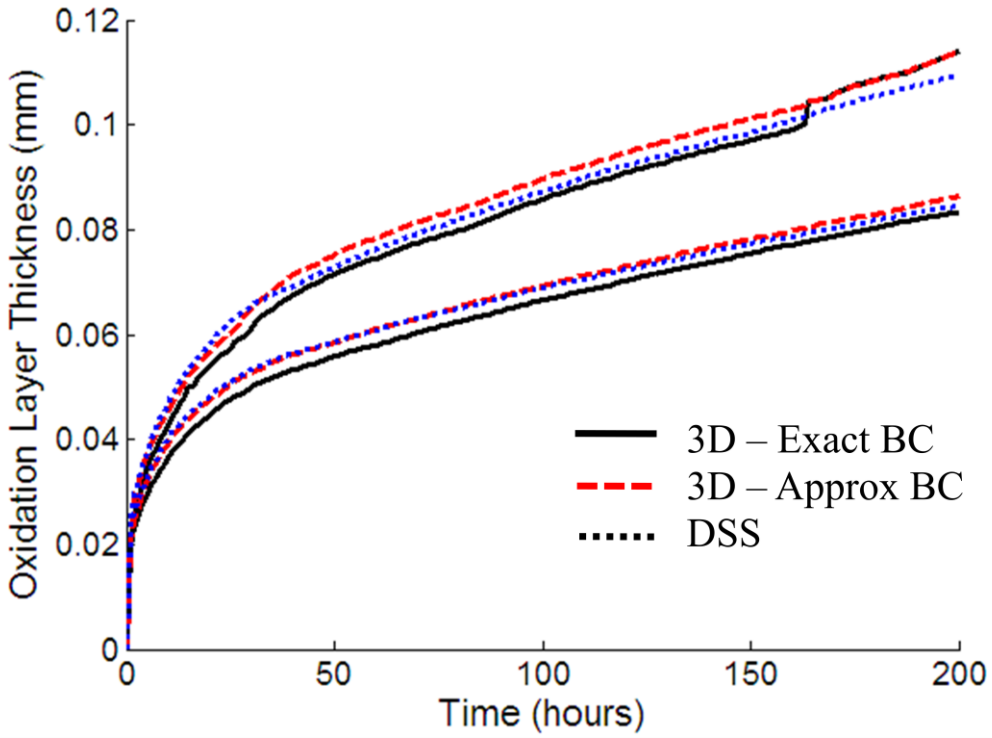

Figure 6.16: Comparison of oxidation envelopes for a plain weave laminate up to 200 hours

6.4. Mesh convergence study for 3D analysis

With efficiency increases allowing three-dimensional analysis of textile composites, a mesh convergence study was in order. While 3D analysis was still time consuming, a few mesh refinements were considered to study the effect of refinement on the predicted behavior. Figure 6.17 shows the meshes considered for a convergence study. These meshes are characterized by the maximum dimensions of an element in the mesh. For example, a mesh characterized by "10 x 15 μm" will have elements with in-plane dimensions of 15 x 15 μm and a maximum element thickness of 10 μm. The metric used to measure convergence was the oxidation envelope that was used in the comparison of exact and approximate boundary conditions in the previous section. Figure 6.18 shows a comparison of oxidation envelopes for the meshes shown in Figure 6.17. All the meshes show approximately the same response to oxidizing environment with regards to the oxidation envelope. There is a larger deviation for the coarsest mesh (10 x 15 μm)

beyond 150 hours, but this deviation is relatively minimal. Thus, the mesh shown in Figure 6.14a will likely be sufficient for oxidation analysis of a plain weave composite.

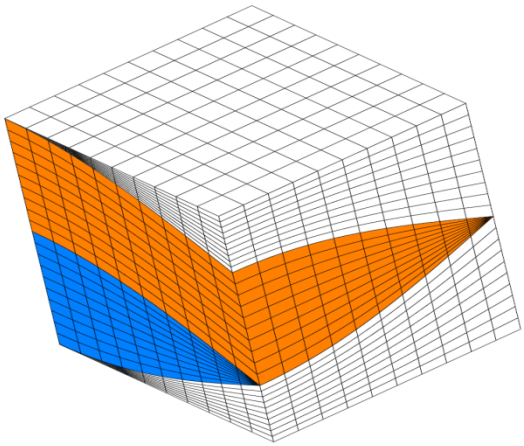

a). 10 x 15 μm mesh

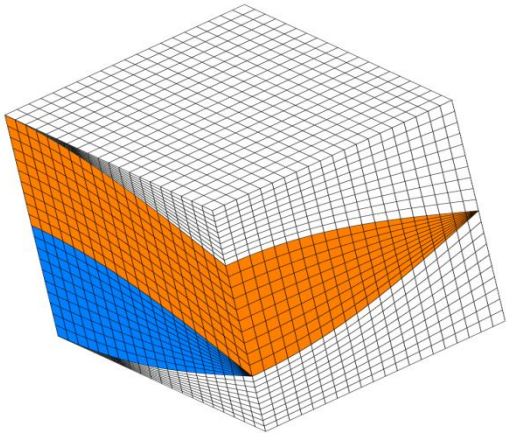

b.) 10 x 7.5 μm mesh

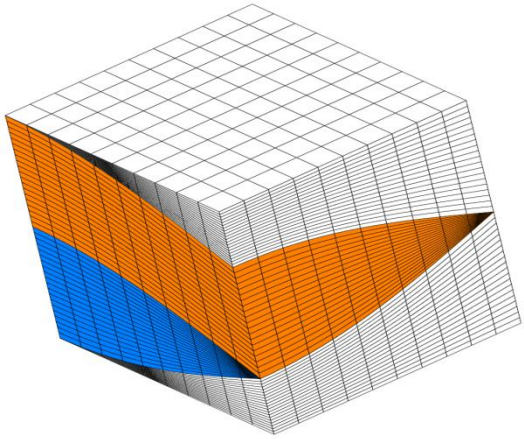

c.) 5 x 15 μm mesh

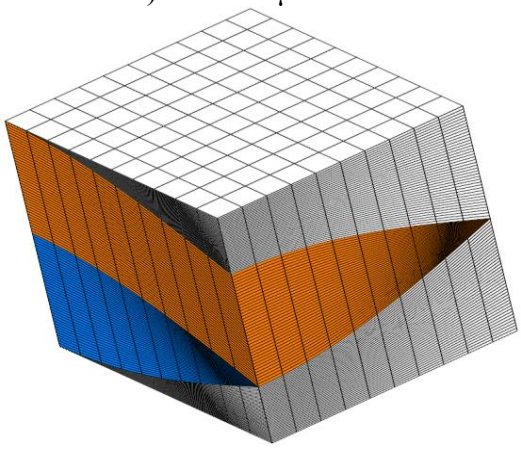

d.) 2.5 x 15 μm mesh

Figure 6.17: Various mesh refinements considered for three-dimensional oxidation analysis of a plain woven composite

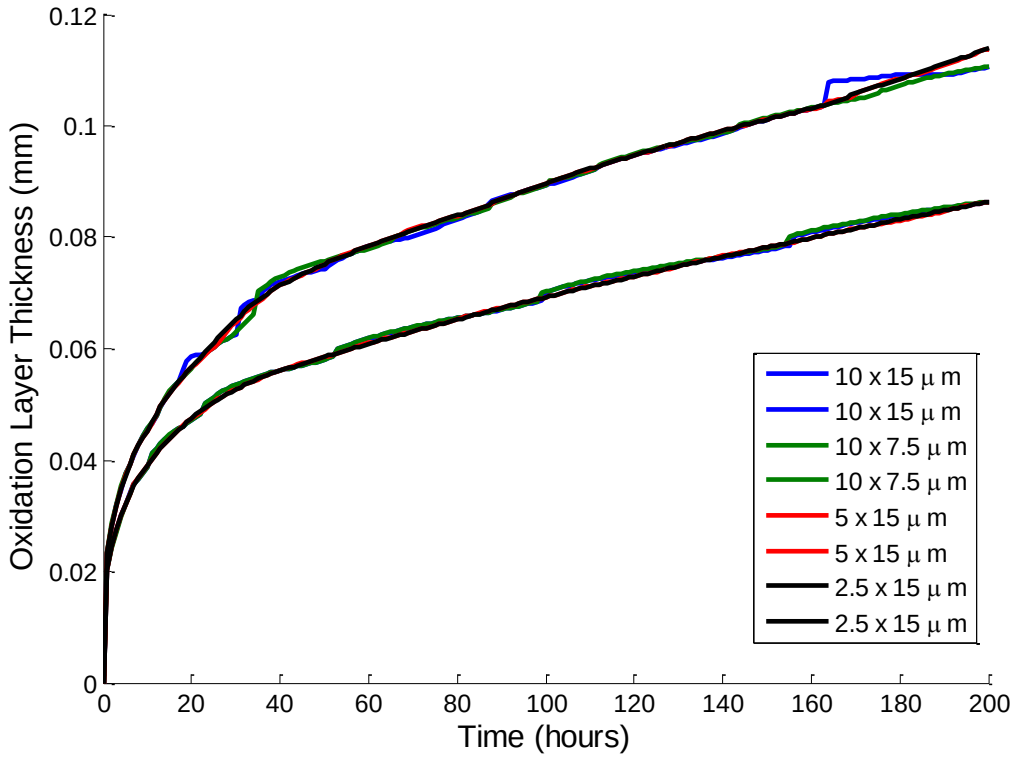

Figure 6.18: Comparison of oxidation envelopes for a plain weave laminate up to 200 hours using various mesh refinements

6.5. Adaptive time stepping

The adaptive time stepping algorithm was validated by comparing results from an oxidation analysis using adaptive time stepping to one that used manual time stepping. Figure 6.19 shows the comparison of concentration profiles at 10, 100, and 200 hours for a one-dimensional oxidation analysis of PMR-15. The solid line shows the result obtained using adaptive time stepping whereas the dashed line shows the result from manual time stepping. The adaptive time stepping results used a minimum time step value of 10^{-6} minutes and a adaptive time step tolerance of 10^{-3}. The manual time stepping results used a uniform time step size of 0.15 minutes. While the manual time stepping required 80000 time steps to complete, the adaptive time stepping algorithm completed the analysis with only 17,400 time steps.

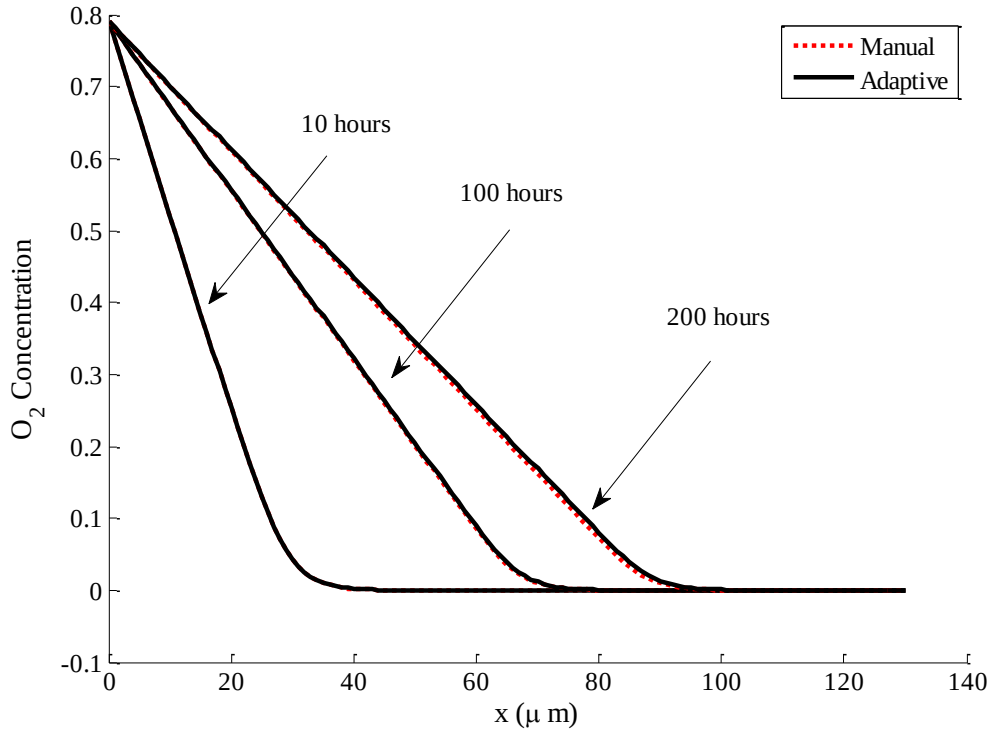

Figure 6.19 Validation of adaptive time stepping algorithm.

6.6. Summary

Various strategies were developed with the goal of expediting oxidation analysis. In particular, the oxidation analysis of textile composites. The complex architecture of textiles coupled with element size constraints for oxidation analysis can result in highly refined meshes. Studies and validation were conducted to determine an optimal element size and time step size for the oxidation of PMR-15. Furthermore, an adaptive meshing strategy was validated which allowed for an increase in efficiency by only periodically solving the entire system of equations in oxidation analysis. A decoupled subdomain strategy developed to expedite composite analysis was validated using two-dimensional and three-dimensional models. Despite the significant simplifying assumptions, the decoupled subdomain strategy predicts the results of a three-dimensional analysis very well. The use of exact and approximate boundary conditions were also examined for three-dimensional oxidation analysis of a plain weave. It appears that approximate boundary conditions give sufficiency accuracy and can significantly reduce the size the mesh used in oxidation analysis. Finally, an adaptive time stepping algorithm was implemented and validated, which showed very good agreement with results obtained by manual specification of an optimal time step.

7. Homogenized Oxidation Properties

When simulating oxidation in a configuration made of composites, it is not practical to discretely model all the matrix and fibers in the composite because of modeling and computational challenges. The same situation is true in the case of textile composites. Similar to what is done in order to perform structural analysis of textile composites, homogenized properties are used to avoid modeling a microstructural scale thereby making the analysis tractable. The necessity is even more severe when simulating oxidation because the finite element formulation requires very refined meshes. Therefore, even discretely modeling the tow architecture scale in a single unit cell creates a very large model. Strategies for determining homogenized oxidation properties for unidirectional laminates or tows are described in Section 3. In this section, the homogenization strategies are validated using various configurations so that they can be reliably used later to model oxidation in textile composites. The next section describes the material properties and the configurations analyzed. This is followed by the results of the analyses and a discussion of the accuracy of the homogenized properties.

7.1. Material properties and configurations

Three configurations were analyzed to determine the accuracy of the homogenized oxidation properties. The expressions described in Section 3 were used to determine homogenized oxidation properties for tows with a fiber fraction of 28.49% and 50%. Table 5.1 specifies the material properties for the neat PMR-15 resin and Table 7.1 specifies those computed for the homogenized tows.

For a more accurate calculation of the diffusivity at V_f=50%, the actual value of $\bar{D}$ in Figure 3.4 obtained from micromechanics (which is 0.3254) is used rather than calculating the value using the formula for the curve fit (which is 0.33). Mesh refinement and time step sizes were determined such that the analyses were computationally efficient while giving accurate results as described in the previous section. The three configurations that were considered are described next.

Table 7.1: Oxidation material properties for the homogenized tows

	Homogenized tow (Vf=28.49%)	Homogenized tow (Vf=50%)
Diffusivity D_{unox} D_{ox}	 41.71 x10^{-6} mm^2/min 60.87 x10^{-6} mm^2/min	 34.88 x10^{-6} mm^2/min 50.90 x10^{-6} mm^2/min
R_0	2.50 mol/(m^{3}min)	1.75 mol/(m^{3}min)
ϕ_{ox}	0.4186	0.5935
C^{∞}	0.564 mol/m^3	0.395 mol/m^3
α	0.01-0.0067(t/40) : t < 40 0.0033 : t > 40 (t in hours)	
$f(C)$	$\frac{2\beta C}{1+\beta C}\left[1-\frac{\beta C}{2(1+\beta C)}\right]$	
β	0.919	

7.1.1. Configuration A (20 fiber)

This configuration is a unidirectional laminate idealized as having fibers arranged in a "square array" with twenty fibers in the x direction and infinite dimensions in the y and z directions. This is illustrated in Figure 7.1 showing a single layer of fibers from an infinite stack of such layers. Although the sketch shows a finite z dimension, the configuration is actually infinite in the z direction. The fibers are identical and have a diameter of 10 microns. The fiber volume fraction of the laminate is 50%. The laminate is exposed to air on both the left and right surfaces. Therefore, the composite begins oxidizing from the outer surface with the oxygen making its way into the interior of the laminate. By taking into consideration the symmetries, this configuration can be analyzed by modeling just ten fibers in a two-dimensional model as shown in Figure 7.1. The analysis region is also shaded in the sketch of the configuration. The left edge of the model is exposed to air whereas the right edge is impermeable. The ten fibers in the matrix are modeled discretely and the results from using this model will provide the reference solution. The fibers are modeled as voids since the fibers are assumed to be impermeable. The same configuration is analyzed in two other ways to test the accuracy of the effective properties. One is to model the configuration completely using homogenized properties for the microstructure. Since this involves only one homogenized material in a simple one dimensional geometry, this can be analyzed using a 1D finite element model. The other way is to use a mixed model with three unit cells on the extremes modeled discretely and the four interior unit cells modeled using homogenized properties. Figure 7.2 shows a schematic of this model. This method will test the accuracy of the homogenized properties in models with heterogeneous materials.

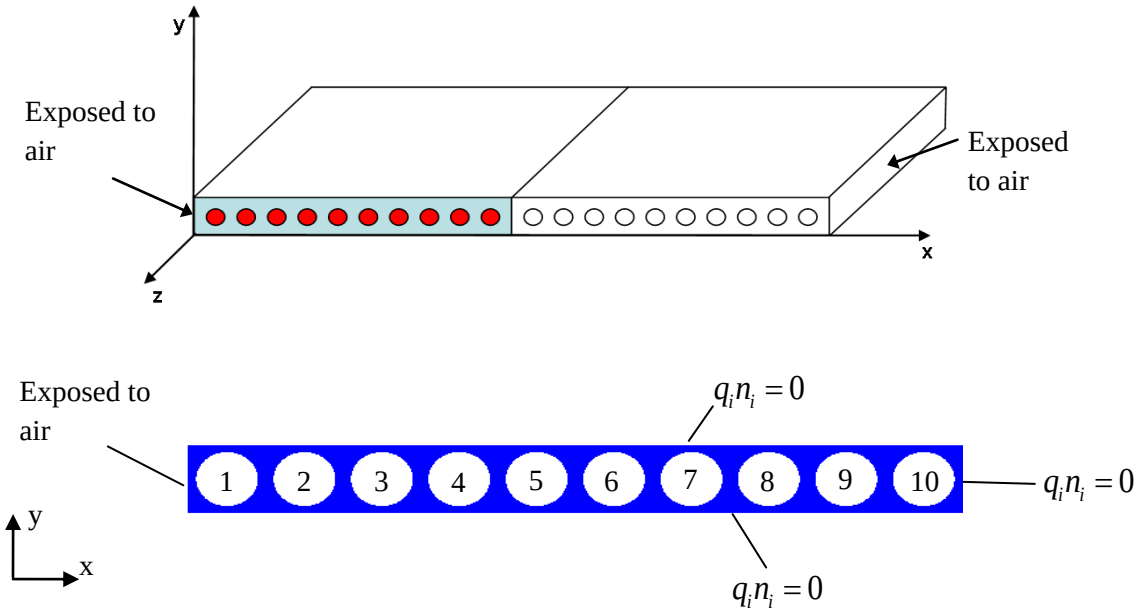

Figure 7.1: Schematic and analysis region for configuration A with the numbering for each unit cell.

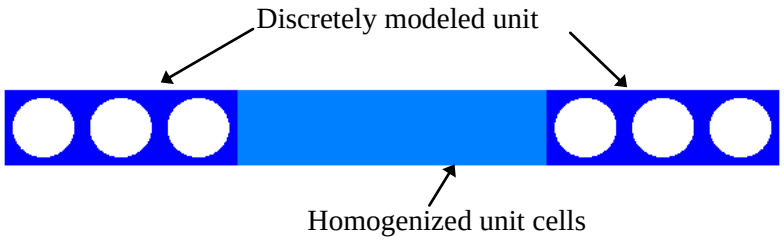

Figure 7.2: Mixed model for configuration A

7.1.2. Configuration B((36 fiber)

This configuration is slightly more complex than the previous one in that the laminate is infinite only in the z direction. This can be considered as a square tow with 36 fibers packed in a square array as illustrated in Figure 7.3. Again, all the fibers have a diameter of 10 microns and are packed with a fiber fraction of 50%. The tow is exposed to air on all four lateral surfaces and starts oxidizing as the oxygen makes diffuses into the tow. Utilizing symmetry conditions, only the shaded region in the sketch needs to be modeled, as shown in Figure 7.3. The left and bottom edges in the analysis model are exposed to air while the right and top edges are specified to be impermeable.

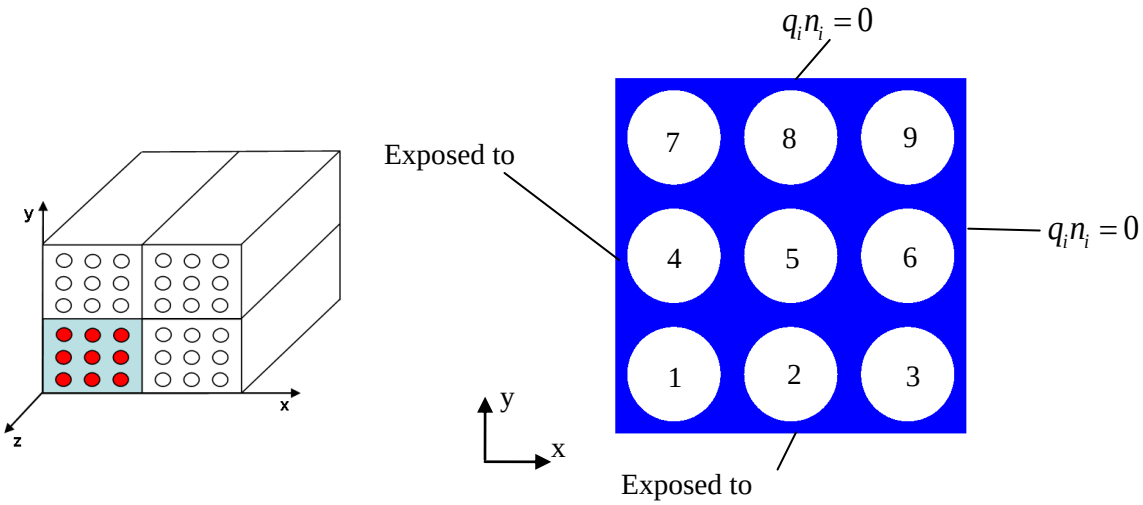

Figure 7.3: Schematic and analysis region for configuration B with the numbering for each unit cell.

7.1.3. Configuration C (irregular fiber distribution)

This configuration considers a slightly more realistic situation with an irregular distribution of fibers. A computer generated random microstructure was used to represent the microstructure in a tow (see Figure 7.4). The two dimensional microstructure assumes that the fibers run exactly parallel to each other in the z-direction. This, of course, is not what happens in a typical tow but this configuration would be a reasonable precursor to modeling the much more complex (if at all achievable) realistic microstructure of a tow. The configuration C has 160 identical fibers with 10 micron diameter like the previous configurations but with an overall fiber fraction of 28.49%. The analysis region is assumed to be a square with a side of 210 microns. The configuration is assumed to be exposed to air from the bottom edge and all the other surfaces are impermeable. Three idealizations are used to model the configuration. The first one discretely models the random microstructure shown in Figure 7.4. This idealization also brings to light the computational challenges involved in analyzing the oxidization behavior of complex microstructures.

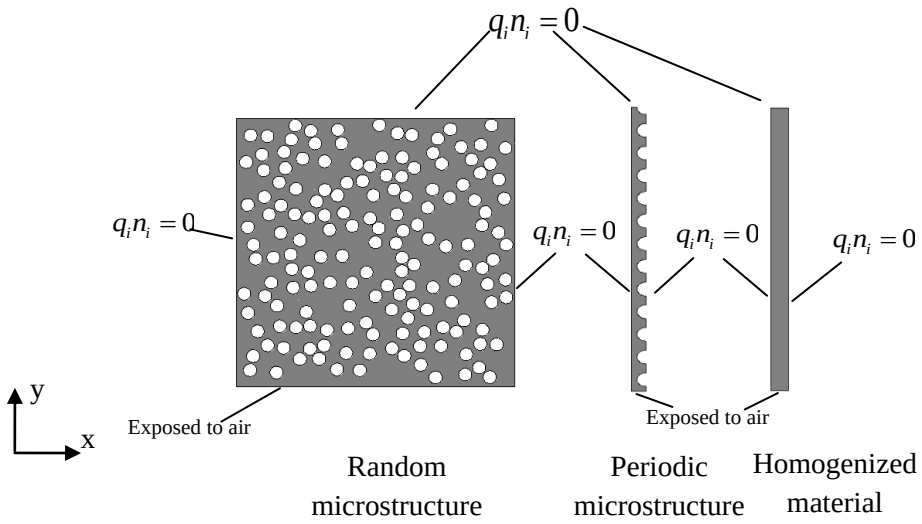

Figure 7.4: Analysis regions for the different configuration C idealizations.

The second idealization uses a periodic microstructure. It is not possible to create a perfect square region using an array of 160 square unit cells because $\sqrt{160}$ is not a rational number. A close approximation was chosen using a square with a side measuring 12.5 square unit cells (or 207.54 microns). Although the height of the periodic model is a half unit cell longer than the discrete model, this difference does not have any effect on the oxidation growth behavior for the 200 hour simulations that are analyzed in this work. Even after 200 hours of oxidation, the oxidation front in a pure resin advances less than 100 microns and the un-oxidized material on the other side of the front has insignificant influence on the oxidation growth up to that point. For a periodic idealization, it is possible to analyze just a fraction of the configuration by taking advantage of symmetry. To analyze the idealized periodic configuration, a model with a width of a half unit cell and a height of 12.5 unit cells was chosen. The third idealization uses a homogenized material to model the configuration. The simple boundary conditions and the single homogenized material in the idealization allow the third configuration to be modeled using 1D elements.

7.2. Results and discussion

Before determining the accuracy of the effective oxidation material properties, diffusion analyses were run for both configurations A and B to validate the accuracy of the effective diffusivities. Oxidation analyses were conducted for all three configurations (A, B and C). The results from the diffusion modeling are discussed first followed by that of the oxidation modeling.

7.2.1. Diffusion modeling

The diffusion behavior was simulated using the un-oxidized PMR-15 resin diffusivity to model the material in the discrete models, which is 53.6×10^{-6} mm^2/min. For the models that used homogenized materials, the corresponding effective diffusivity of the un-oxidized resin was used, which for the case of a 50% fiber fraction tow is 34.88×10^{-6} mm^2/min.

Diffusion analyses were conducted on all three models representing configuration A: discrete model which serves as the reference solution, a fully homogeneous model and a mixed model as shown in Figures 7.1 and 7.2. The two-dimensional models that generated the results shown in Figures 7.5, 7.6 and 7.7 used meshes with a maximum element length of 1.41×10^{-3}mm and a time step size of 0.15 minutes. Figure 7.5 shows the concentration profiles in the discrete and mixed model at 5 hrs. It is seen that the concentration profiles are almost exactly the same in the first three unit cells on the left which is modeled discretely in both the discrete and mixed models. This shows that the effective properties in the homogenized region did not cause an adverse effect on the concentration profile in the discretely modeled region. The homogenized material has a different saturation concentration compared to the neat PMR-15 material as shown in Table 7.1. The normalized concentration distribution will be continuous throughout the model based on the finite element formulation as explained in Section 3. On the other hand, since the homogenized material has a different saturation concentration as compared to the neat resin, the concentration distribution will have a discontinuity at the interface between the discrete and homogenized region. It is not convenient to make reasonable comparison between the two models by just looking at the concentration profiles. When the models compared have homogenized properties, it is perhaps more reasonable to compare volume averaged concentrations.

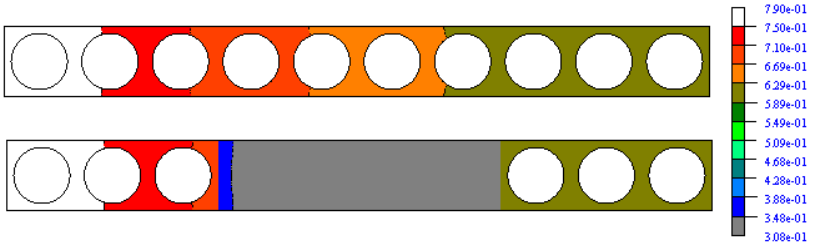

Figure 7.5: Concentration profiles in discrete and mixed models for configuration A under diffusion at 5 hours.

Figure 7.6 shows the volume averaged concentration for the entire model as it grows over time. It shows that the curves from the homogeneous and mixed model fall exactly on top on the curve from the discrete model. To take a closer look at the results, the concentrations were averaged over each of the 10 unit cells in the configuration. The unit cells are numbered as shown in Figure 7.1. Figure 7.7 shows the average concentrations

in each unit cell at three snapshots in the simulation: 15 mins, 150 mins and 375 mins into the simulation. For each snapshot, the average concentrations from the three different models are shown. The first three columns for each unit cell denote the average concentrations for t=15 mins, the next three for t=150 mins and the last three columns for t=375 mins. For each set of three columns, the first one denotes the discrete model, the second denotes the homogeneous model and the last one denotes the mixed model. The results show that both the models that use effective properties agree very well with the discrete model.

Configuration B was analyzed for diffusion using both the discrete model and the fully homogenized model. The two-dimensional models that generated the results shown in Figures 7.8 and 7.9 used meshes with a maximum element length of 1.41×10^{-3}mm and a time step size of 0.15 minutes. Figure 7.8 shows the average concentration in the entire model as it grows over time. The two models agree closely. The homogeneous model under predicts the average concentration in the beginning of the simulation and the difference reduces as time progresses. It is not surprising that the error reduces as the simulation progresses because both models are approaching the same steady state condition. Similar to the previous configuration, the average concentration was determined for each of the nine unit cells at two different times through the simulation. The unit cells are numbered as shown in Figure 7.3. Figure 7.9 shows the average concentration from the discrete and homogeneous in each unit cell at t=1.5 and 15 minutes. The results in Figure 7.9 repeat the trend from Figure 7.8 in that the homogeneous model under predicts the concentrations and the predictions become closer in agreement as the simulation progresses. In this configuration, the concentration profile is more complicated than the earlier one because the oxygen is flowing in from two directions. This kind of complex loading appears to have an effect on how well the diffusion is modeled by the effective properties. Although it does not do a perfect job in simulating the oxygen flow in the beginning, the accuracy increases very quickly as the simulation progresses.

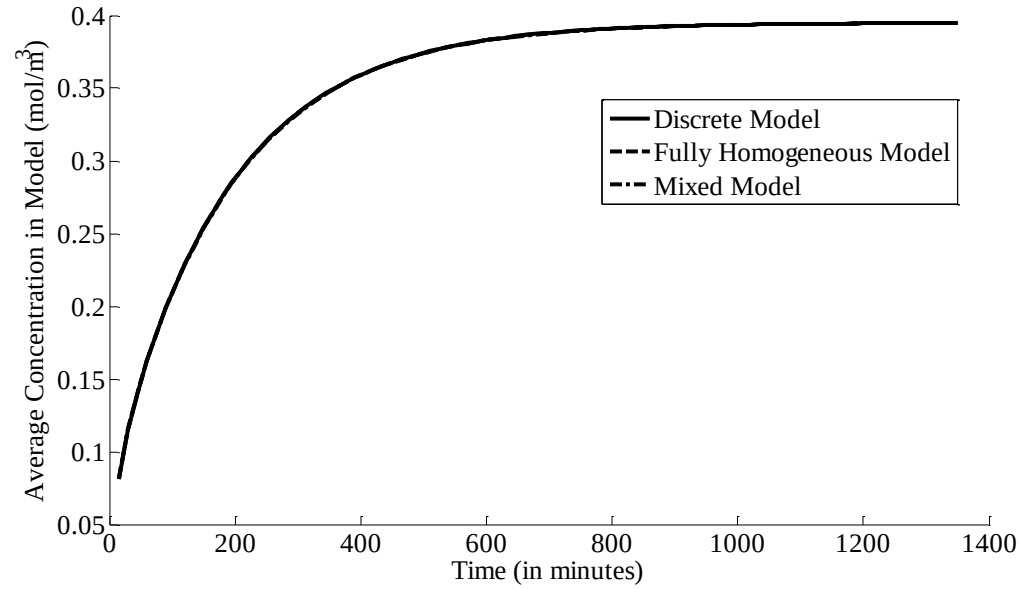

Figure 7.6: Variation of average concentration in configuration A with time

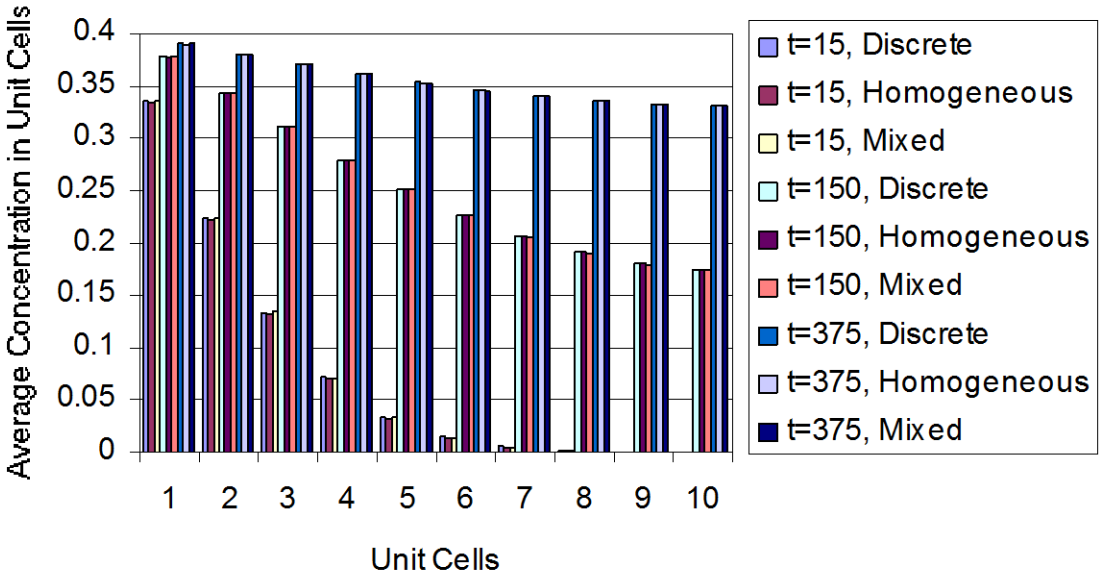

Figure 7.7: Variation of average concentration in each unit cell in configuration A at different times (in minutes)

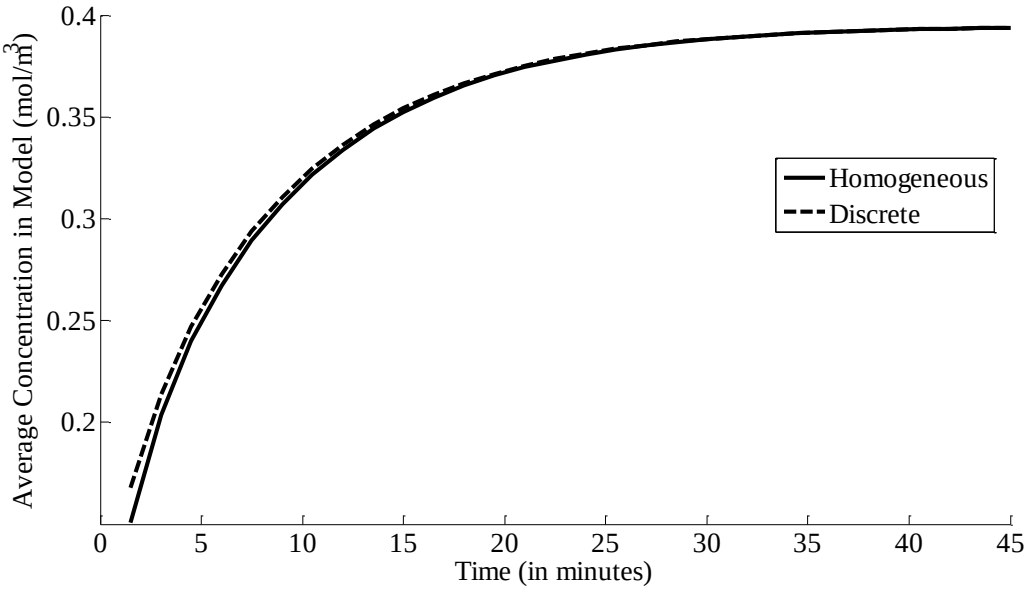

Figure 7.8: Variation of average concentration in configuration B with time

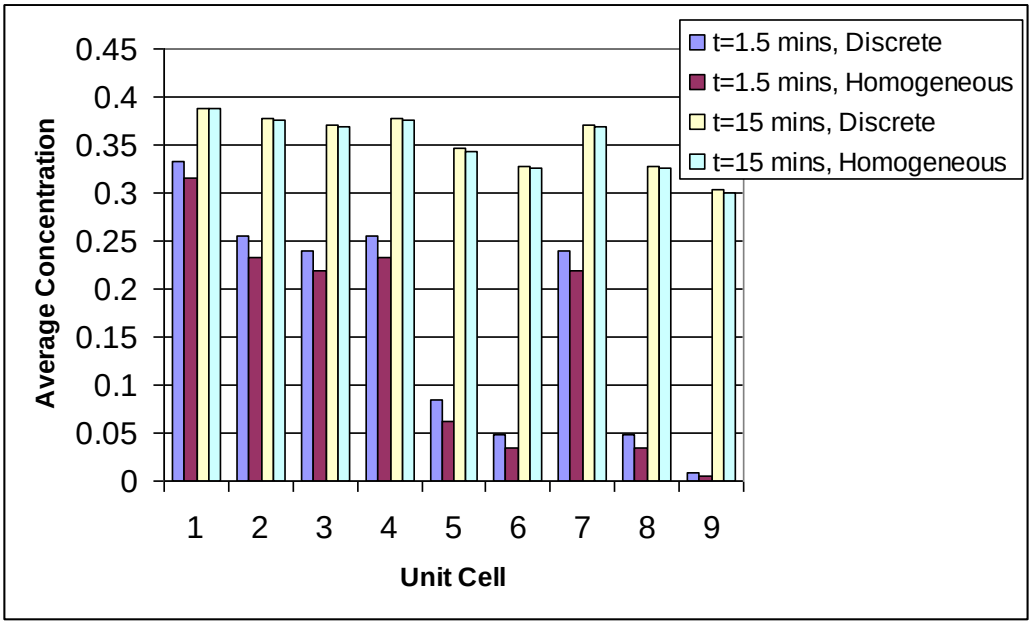

Figure 7.9: Variation of average concentration in each unit cell in configuration B at different times (in minutes)

7.2.2. Oxidation modeling

This section discusses the results from the oxidation simulation of configurations A, B and C. In the oxidation analysis, there are primarily two types of data that are of interest – the concentration and the oxidation state. For configuration A and B, the concentration distribution will be discussed first followed by the oxidation state. For configuration C, only the oxidation state results are presented.

Figure 7.10 shows the concentration profiles in the discrete and mixed model at 200 hrs. It is seen that the concentration profiles are almost exactly the same in the first three unit cells on the left which are modeled discretely in both the discrete and mixed models. This shows that the effective properties in the homogenized region did not cause an adverse effect on the concentration profile in the discretely modeled region. There is, as expected, a discontinuity in the concentration at the interface between the discrete and homogenized region just as seen in the diffusion analysis of configuration A.

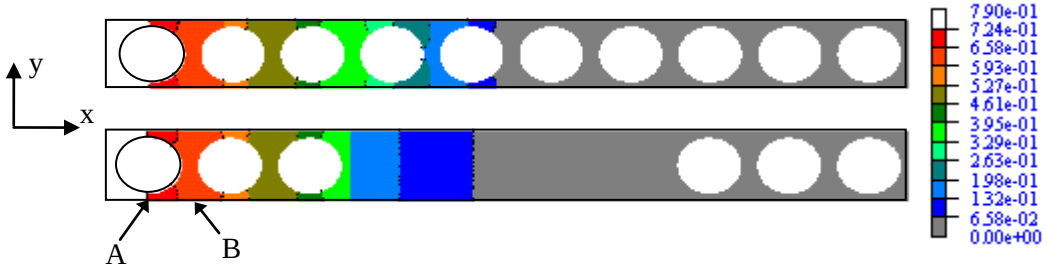

Figure 7.10: Concentration profiles in discrete and mixed models for configuration A at 200 hours.

Just as the results for the diffusion analysis were presented, Figure 7.11 shows the average concentration growth in the model over time. The plot shows that the discrete model appears to have spurts of increase in the average concentration. This can be explained by the fact that the discrete model has fibers that are impermeable and do not oxidize. When the oxygen diffuses from the left end, the cross sectional area of the polymer material through which it can diffuse varies. The area decreases to a minimum where the fiber takes up the most space in the cross section (indicated by A in Figure 7.10) and increases to a maximum when there is no fiber in the cross section (indicated by B). Therefore, when the oxygen is diffusing through the constricted regions, the process slows down and this effect shows up in the concentration growth. When the oxidation front (or the 'moving barrier' as described in the previous section) passes the constricted pathways, the process speeds up for a while till the next constricted pathway comes along. The homogeneous model has no such spurts in the growth of the average concentration because the model assumes that it is all one homogeneous material without any impermeable fibers. On the other hand, the mixed model does show the spurts in concentration growth in the first part of the curve because the mixed model does have three discrete fibers modeled in the left end where the oxygen is entering the

material. Although there are these oscillations when the fibers are discretely modeled, it is clearly seen that the models with the effective properties do follow the same general trend and appears to follow the mean line of the oscillating curves.

Figure 7.12 shows the difference in the average concentration from the discrete and homogeneous in each unit cell at t=150 minutes and t=200 hours. While the homogeneous models always under predicted the average concentrations in the diffusion only analysis (see Figures 7.7 and 7.9), no such correlation was seen in the oxidation analysis. This can be attributed to the same reason for seeing surges in the growth of the average concentration. As seen in Figure 7.11, depending on the simulation time, the homogeneous model fluctuates between under predicting and over predicting the average concentration. This same effect is what is seen in Figure 7.12.

The Zone I and II thicknesses are measured for all the three models for configuration A: the fully discrete model, fully homogenized model and the mixed model. The zone thicknesses for the discrete and mixed models are assumed to be the thicknesses along the top or bottom edges of the model. Note that the model is symmetric about the horizontal mid-axis and therefore the oxidation layer growth will be symmetric about that line. Figure 7.13 shows growth of the oxidation layer (Zone I + II) for the three models as well as the variation of the active zone layer (Zone II). It can be seen that the effective properties do a good job in predicting the growth in both the homogenous and mixed model. The Zone II thickness is also found to be predicted fairly well considering that the Zone II thickness according to the discrete model appears to fluctuate erratically. Figure 7.14 shows the evolution of the oxidation layer in the discrete and mixed models. The three zones, Zone I (Fully oxidized), Zone II (Oxidizing) and Zone III (Un-Oxidized) are color-coded by grey, red and blue respectively. Figure 7.14 shows the state of oxidation at six different times during the simulation, t= 150 mins, 25 hrs, 50 hrs, 100 hrs, 150 hrs and 200 hrs. The snapshots in Figure 7.14 shows what has already been conveyed by Figure 7.13 in that the effective properties are able to simulate the oxidation layer growth fairly well for configuration A.

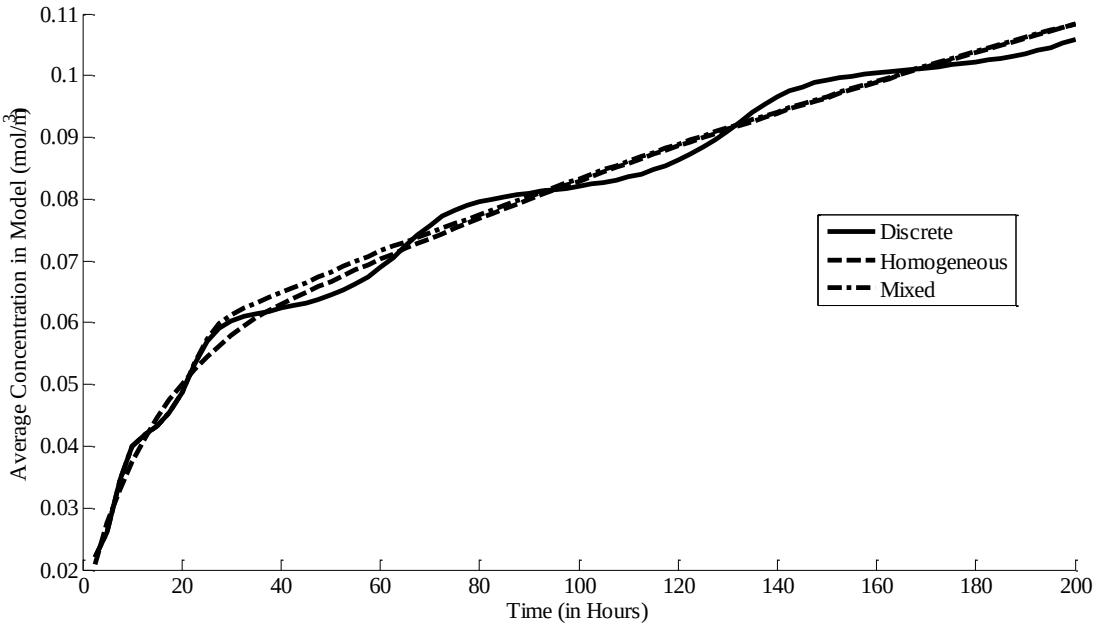

Figure 7.11: Variation of average concentration in configuration A with time under oxidation

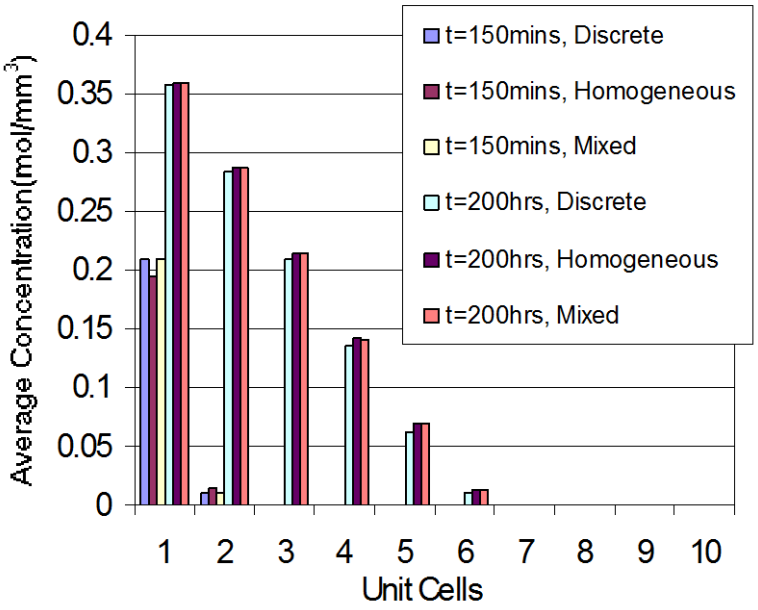

Figure 7.12: Variation of average concentration in each unit cell in configuration A at different times under oxidation.

Next, the oxidation analysis was performed for configuration B using two models – a discrete model and a homogeneous model. Figure 7.15 shows the concentration distribution in the two models at time, t=150 mins. The homogeneous model has the fibers drawn in light gray in order to expedite comparisons with the discrete model. While the concentrations contours do not exactly match, the contours in between the fibers do in some sense resemble corresponding contours in the homogeneous model. Figure 7.16 shows the growth of average concentration in the two models as simulation progresses. Similar to the concentration growth in discrete model for configuration A, it can be seen that the concentration growth for configuration B follows a similar oscillating trend. The plot shows that the homogeneous model under-predicts the average concentration for most of the simulation. It is understandable that the homogeneous model is not able to reproduce the wavy nature of the concentration growth in Figure 7.16 because that effect is caused by the microstructure. The homogenous model on the other hand, does not have such a microstructure.

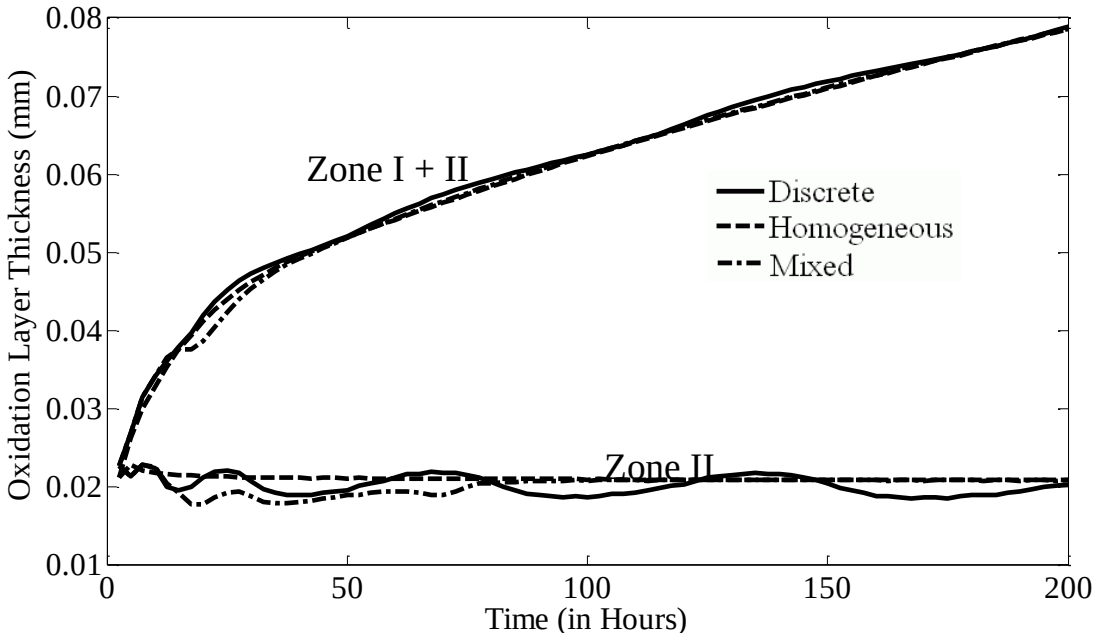

Figure 7.13: Oxidation layer growth (Zone I+II and Zone I) for configuration A

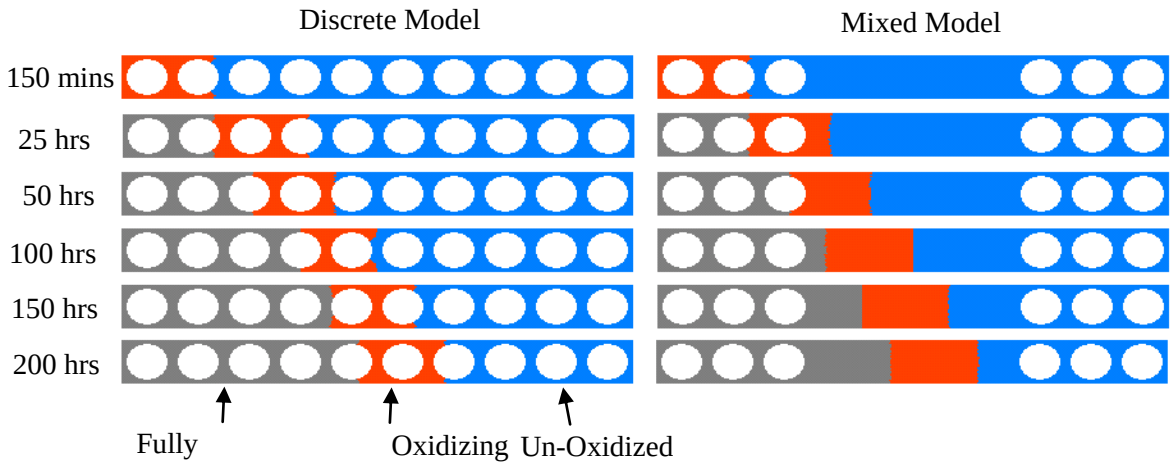

Figure 7.14: Evolution of oxidation layer in discrete and mixed model for configuration A

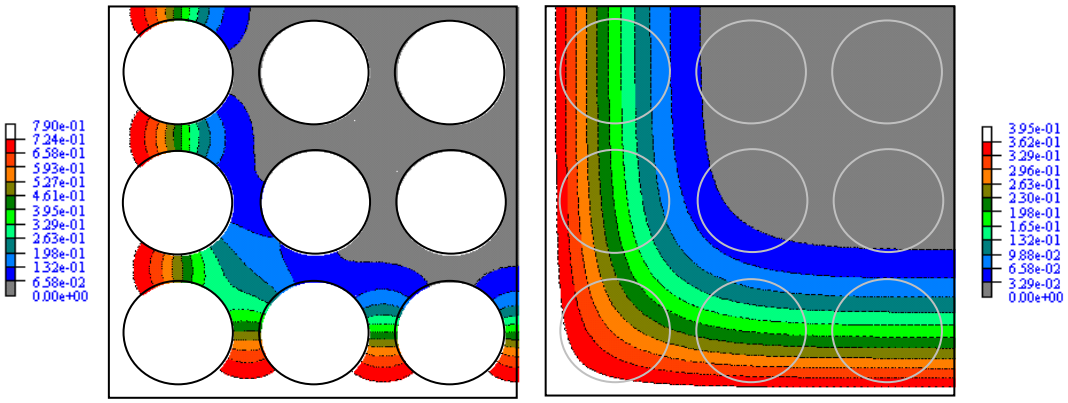

Figure 7.15: Concentration profiles in discrete and mixed model at t=150 mins for configuration A

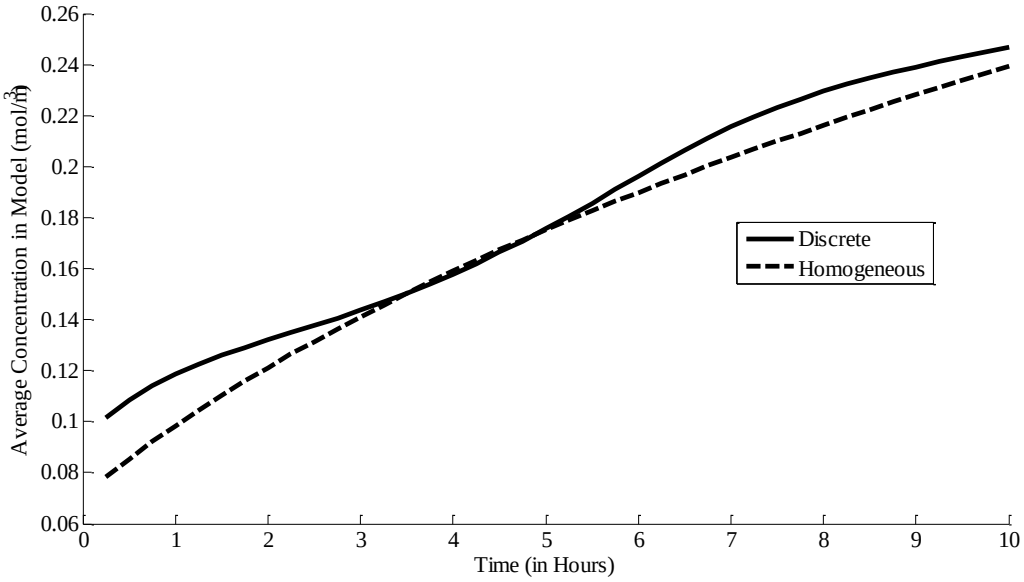

Figure 7.16: Variation of average concentration in configuration B with time under oxidation

The oxidation state from the two models is compared next. Figure 7.17 shows the oxidation state at different times in the simulation. As shown in Figure 7.15, the homogeneous model has the fibers drawn in light gray in order to expedite comparisons with the discrete model. The oxidation states for t=15 mins, 2.5 hrs, 5 hrs and 10 hrs are shown. The figures show that the homogeneous model is able to predict the oxidation layer growth fairly accurately.

The discrete models that have been considered so far model only 9 or 10 fibers but the discrete model for configuration C models 160 fibers. This makes it a considerably larger model and more time-consuming compared to the previous models. Figure 7.18 shows the contour plots of the oxidation state in the discrete and periodic models after undergoing 75 hours of oxidation. As expected the oxidation profile is irregular for the model with the discrete microstructure. Nevertheless, the variation in thickness and location of the oxidation layer from the exposed edge varies no more than 5% across the width. It is interesting to note that the periodic model predicts relatively the same amount of oxidation growth as the random model which indicates that for this fiber volume fraction and distribution of fibers, the oxidation growth can be idealized by using a periodic array. While Figure 7.18 shows the oxidation state distribution at a single snapshot from the entire simulation, Figure 7.19 gives a sense of how the oxidation state evolved during the entire simulation. Figure 7.19 gives the oxidation layer growth over time for the random, periodic and homogenized idealizations. It shows the oxidation layer growth along the two edges (right and left) of the discrete model.

While the two curves do not fall right on top of each other, they are very close. The curve from the periodic model is very close to the curves from the discrete model and follows the same trend but slightly under predicts the oxidation growth. The homogeneous model also follows the same trend but under predicts the growth even further. To make an easy comparison with the behavior if there were no fibers at all (i.e. pure resin), the oxidation growth curve from pure resin oxidation analysis (using a 1D model) is also included. This shows that the pure resin oxidizes slightly faster than when there are fibers in the resin which is expected since the fibers are assumed to be impermeable and do not oxidize.

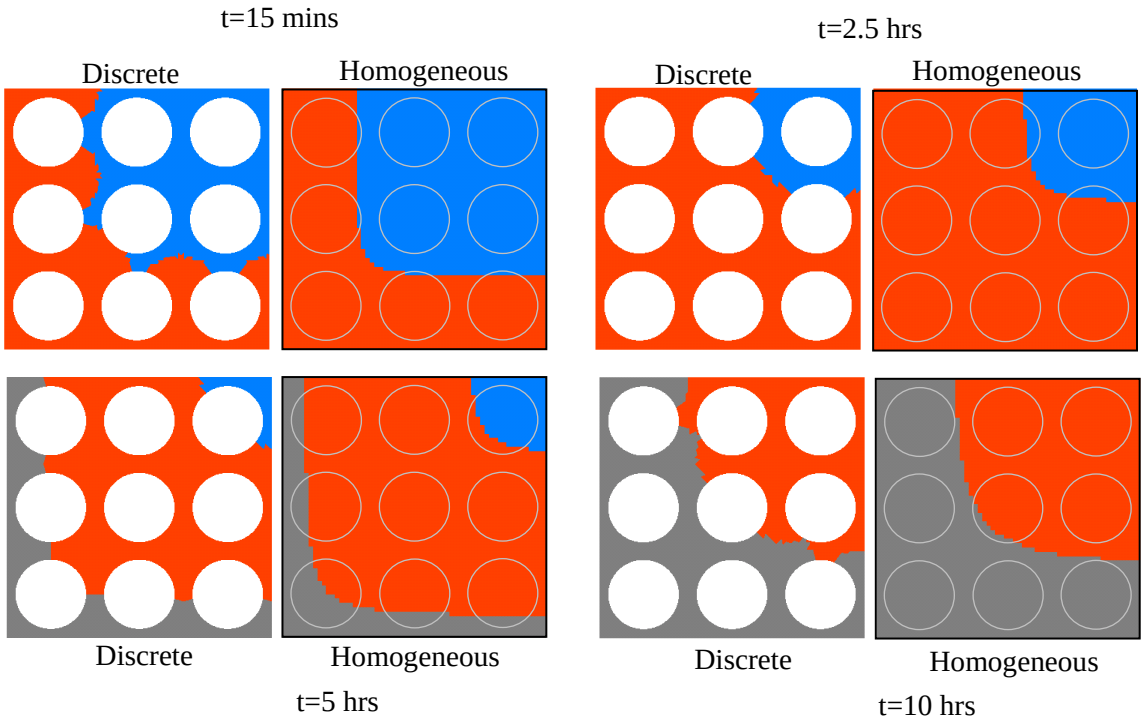

Figure 7.17: Evolution of oxidation layer in discrete and homogeneous models for configuration B

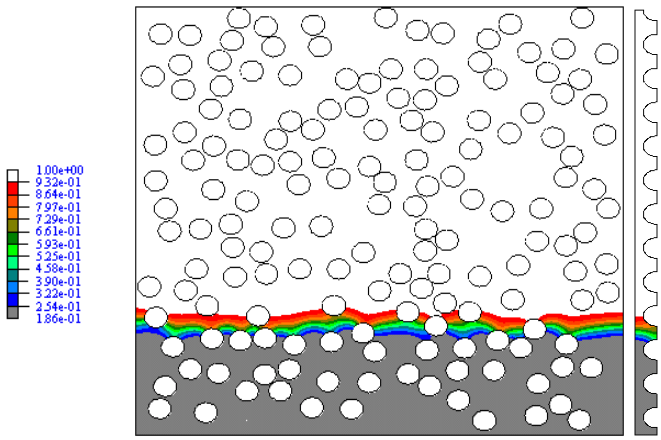

Figure 7.18: Oxidation state profiles in discrete and periodic model at t=75 hours for configuration C

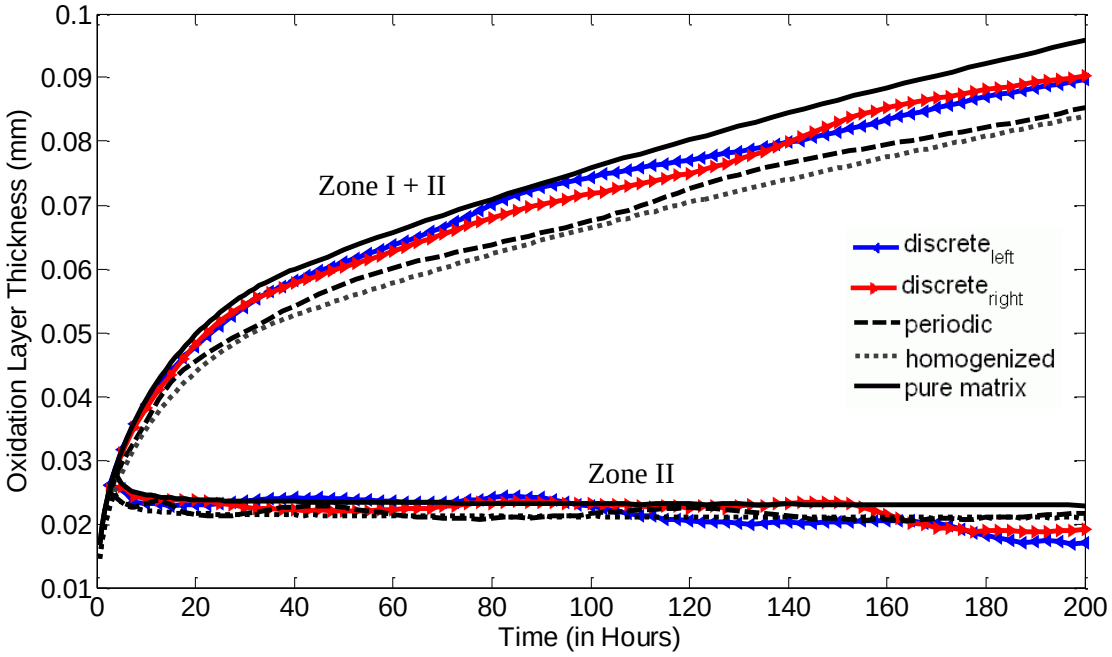

Figure 7.19: Oxidation layer growth (Zone I+II and Zone I) for configuration C

A typical homogenization process in structural mechanics results in being able to use a less refined homogenized model to replace the actual microstructure. This was generally found to be the case for the oxidation analysis as well. As discussed in the previous section, it is possible optimize the mesh parameters and use larger elements and time steps. In some configurations, including the ones described in this section, the element size is restricted by the need model the discrete geometry accurately. This restriction is greatly reduced when modeling homogenized regions. It is also easier to generate the models when a complex microstructure can be replaced by a simpler homogenized geometry. Another advantage is that sometimes a two dimensional model can be replaced with a one dimensional model that is much less computationally intensive. This was made use of when analyzing configuration A with a fully homogeneous model. The goal of this work is to eventually be able to correlate the effect of the oxidation on the mechanical response and damage progression of the composite. Keeping this in mind, tracking the regions of oxidized or oxidizing material in the composite is what would be considered to impact the mechanical response. For the material system being considered in this work, the thickness of the active zone is found to be practically constant and the variation of oxidation state within this zone can be inconsequential in this regard, but this need not be the case for other composite systems. Further work needs to be performed in order to determine if some accuracy of the oxidation state variation in the active zone can be given up in exchange for better computational efficiency as long as the oxidation layer thicknesses are predicted with reasonable accuracy.

7.3. Summary

To simulate the oxidation of the textile composite, it is important to be able to use homogenized oxidation properties for the tow because it is practically impossible to discretely model all the fibers in a composite. Effective oxidation material properties were calculated for a unidirectional laminate/tow using the expressions described in Section 3. Three configurations were analyzed to test the accuracy of the effective oxidation properties. The fibers were assumed to be impermeable and do not oxidize. All the configurations had 10 micron diameter circular fibers. Two of the configurations had the fibers in a square array packing with 50% fiber fraction whereas the third configuration had random microstructure with an overall fiber fraction of 28.5%. The configurations were discretely modeled to provide a reference solution. Idealizations with fully homogenized materials as well as mixed idealizations (both discrete and homogenized regions) were used to determine the accuracy of the effective properties. The concentration of oxygen in the model as well as the oxidation state of the materials in the composite was compared to the reference model. It was seen that the effective oxidation properties performed reasonably well for both configurations and were able to simulate the oxidation layer growth.

8. Oxidation Analysis of Textile Composites

One of the primary goals of this work is to study the effect of oxidation on damage progression in textile composites. A precursor to the complete damage progression is the oxidation analysis of the textile composite. The information from the oxidation analysis will be used to degrade the mechanical properties of the textile composite in the damage progression model. In this work, the mechanical damage is assumed to not have an effect on the oxidation behavior. Therefore, the oxidation model and the damage progression model are only coupled in one direction, where the oxidation behavior has an effect on the damage model and not the other way round. As discussed in the previous sections, simulating the oxidation behavior is a computationally intensive task. At the time the results in this section were obtained, the efficiency of the software did not allow for 3D results to be obtained. These results were obtained using the decoupled subdomain strategy (DSS) described in Section 5 and validated in Section 6. Validation showed that DSS agrees quite well with the 3D results. Thus, the results presented in this section should be viewed as having adequate accuracy despite the simplifications imposed by DSS. This section also describes the information that is generated from DSS, which can then be used in the coupled damage progression model to predict the mechanical behavior of the composite under oxidation.

8.1. Plain weave analyzed using decoupled subdomain strategy

Now that DSS has been validated in Section 6, it can be used to simulate the oxidation behavior in textile composites and eventually coupled with the damage progression analysis to predict the mechanical behavior under oxidation. The configurations that are examined in this work are plain weave laminates exposed to oxygen at the top and bottom surfaces and the oxidation behavior is simulated only for 200 hours. As discussed later in this section, after 200 hours of oxidation of the laminates with the material system that is considered in this work, the oxidation layer thickness does not exceed more than the thickness of a single ply. Therefore, based on the oxidation model implemented in this work, the growth of the oxidation layer would be the same regardless of whether it is a 2-ply laminate or if it has more than 2 plies. On the other hand, although the oxidation layer growth is the same, the number of plies could have an impact on the mechanical behavior and this is discussed in the next section.

DSS was used to simulate the oxidation behavior in a symmetric two-ply graphite/PMR-15 plain weave laminate. Both the top and bottom surfaces are exposed to oxygen. The composite is chosen to have a waviness ratio of 1/3. A full unit cell of the configuration is shown in Figure 8.1(a). By exploiting symmetry, it is possible to analyze the configuration using only $1/8^{th}$ of the full unit cell as shown in Figure 8.1(b) with a transparent matrix. The decoupled subdomain strategy is used on the reduced domain, which is automatically subdivided into an array of 64 1D models as described in the previous section. Since the effects of the undulation are assumed to be insignificant, both the warp and fill tows have the same oxidation material properties in the through-

thickness direction. This means that the four quadrants in Figure 8.1(b) are essentially identical after the appropriate rotations about the z-axis , and therefore the results from the corresponding 1D models in the different quadrants will be the same. Figure 8.1(c) shows one of the quadrants from Figure 8.1(b) (labeled 1) which is 1/32nd of the full unit cell. The labeling in Figure 8.1(c) shows the unique domains once the decoupled subdomain strategy is applied. Since through thickness properties of the tows are the same when the undulation effect on material orientation is disregarded, a plane of symmetry exists as shown in Figures 8.1(c) and 8.1(d). Figure 8.1(d) provides a view rotated by 180^{o} about the z-axis to verify the available symmetry within the 1/32nd unit cell when employing the decoupled subdomain strategy.

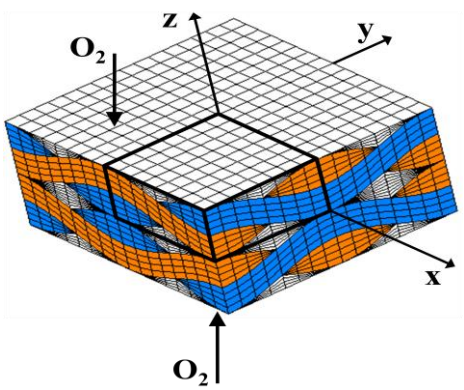

(a) Full unit cell

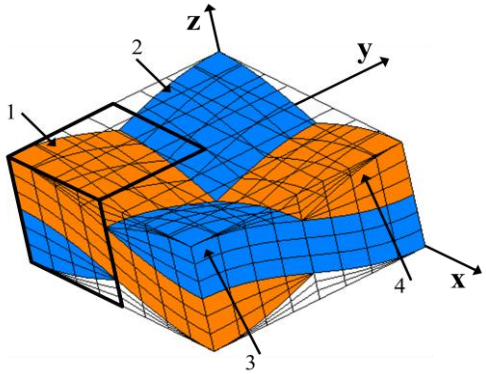

(b) 1/8th unit cell

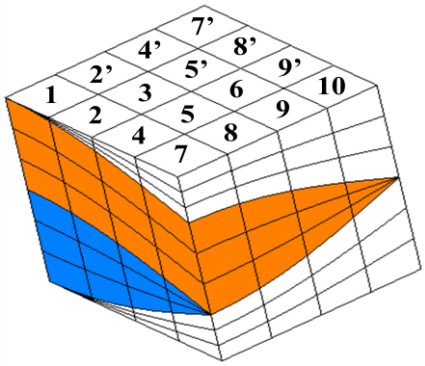

(c)1/32nd unit cell with unique domains labeled

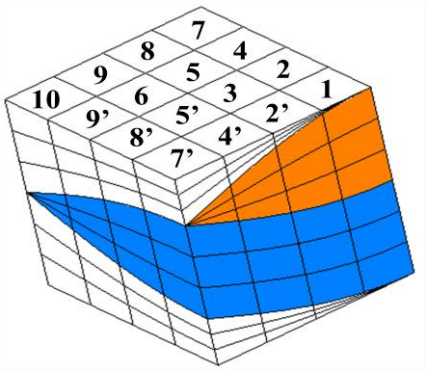

(d) Alternate view of 1/32nd unit cell to display symmetries

Figure 8.1: Configuration and analysis domains for simulating oxidation in plain weave composite

Therefore, the only unique results from the analysis are those from the 10 domains numbered in Figure 8.1(d). Figure 8.2 gives the predicted oxidation layer growth for the 10 domains. It shows that there is considerable variation in the oxidation layer growth behavior of the 10 domains. At the end of 200 hours of oxidation, the thickest layer is 0.11 mm (in Domain 9) which is only slightly larger than half the thickness of a single

ply. Figure 8.1(c) shows that domain 10 has the largest amount of matrix with a very small region of tow in the middle whereas domain 1 has the largest amount of tow with a very small region of matrix at the two ends. Although domain 10 has the largest amount of matrix, it is not the domain that has the thickest oxidation layer. This is because, as discussed earlier, in heterogeneous models the oxidation behavior is not very straightforward and depends on a number of factors such as the location of the material boundaries and the oxidation properties of each of the constituent materials. In each of the ten unique 1-D domains representing the weave microstructure, the material boundaries are at a different distance away from the exposed surface. This results in a varied oxidation behavior from the 1-D models. Since domain 10 is almost all resin with a small region of tow in the middle, its oxidation behavior would be expected to be close to that of a neat resin. Similarly, since domain 1 is almost all tow with small regions of matrix at the two ends, its oxidation behavior would be expected to be close to that of a homogenized tow model.

However, as explained earlier with the heterogeneous configuration, the behavior is not always close to that of the corresponding homogeneous model. Figure 8.3 shows the layer growth for domains 1 and 10 as well as for a neat resin model and a homogenized tow model. It shows that domain 10 follows the same behavior as a neat resin model but once the oxidation front reaches the tow material, domain 10 has a slightly faster oxidation layer growth. For domain 1, the oxidation layer is only slightly thicker than that in an all tow model. Overall, the analysis shows that the oxidation front does not advance uniformly throughout the composite. At the end of 200 hours of oxidation, domain 1 has the smallest oxidation layer with a thickness of 84.5 microns and domain 9 has the largest oxidation layer with a thickness of 110 microns. That is a range of over 25 microns, which is over 30% of the domain 1 layer thickness. Therefore, it can be said that the tow architecture plays a significant role in the variation.

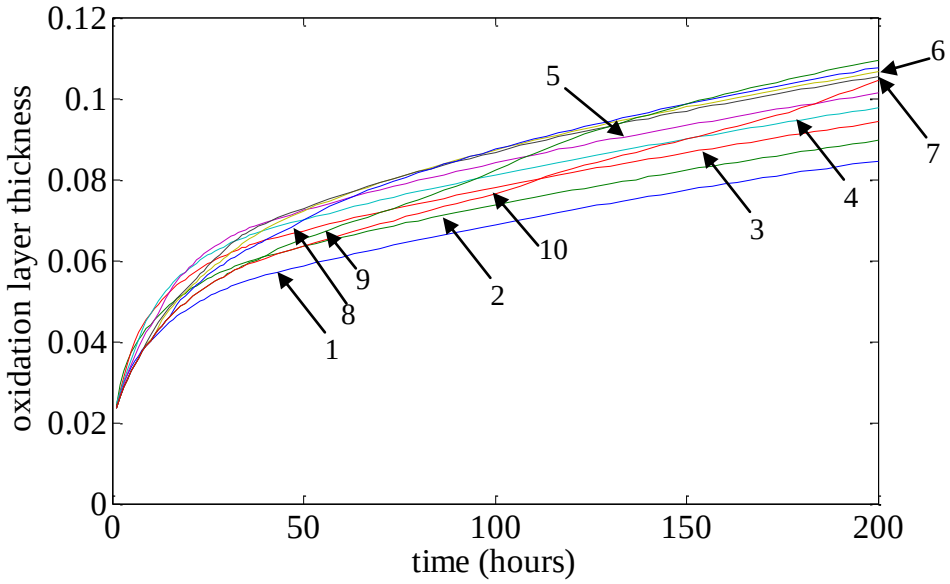

Figure 8.1: Oxidation layer growth in the 10 unique domains

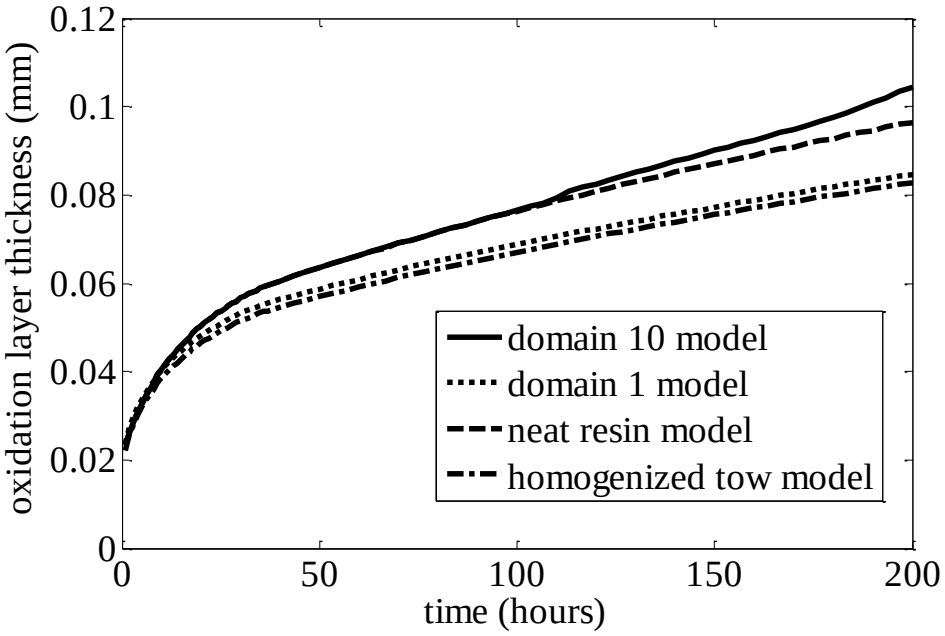

Figure 8.2: Comparison of oxidation layer growth in domains 1 and 10 with that of a neat resin model and homogenized tow model

8.2. Storage of oxidation behavior data from decoupled subdomain strategy

The oxidation behavior of the laminate is eventually used in the coupled damage progression model in order to predict the mechanical behavior under oxidation. In order to do this, the results from the oxidation analysis need to be passed on to the damage progression model. The results consist of the distribution of the oxidation level property in the laminate at different time steps in the simulation. The oxidation level data at the different time steps is needed by the damage progression model in order to degrade the mechanical properties of the composites based on how much of the material has oxidized. The value of the oxidation level at each integration point in the all the elements of the finite element model is kept track of in the memory and can be written to a file, similar to how the stress distribution in a model can be written to a file. If the oxidation model and the damage progression model used the same discretization for the analysis domain, i.e. the same finite element mesh, then the information transfer is straightforward. The oxidation level distribution file can be read in by the damage progression model and all the oxidation level information would be available for performing the mechanical property degradation.

However, when a hybrid model is used for the oxidation analysis, the information transfer to the damage progression model is not so straightforward. In the hybrid model, each individual 1-D domain is an approximation of the actual 3-D region that it represents in the laminate. Due to this reason, the oxidation level value distribution in the 1D model is not an exact representation of what the distribution would be if the actual 3-D domain was analyzed. For example, Figure 8.4 shows a 3D domain and its equivalent 1D domain. Point A in the 3D domain would be the geometrically equivalent point to Point B in the equivalent 1D domain, but note that the two points are located in different material regions of the models. Point A is located in the matrix region where as Point B is located in the tow region. However, because of the characteristic oxidation behavior, the mismatch in the geometry is only an issue when the oxidation front is in the vicinity of the material boundaries. Even when the oxidation front is near the material boundary, it is seen that errors due to this mismatch are not significant because the rotation angles of the tow in the laminates are not large enough.

Another issue has to do with the amount of information that has to be transferred from the oxidation model to the damage progression model. For example, using DSS on the 3D domain shown in Figure 8.1(b) would result in 64 1D domains. Assuming that the oxidation level distribution is post-processed and outputted by each 1D model at 88 different time steps throughout the oxidation simulation, this would result in the creation of 88 x 64 = 5632 data sets. During the coupled simulation, at each of the 88 time steps, 64 different files need to be opened and the oxidation level information of each element in all the 1D models need to be read in. A strategy was sought that could reduce the number of file I/O operations as well as the amount of data that had transferred during the coupled analysis while maintaining reasonable accuracy. The approximations that were made in the developed strategy and a description of the data that is transferred from

the hybrid oxidation model to the damage model are described in the remainder of this section.

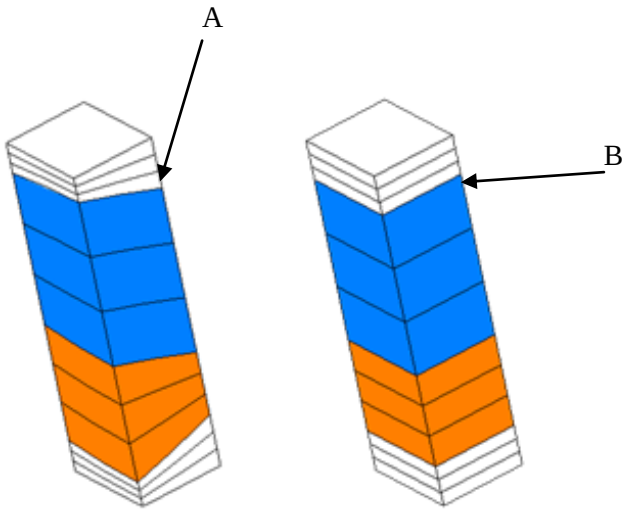

Figure 8.3: 3D domain and equivalent 1D domain in hybrid modeling strategy

Note that the value of the oxidation level at a material point can vary from 1 to 0 as described in Section 3. A value of 1 denotes that the material is un-oxidized and a value of 0 denotes that the material is fully oxidized. Typically, a significant majority of the model is made up of either fully oxidized or un-oxidized material. A small fraction of the model has oxidation levels in the range between 1 and 0, which ideally denotes the active zone, or that the material has started oxidizing but it is not fully oxidized yet as shown in Figure 3.5. Therefore, instead of storing the oxidation level information for each element in the 1-D model, just the dimensions of the active zone is stored to represent the oxidation level profile for a particular time step. In this manner, the oxidation level profile in a 1D domain for all of the 88 time steps can be effectively compressed into a single file using only a fraction of the information. When the data is read in during the coupled simulation, the oxidation level profile is approximated using a linear variation of the oxidation level within the active zone. These approximations are made based on a few assumptions. The active zone is assumed to be very small compared to the fully oxidized and un-oxidized region. Although the actual variation of the oxidation level in the active zone is not linear, the linear variation assumed in this model is assumed to be reliable for the material systems considered in this work. The simple linear approximations employed here are assumed to be reliable for the purposes of predicting mechanical behavior in the composites. Figure 8.5 shows the predicted oxidation level profile in a block of neat resin at 100 hours. The dotted line shows the approximated oxidation level profile. The location where the approximated oxidation

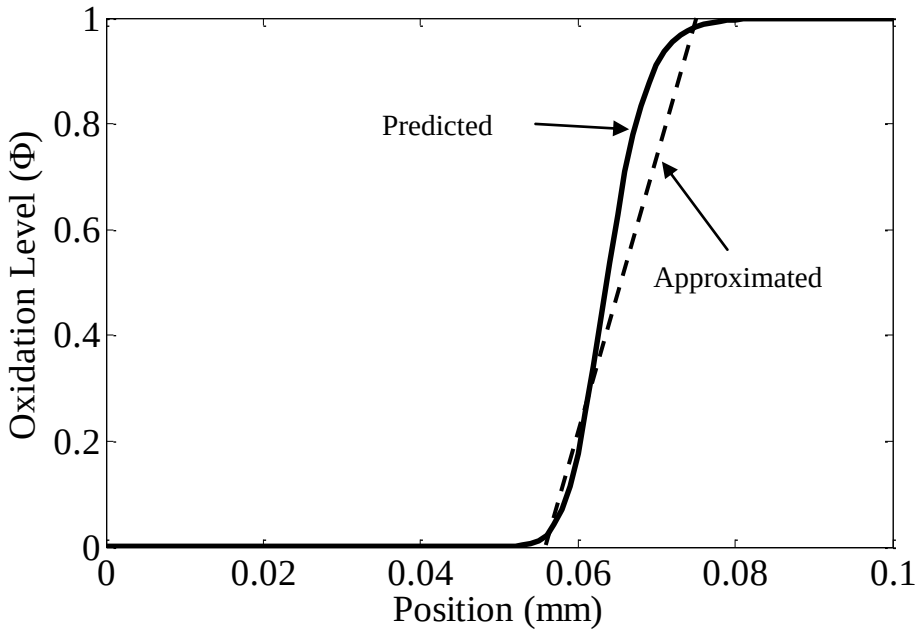

Figure 8.4: Oxidation Level profile in neat resin 1-D model at 100 hours

level starts lowering from 1.0 is determined by the thickness of the oxidation layer or in other words the dimensions of the oxidation zones. The instructions to determine the dimensions of the different zones and the oxidation layer thickness are described in Section 3. The location of the point where the approximated oxidation level reaches 0 is also similarly determined by the dimensions of the active zone (typically it is the location where the predicted oxidation level reaches 0.01). During the initial stages of oxidation when there is no fully oxidized material, the predicted oxidation level does not drop all the way to 0. In this case, the linear approximation is based on the value of the predicted oxidation level at the location in the model that is exposed to oxygen. This is illustrated in Figure 8.6, which shows the oxidation level profile in neat resin at 1 hour. The predicted oxidation level at the exposed surface after 1 hour of oxidation is 0.1812 and as shown in Figure 8.5, both the predicted profile and the approximate profile have the same oxidation level value at the exposed end. When analyzing heterogeneous models, the oxidation level profile is more complicated in that the profile is piece-wise continuous with the predicted oxidation level continuous within a single material. For example, in the heterogeneous configuration shown in Figure 8.4, the material boundary is at 0.06 mm. Figure 8.7 shows the predicted oxidation level profile for that configuration at 70 hours. The approximated oxidation

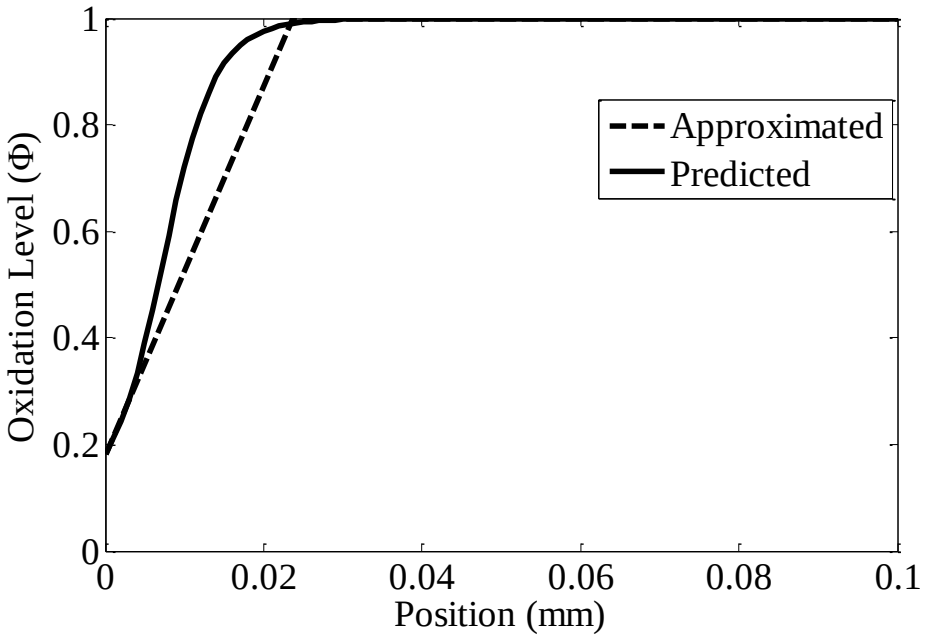

Figure 8.5: Oxidation Level profile in neat resin 1-D model at 1 hour

level profile is also maintained as a piece-wise oxidation level profile for each material region. The approximated oxidation level value in either material region at the material boundary is same as the corresponding predicted oxidation level value for that location.

In order to save the approximated oxidation level profiles for the required time steps so that it can be used by the damage progression model in the coupled simulation, the oxidation level information for each material region in the 1D domain is stored using just four values – the beginning and end locations, and the beginning and end oxidation level values. This information is then used in the coupled damage progression model to determine the oxidation level at each integration point and degrade the mechanical properties based on the constitutive relations.

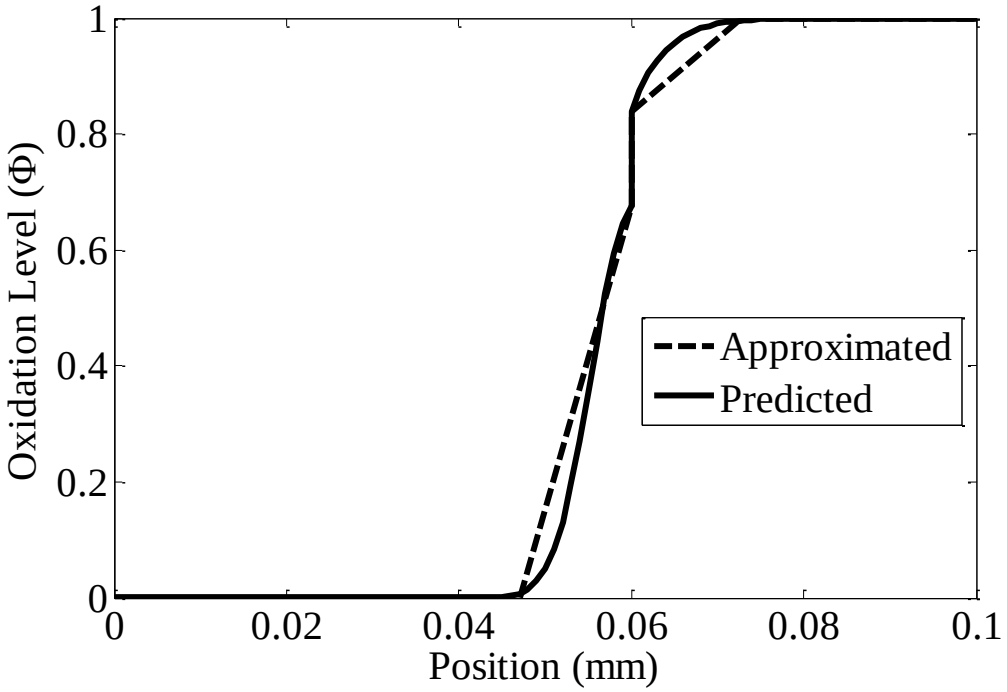

Figure 8.6: Oxidation Level profile in heterogeneous 1-D model (see Figure 8.4) at 70 hours

8.3. Summary

Finite element analysis of the oxidation of a plain weave graphite/PMR-15 textile composite was performed using the decoupled subdomain strategy (DSS). This strategy was presented and validated in previous sections. This section presented the oxidation layer growth through the thickness of a woven mat by inspecting the results of individual 1D domains. The section also describes how the oxidation information from the DSS model is maintained so that it can be used by the damage progression model for prediction of mechanical behavior of a composite subjected to a high temperature oxidizing environment.

9. Oxidation-Damage Analysis of Textile Composites

The previous sections have laid the groundwork in order to be able to build the framework so that the effect of oxidation on the mechanical behavior of textile composites can be predicted. The last three sections describe the challenges and appropriate strategies for simulating the oxidation behavior in textile composites. Section 3 described the governing equations and finite element formulations required for the damage analysis, oxidation analysis and the coupled oxidation-damage progression model. This section begins with a brief overview of the different damage mechanisms in textile composites. This is followed by a description of how the coupled analysis model was used to predict the damage initiation and progression in the textile composites in oxidizing environments. The configurations that will be analyzed will be described including the material properties and the constitutive model that was used to implement the coupled analysis model. This will be followed by the results and discussion of the analysis and the parametric studies.

9.1. Damage mechanisms

Textile composites fail under different types of loadings exhibiting different types of damage mechanisms [48]. One common damage mechanism is transverse cracking in the matrix and tows. Other damage mechanisms seen in the tows are inter- and intra-tow delamination, fiber buckling and fiber breakage etc. Resin pockets in the composite can develop transverse matrix cracks (transverse to the loading direction) independent of the matrix cracks in the tows. Quaresimin et al. [48] observed three main damage mechanisms in twill weave composites under fatigue loading. They are layer delaminations, transverse matrix cracking and fiber failure. Figure 9.1 shows the micrographs illustrating these damage mechanisms. Quaresimin et al. [48] analyzed a number of laminates with different stacking sequences and saw that all three damage mechanisms were present under different types of fatigue loadings, but the sequence of appearance was different. It was also seen that only one predominant mechanism generally dictated the laminate behavior.

Figure 9.2 shows a schematic of the different damage modes in a tow. The mode under which damage occurs in the material depends on which material allowable is exceeded. The failure criteria that are used in this work are discussed in the next section. The damage modes in the tows can be classified into four types as shown in Figure 9.2. The "1" direction denotes the fiber direction whereas the "2" and "3" directions are in-plane and out of plane transverse directions respectively. The coordinate axes defined by the "1", "2" and "3" direction are the principal coordinate axes of the tow, which is assumed to be transversely orthotropic. The finite element model of the composite accounts for the undulation of the tows and therefore the rotation angles for the material vary depending on the location of the material point in the tow. As illustrated in Figure 9.2, fiber breakage occurs under failure mode 11 and this damage mode is generally caused

by excessive σ_{11} stress in the tow. This failure mode is what generally causes the ultimate failure of the composite. Transverse matrix cracking is generally one of early damage mechanisms seen in the tows. This type of damage mode is caused by excessive σ_{22} or σ_{12} stress components and classified as failure modes 22 and 12 respectively. Failure mode 33 and 13 can be caused by either σ_{33} or σ_{13} stress components and can result in intra- or inter-laminar delaminations. Figure 9.2 also shows the damage mode 23 which is caused by σ_{23} stress.

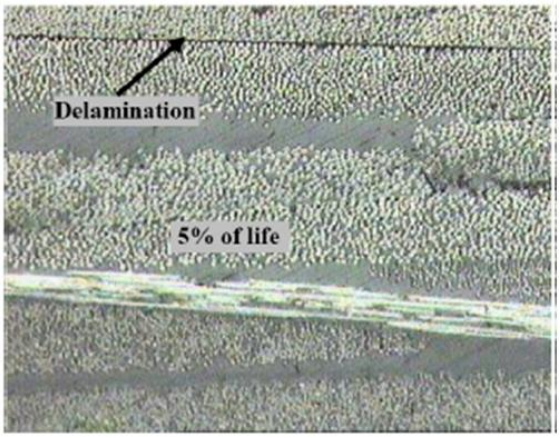

(a) Delamination

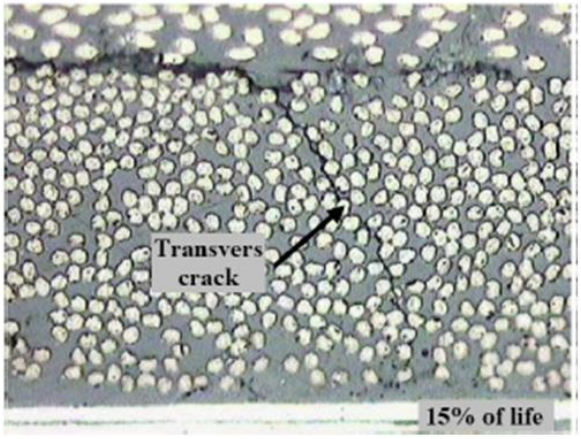

(b) Transverse matrix crack

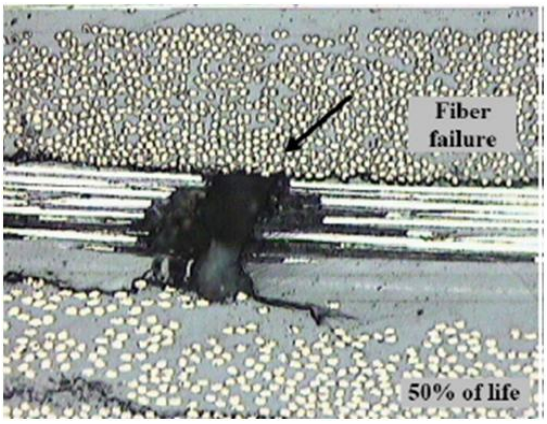

(c) Fiber Failure

Figure 9.1: Damage Mechanisms in woven composites [48]

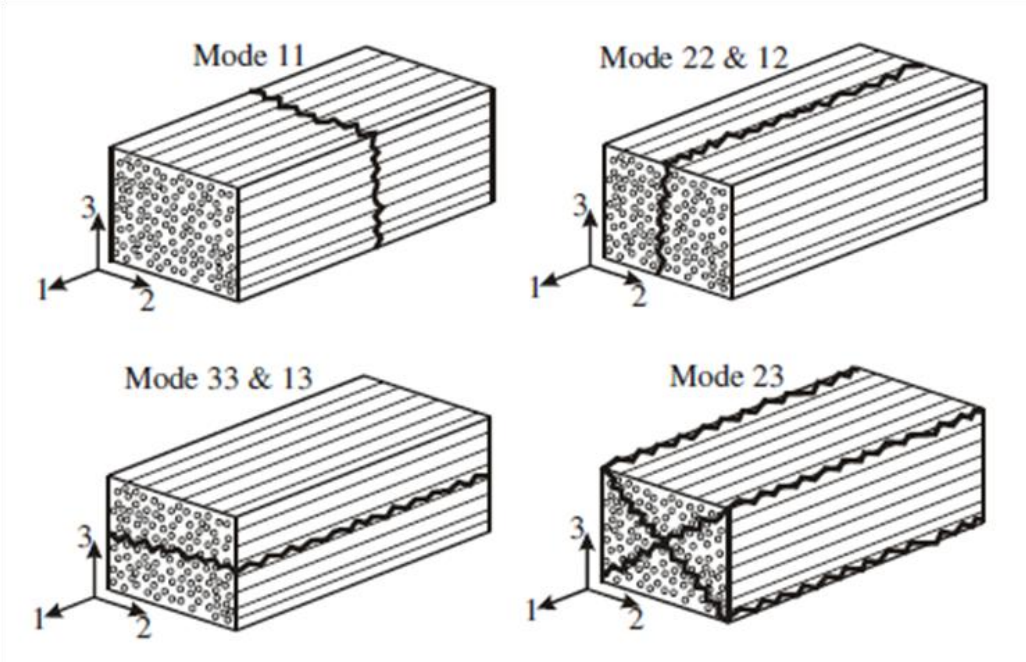

Figure 9.2: Schematic of different damage modes in the tow of textile composites [49]

9.2. Failure criteria for tows and matrix

As mentioned in the previous section, the condition for damage to occur and more specifically, which type of damage mechanism is in action, is determined based on what failure mode has been triggered. In order to determine if a failure mode has been triggered, a suitable failure criterion is required. This section defines the failure criteria employed in all the models used in this work.

Depending upon the property degradation scheme used, a material point in the matrix will be assumed to be isotropic or anisotropic after the damage has occurred. Since the matrix is initially isotropic, the global coordinate system and the material coordinate system are the same. On the other hand, the principal coordinate system is not necessarily the same as the global coordinate system. Moreover, the property degradation scheme used in this work assumes that the material will become anisotropic after mechanical damage. Therefore, it was assumed that there is no significant effect of choosing the maximum stress criterion over the principal stress criterion. In this particular work, the stress in the global coordinate system was used in the maximum stress criterion to determine failure modes in the matrix. However, future enhancements

to the model should provide the option of choosing the maximum principal stress criterion if the material is not damaged.

In the case of the tow material, the maximum stress criterion for anisotropic materials was used, which says that the failure occurs when any of the stress components in the material coordinates system exceeds its corresponding strength. The tows can fail under one or more damage modes such as fiber breaking and transverse cracking. The modes strongly affect the mechanical behavior of the structure. In this work, the tows are assumed to be transversely isotropic before any damage occurs. However, the tow in general would no longer be transversely isotropic after it has failed and its mechanical properties have been degraded. But the stress in the local coordinate system of the tow is continued to be used for the maximum stress failure criterion. If σ_{ij} are the stress components in the material coordinates system of the tow and S_{ij} are the corresponding strength values, then the failure criteria used in this work can be summarized as below:

For isotropic matrix:

Max stress criterion

For transversely isotropic tow:

Max stress criterion (6.1)

$\sigma_{ij} / S_{ij} > 1$ Material point has failed in mode *ij*

$\sigma_{ij} / S_{ij} \leq 1$ Material point has not failed

The strength properties of the materials analyzed in this work is listed in Section 9.4 which defines the all material properties used in this work.

9.3. Configuration

The coupled analysis framework was used to investigate the mechanical behavior of a plain weave Graphite/PMR-15 composite in an oxidizing environment. The waviness ratio of the composite is assumed to be 1/3 and the fiber volume fraction in the tow is assumed to be 55.6%. The reason for choosing this fiber volume fraction was because of the availability of experimental engineering properties for this particular material system in the literature. The volume fraction of the tows in the composite is assumed to be 63.6% and therefore the overall fiber fraction in the composite is 35.36%. The laminate consists of two plies and is assumed to be symmetrically stacked and infinite in the in-

plane directions. Figure 9.3 shows the full unit cell of the configuration. The laminate is assumed to be loaded under uniaxial stress conditions in the x-direction at a temperature of 288C. The material properties used to model the configuration will be assumed to be those at 288 C. However, in this current implementation of the coupled analysis model, the effects of thermal expansion and the shrinkage of resin under oxidation will be ignored. The configuration will be loaded to a pre-determined strain level and maintained at that level. The configuration is then exposed to oxygen from the top and bottom surfaces while the lateral surfaces are assumed to be impermeable. The laminate will be exposed to the oxygen for 200 hours at 288C. The damage in the laminate throughout this simulation will be tracked and the mechanical behavior will be recorded. The number of plies in the laminate was changed in a parametric study to determine its effect on the mechanical behavior. Any changes from this basic configuration will be described as required when discussing the results of the parametric study.

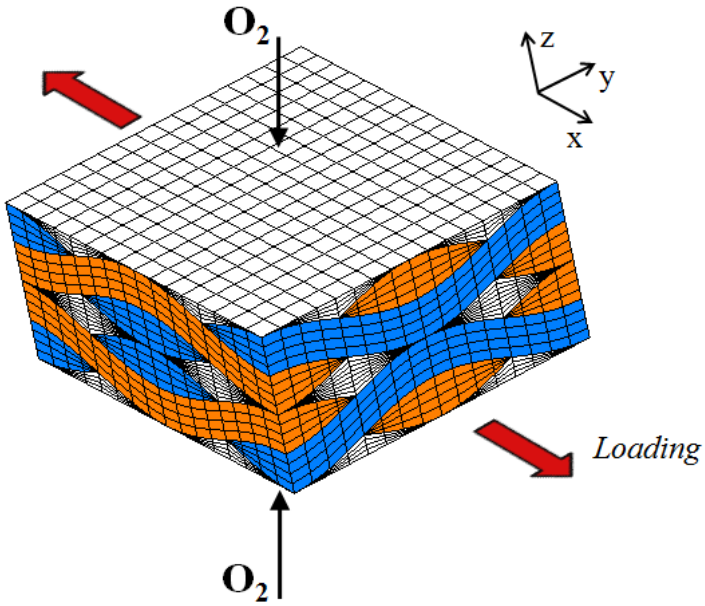

Figure 9.3: Two-ply plain weave composite configuration

Exploiting symmetry conditions in this configuration allows reducing the analysis domain from a full unit cell to just $1/8^{th}$ of the unit cell as shown in Figure 9.4. For all the results discussed in this section, the analysis domain, which is the $1/8^{th}$ unit cell, is part of the bottom ply in the configuration. Therefore, the bottom surface of the model in Figure 9.4 is traction-free and exposed to oxygen.

9.4. Material system

The material system used for all the analyses discussed in this section is Graphite/PMR-15 composite. The coupled model requires both the oxidation material properties as well as the mechanical properties for the tow and matrix in the composite. Note that the configuration is assumed to be at a temperature of 288 C throughout the entire simulation. The coupled model also requires the degradation schemes for the matrix and the tow, for both the oxidation as well as mechanical damage. These degradation schemes are described in the next section.

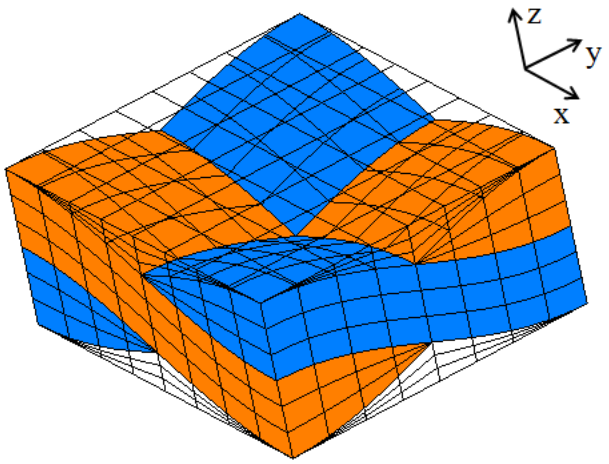

Figure 9.4: Analysis domain ($1/8^{th}$ unit cell) with transparent matrix

The oxidation material properties that are used in these models have already been described in the previous sections that discuss the oxidation behavior in composites. The oxidation material properties for the neat PMR-15 resin were obtained from ref [25]. The oxidation material properties for the tow were determined using the homogenization strategies described in Section 3. Table 5.1 gives the oxidation material properties for the neat PMR-15 resin and Table 7.1 gives the corresponding properties for the tow.

Obtaining the mechanical properties for the Graphite/PMR-15 material system at 288 C is not easy since they tend to change over time and it may not be appropriate to use property data from different sources or manufacturers over different time periods. That being the case, it is also very difficult to obtain the entire set of required mechanical properties from one source in the literature. Moreover, some of the required properties at 288 C are unavailable due to the lack of appropriate experimental techniques to determine them. The resin and the tow are also assumed to be linear elastic materials although elasto-plastic behavior of the polyimide resin would be expected to be more prominent at 288 C. Overall, the set of mechanical properties for the material system used in this work was chosen from a combination of different sources in the literature and based on certain assumptions and estimates that are described below.

The mechanical properties of the neat PMR-15 resin were chosen based on experimental data from Pochiraju and Tandon [30]. The Young's modulus of the neat resin was found to be 2.096 GPa and the Poisson's ratio is assumed to be 0.30 in Pochiraju and Tandon's work [30]. Based on the assumption that the neat matrix is isotropic, the Young's modulus and Poisson's ratio can be used to calculate the shear modulus. Pochiraju and Tandon [30] also provide the normal strength at room temperature and 288 C. The shear strength of the neat PMR-15 resin is calculated by scaling the strength at room temperature based on the change in normal strength from room temperature to 288 C. Table 9.1 contains the elastic moduli for neat PMR-15 resin that were used in this work. The strength properties that were discussed in this paragraph are provided under Set 1 in Table 9.2. The properties under Set 2 and the need for an additional set of strength properties are discussed in the next paragraph.

The Graphite/PMR-15 tow is assumed to be transversely isotropic and therefore its elastic behavior is defined by five independent properties. The engineering properties for the tow were harder to obtain because the configuration requires properties at 288 C. The elastic moduli chosen were interpolated from work performed by Odegard and Kumosa [50], which looked at the effect of temperature on some of the engineering properties of a Graphite/PMR-15 unidirectional laminate (V_f=55.6%). Of the five independent properties required, E_{11}, E_{22}, ν_{12} and G_{12} were obtained by interpolating from the data in Ref [50]. The Poisson's ratio in the transverse plane, ν_{23}, at 288 C was assumed to be the same as that at room temperature. The elastic moduli for the tow material are summarized in Table 9.1. All the strengths properties of the tow at 288C were not available in the literature. It is relatively difficult to determine all the strength properties for the tow. These properties, especially the matrix-dominated properties, are hard to determine, because of many factors like the material interface properties that influence the strengths. The σ_{22} strength and σ_{12} strength were interpolated from Odegard and Kumosa's work[50]. Since, the tow is assumed to be transversely isotropic, the σ_{33} strength is the same as the σ_{22} strength and the σ_{12} strength is the same as the σ_{13} strength. Due to lack of experimental data for the fiber-dominated σ_{11} strength, the corresponding strength from a Graphite/epoxy material system was used. However, the σ_{11} strength is only consequential only during fiber-breakage which occurs during final failure of the composite. Therefore, this assumption was not considered to be significant because this work is more concerned with the damage initiation and progression then the final failure of the composite. Also, due to lack of experimental data for the σ_{23} strength, it was assumed to be the σ_{23} stress corresponding to the same strain level at which the σ_{12} stress mode failed. These strength properties for the tow are summarized under Set 1 in Table 9.2. Note that the σ_{22} strength of the tow in Set 1 is considerably lower than the normal strength of the neat resin. This would indicate that the tows would fail before the neat resin pockets in the composite. It is common for a composite to have a lower transverse tensile strength than the tensile strength of the neat resin [51]. However, since the properties for this material system were compiled from different sources and

therefore as mentioned before, not particularly reliable, another set of assumed strengths were also chosen for the material system. In this new set of properties, the normal and shear strength of the neat resin were scaled down based on typical strength ratios between resin and tow transverse strengths in Graphite/Epoxy material systems. This additional set of strength properties for the material system used in this work is defined as Set 2 in Table 9.2. Having two sets of material properties would also give another perspective on the damage initiation and progression behavior based on the change in engineering properties.

Table 9.1: Elastic properties for the Graphite/PMR-15 material system [50,30]

	Resin Neat PMR-15	Tow Graphite/PMR-15
E11	2.096 GPa	124.05 GPa
E22=E33	2.096 GPa	6.2 GPa
G12=G13	0.806 GPa	1.62 GPa
G23	0.806 GPa	1.929 GPa
v12=v13	0.3	0.485
v23	0.3	0.607

Table 9.2: Strength properties for the Graphite/PMR-15 material system [50,30]

	Set 1		Set 2	
	Resin Neat PMR-15	Tow Graphite/PMR-15	Resin Neat PMR-15	Tow Graphite/PMR-15
S11	41	2550	12	2550
S22	41	18.91	12	19
S33	41	18.91	12	19
S12	73.72	36.83	12	37
S23	73.72	43.85	12	44
S13	73.72	36.83	12	37

All strengths in MPa

9.5. Constitutive relations

This section describes the different constitutive relations that are required to implement this coupled oxidation-damage progression model. This includes the mechanical property degradation schemes both due to mechanical loading as well as due to the effect of oxidation. The section also talks about how the two degradation schemes are combined and used in the coupled model to obtain the overall mechanical properties of the material based on the oxidation and damage state.

9.5.1. Property degradation based on mechanical damage

When a failure mode is triggered during the damage analysis, the engineering properties are degraded to account for the change in mechanical behavior. This operation is conducted based on a property degradation scheme, which has been briefly discussed in Section 3. In this work, the failure criteria and the property degradation scheme is applied on each integration point within every element in the model. The property degradation scheme is implemented such that a material point that has already failed under a particular mode can fail under another mode. In such a case, the material properties are degraded based on which failure mode prescribes the larger degradation.

Different property degradation schemes have been proposed in the literature by several researchers such as Whitcomb et al. [52], Blackketter et al. [53], Tamma et al. [54] and Zako et al. [55]. All these models share certain similarities and differences. They are similar in the sense that each of them controls the amount of degradation under different failure modes for both the tow and the matrix. Goyal [49] performed a comparison of the different degradation schemes and developed a common framework that allowed implementation of a wide variety of degradation schemes.

For all the damage progression models in this work, the degradation scheme by Blackketter [53] was used. This type of degradation scheme has been widely used by many researchers [52,56-58] to predict initiation and progression of damage. The engineering properties are degraded as specified in Eq.(3.6). The degradation scheme used is different for the tow and the matrix.

In the degradation scheme for the tow material, the values of the degradation parameters, a_i (i=1 to 6) are 1, 5 or 100. Note that the value of the parameters in a_i will be different under different damage modes. Table 9.3 gives the values of the degradation factors for the tow material under this scheme. The "1" is the local fiber direction of the tow and "2" and "3" are the local transverse directions of the tow. An a_i value of 1 indicates that the modulus has not been degraded. An a_i value of 5 indicates the modulus has been degraded to 20% of its original value and similarly an a_i value of 100 indicates the modulus has been degraded to 1% of its original value. The reason that some of the moduli are degraded to 1% of the original rather than an absolute zero is to avoid numerical instabilities[53]. The shear moduli were not reduced to less than 20% of the original value under mode σ_{22} and σ_{33} failure because it is assumed that some shear stiffness remains due to frictional resistance still present on the failure plane [53].

For the matrix material, the property degradation was assumed to be the same under all the failure modes. The tensile moduli and Poisson's ratios of the matrix are reduced to 1% of its original value whereas the shear moduli are reduced to 20% of its original value. The matrix is therefore assumed to become anisotropic after failure. Table 9.4 gives the degradation factors for the matrix material.

Table 9.3: Degradation parameters (a_i) for engineering elastic properties of the tow [53]

	Mode σ_{11}	Mode σ_{22}	Mode σ_{33}	Mode σ_{12}	Mode σ_{23}	Mode σ_{13}
E11	100	1	1	1	1	1
E22	100	100	1	100	100	1
E33	100	1	100	1	100	100
G12	100	5	1	100	100	1
G23	100	5	5	1	100	1
G13	100	1	5	1	100	100
v12	100	1	1	1	1	1
v23	100	100	1	100	100	1
v13	100	1	1	1	1	1

Table 9.4: Degradation parameters (a_i) for engineering elastic properties of matrix [53]

	All Modes
E11	100
E22	100
E33	100
G12	5
G23	5
G13	5
v12	100
v23	100
v13	100

9.5.2. Property degradation based on oxidation damage

The effect of oxidation on the mechanical behavior of the composites is considered in the coupled analysis models used in this work. In reality, the mechanical behavior is probably more tightly coupled with the oxidation behavior than what is assumed in the current model because the mechanical damage can affect the oxidation behavior by allowing more oxygen to penetrate the composite material. This can further affect the mechanical behavior because more oxidation will cause more damage in the composite. These complex effects are not considered in this current work. In this work, the oxidation is assumed to affect the mechanical behavior, but not the converse.

A simple constitutive relation or property degradation scheme was developed to account for the effect of oxidation on the mechanical behavior and is described in Section 3. For a general orthotropic material, the engineering moduli are modified according to Eq.(3.6). Unlike the property degradation scheme for mechanical damage, there is no failure criteria on which the degradation scheme is based.

While the property degradation scheme due to mechanical damage typically reduces the value of the moduli, the same is not necessarily the case for the property degradation

scheme for oxidation. Experimental work has shown that the stiffness of the fully oxidized matrix is typically larger than that of the un-oxidized material [25]. There is not enough data in the literature in order to determine all the degradation parameters, b_i. In order to implement the degradation scheme for this work, the best available data in the literature was used where appropriate and estimates based on certain assumptions were used to the remaining parameters. The values of b_i chosen for the matrix and tow materials in this work are given in Table 9.5. Experiments showed that the elastic modulus of the neat PMR-15 resin increased by about 20% when fully oxidized [25]. The same amount of increase is assumed to apply for the shear moduli. The Poisson's ratio is assumed to remain constant based on the assumption that the matrix remains isotropic after oxidation. The same challenges exist for obtaining accurate characterization data for tows or unidirectional laminates. The fiber is assumed to be impermeable and unaffected by the oxidation. Simple micromechanics analyses showed that effective tow properties were changed by a very small amount when the matrix moduli were increased by 20%. Since the change was insignificant, the degradation properties (b_i) for the tow were assumed to be zero, meaning that the elastic properties of the tow were assumed to remain constant after oxidation. Therefore, an undamaged material point in the tow was assumed to remain transversely isotropic after the material was oxidized.

As mentioned in Section 3, the property degradation scheme based on oxidation also degrades the strength properties of the materials in the composite as defined by Eq.(3.103). There is no data in the literature that can be used to determine the strength degradation parameters, d_i. Due to this limitation, for all the models analyzed in this work, strength properties are assumed for the fully oxidized matrix and tow. Table 9.6 gives the values of the strength degradation parameters chosen for the matrix and tow. The strengths for all stress components in the matrix are assumed to drop to half its value. In the case of the tow material, the σ_{11} strength, which is the strength in the fiber direction, is assumed to drop to 95% of the original value whereas all the other strengths drop 50%.

Table 9.5: Parameters (b_i) for degrading engineering elastic properties of matrix and tow

	Engineering property affected	b_i	
		Matrix	Tow
1	E11	+0.2	0.0
2	E22	+0.2	0.0
3	E33	+0.2	0.0
4	G12	+0.2	0.0
5	G23	+0.2	0.0
6	G13	+0.2	0.0
7	v12	0	0.0
8	v23	0	0.0
9	v13	0	0.0

Table 9.6: Parameters (d_i) for degrading strength properties of matrix and tow

	Strength property affected	d_i	
		Matrix	Tow
1	S11	-0.50	-0.05
2	S22	-0.50	-0.50
3	S33	-0.50	-0.50
4	S12	-0.50	-0.50
5	S23	-0.50	-0.50
6	S13	-0.50	-0.50

The overall mechanical moduli of the material are obtained by combining the two degradation schemes, both based on mechanical damage as well as oxidation, as described in Section 3.The expressions for the overall properties at a material point are given by the Eq.(3.104). Note that although the degradation scheme chosen in this work assumes that the matrix remains isotropic after oxidation, the overall mechanical properties obtained after accounting for mechanical damage need not necessarily represent an isotropic material. The parameters, a_i, have a value of 1 if the material is not damaged and therefore in such a case, the matrix would remain isotropic. On the other hand, if the matrix is damaged under any mechanical failure mode, the matrix becomes anisotropic. Similarly, the tow need not remain transversely isotropic after the mechanical properties have been modified using Eq.(3.104).

9.6. Results and discussion

The coupled analysis model was used to simulate damage initiation and progression in the configuration described in Section 9.3. The basic configuration described in Section 9.3 is a two-ply laminate at 288 C with the top and bottom surfaces exposed to oxygen. The laminate is assumed to be infinite in the in-plane directions and has a uniaxial load

in the x-direction. As described in Section 9.4, two sets of material properties were chosen to model the Graphite/PMR-15 material system. This section will discuss the results from the analyses performed using both sets of properties. A parametric study was also performed where the number of plies in the laminate was increased. The parametric study looked at two-, four- and six-ply laminates for both the sets of material properties. The results of this parametric study will be described in this section as well.

9.6.1. Two-ply laminate

The damage progression behavior of the laminate under mechanical load alone (i.e. no oxidation) is first discussed. The laminate is assumed to be quasi-statically loaded uniaxially while maintained at a temperature of 288 C. Since two sets of material properties were chosen to define the Graphite/PMR-15 material system, the damage analyses were performed on two models, one for each material property set. Note that the two sets of material properties have the same elastic moduli. The difference between the two sets of material properties is in the strengths properties as shown in Table 9.2. Figure 9.5 shows a plot of the volume averaged σ_{xx} versus the volume averaged ε_{xx} for both the models. As expected, the stress-strain behaviors are different for the two models. Figure 9.5 shows that the initial damage in the model using Set 1 properties causes a significant drop in load (indicated by A) compared to the initial damage in the model using Set 2 properties (indicated by B). This difference in behavior can be explained by looking at where the initial damage occurs. In the case of Set 1, in which the transverse tow strengths are much lower than the matrix strengths, damage initiated in the fill tow under compressive σ_{33} damage mode. The observation that parts of the fill tow closer to the laminate mid-plane are under compression can be explained by considering that warp tows are being stretched because of the load and therefore pushing on the fill tows in between. When the material properties of the damaged area in the fill tow are degraded, the amount of load carried by the tow reduces. In the case of Set 2, in which the resin has the lowest strengths, the damage initiates in the matrix pockets under

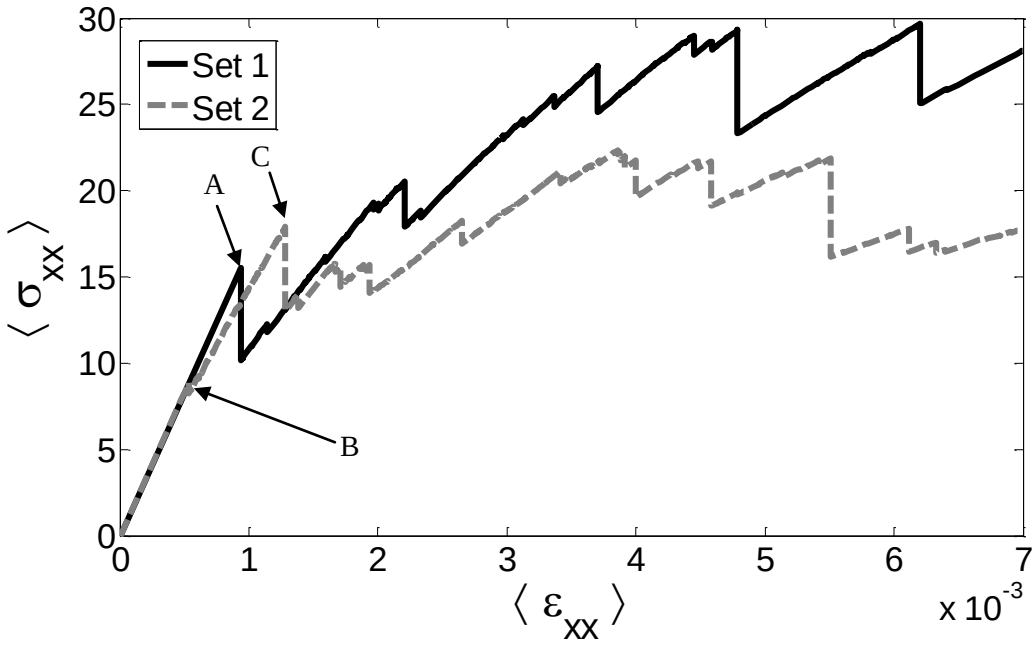

Figure 9.5: Volume averaged stress-volume averaged strain curves for the two-ply laminate without oxidation

tensile σ_{33} damage mode but since the matrix doesn't carry as much load as the tows, the load drop is not as significant as that seen in the model with Set 1 properties. This explanation can be confirmed by looking at the damage evolution in the two models.

Figure 9.6 shows the evolution of damage in the different constituents of the model using Set 1 material properties. It shows the location of the initial damage in the fill tows at a volume averaged ε_{xx} strain level of 0.0935% strain. The initial damage occurs under compressive σ_{33} damage mode. It can be seen that the matrix is the last constituent in the composite to have significant failure. Looking at the column for 0.6% strain in Figure 9.6 shows that the there is significant transverse damage in the fill and warp tows but there is hardly any damage in the matrix. This behavior was also expected based on the fact that the Set 1 material properties have the transverse tow strengths much lower than that of the matrix.

In comparison, Figure 9.7 shows the evolution of damage in the model using Set 2 material properties. In this case, it shows that the damage initiates in the matrix under tensile σ_{33} mode near the mid-plane of the laminate at a volume averaged ε_{xx} strain level of 0.0473%. Note that the damage initiates at a much lower strain level when using Set 2 material properties versus those in Set 1. Although the initial damage in the Set 2 model is in the matrix, the first significant drop in load is at a strain level of 0.128% (indicated by C in Figure 9.5) and it is caused by damage in the fill tow under

compressive σ_{33} failure mode. In comparison, the first significant drop in the Set 1 model occurs at 0.0935% strain (indicated by A in Figure 9.5) under the same type of failure mode. The reason why the damage in the fill tow occurs at a higher strain level in the Set 2 model could be explained as follows. When the Set 2 laminate is at 0.0935% strain, there is already some damage in the matrix pockets. This would make the matrix pockets more compliant and thereby effectively reducing the constraints on the fill tow. The fill tows would be allowed to deform more freely than before matrix damage occurred and therefore relieving the σ_{33} stresses in the fill tow. Thus, a larger load would be required to raise the σ_{33} stress in the fill tow enough to cause damage.

In comparison to the evolution of damage in the Set 1 model, the matrix has much more damage at 0.6% strain. Also, there are slight differences between the damaged locations in the tows. This is probably because of the manner in which the load is transferred when different locations in the laminate start to fail.

The results discussed up to this point considered only the effect of damage due to mechanical loading. Now the results from the coupled models are discussed. The coupled models simulate the mechanical behavior when the laminate is under a fixed mechanical loading and is then exposed to oxygen from the top and bottom surfaces for 200 hours. These simulations are performed at different fixed mechanical loads. Similar simulations are performed on models with each set of material properties to determine the effect of the properties on the behavior.

The behavior of the model using Set 1 material properties is discussed first. As illustrated in Figure 9.6, damage due to a mechanical-only load initiates at a strain level of 0.0935%. A coupled model simulation was performed at a strain level of 0.09% to see if the oxidization would initiate any damage. It was seen that there was no effect of oxidation on the damage behavior throughout the 200 hours. This is because, as shown in Figure 9.6, all the initial damage is located in the top half of the fill tow in the model, which implies that the stress failure index is highest in that region of the fill tow. This region in the model corresponds to the interior of the laminate because the analysis domain represents the lower half of the laminate. After 200 hours of oxidation, the oxidation front has not reached the interior of the laminate far enough to affect the engineering properties of the tow to cause damage. As defined in Table 9.5, the change in engineering moduli is not significant enough to affect the stresses. The changes in the strength properties are significant, but the regions with the stress concentrations are either not oxidized, or not oxidized enough to cause damage in the fill tows.

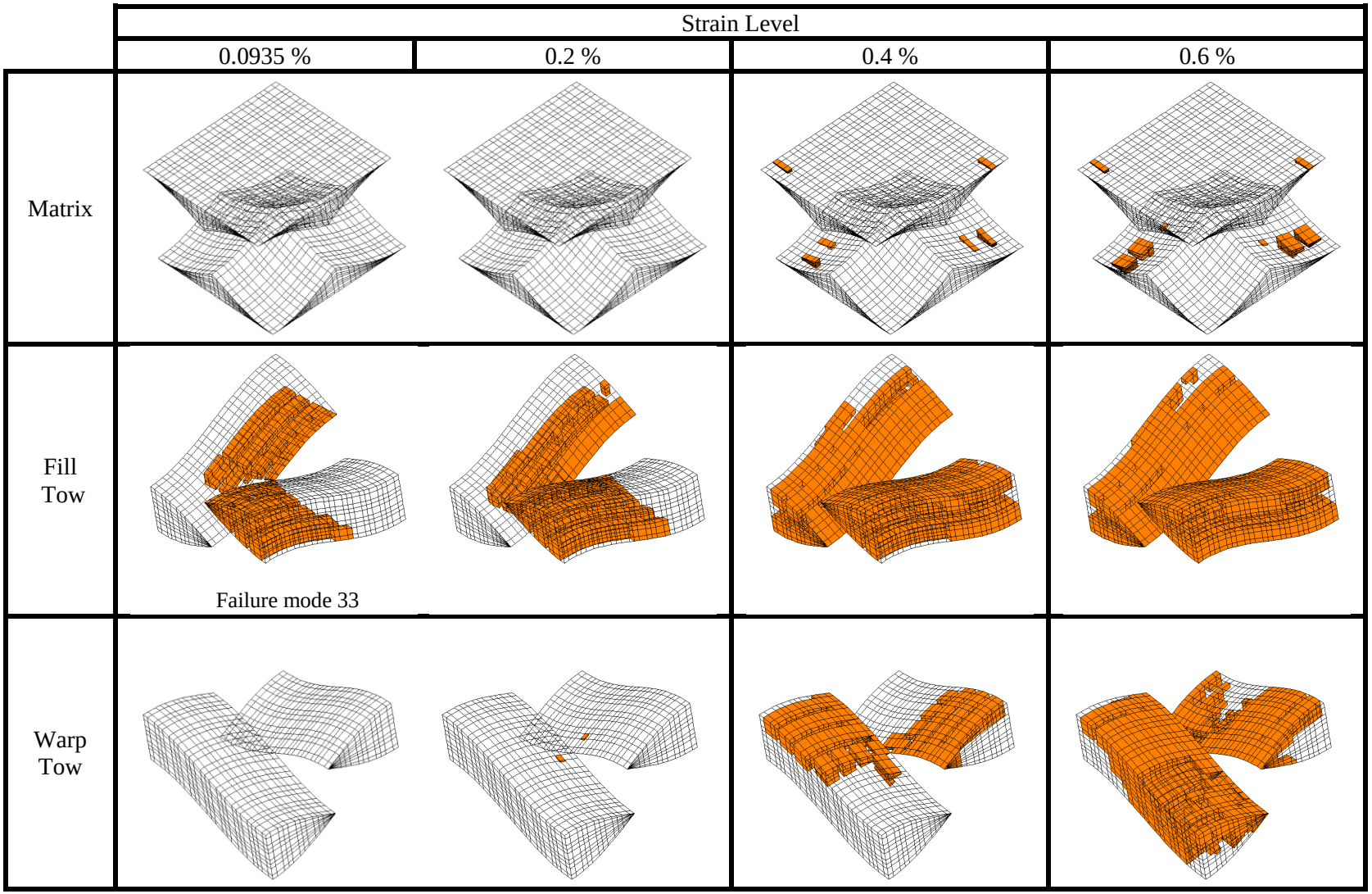

Figure 9.6: Evolution of damage in the two-ply laminate configuration without oxidation using Set 1 material properties

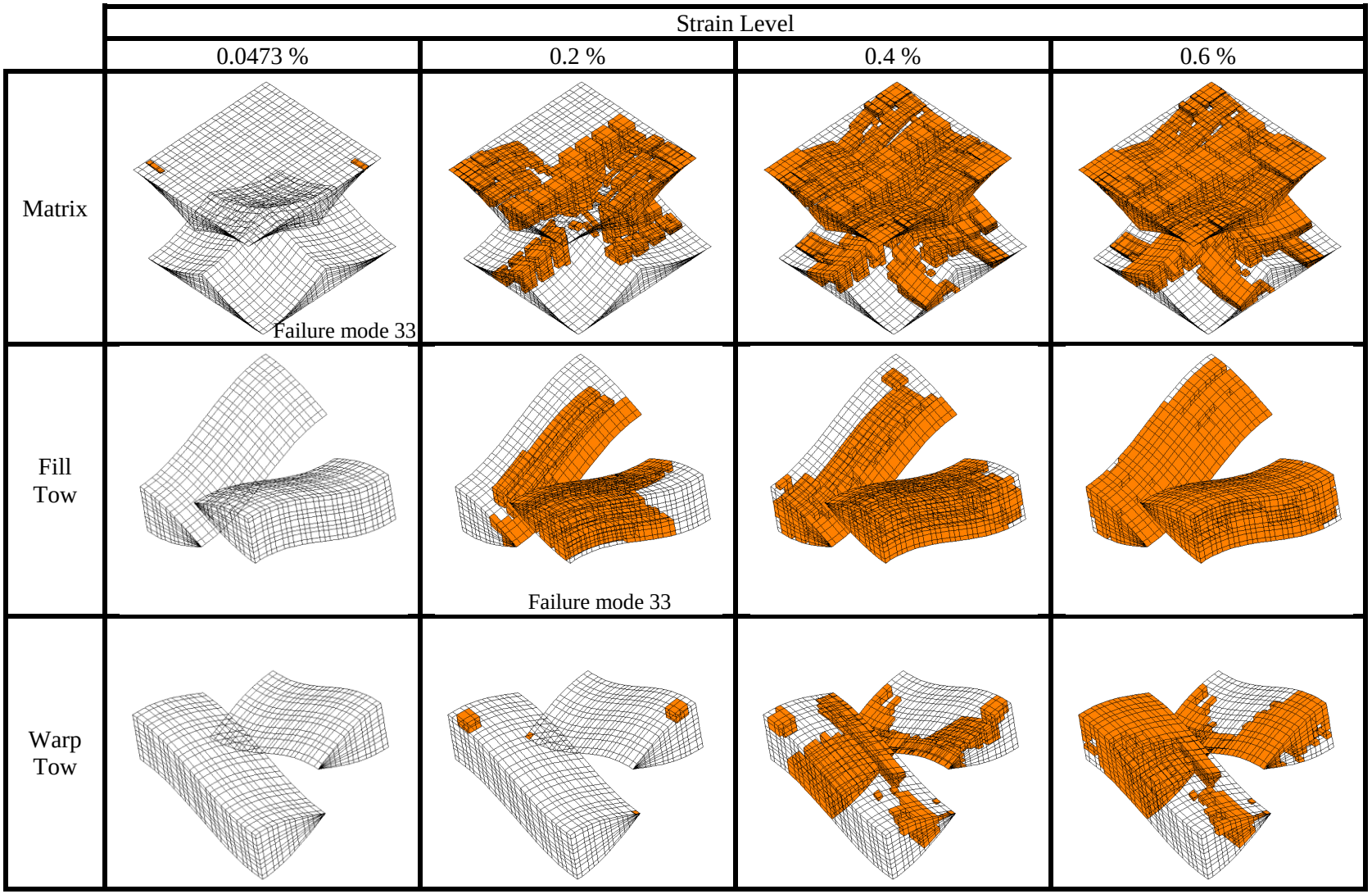

Figure 9.7: Evolution of damage in the two-ply laminate configuration without oxidation using Set 2 material properties

The simulations were also performed at strain levels of 0.2% and 0.4%. Since the configuration is assumed to be already loaded to a constant strain level, the configuration should also be assumed to have the damage that would have ordinarily occurred without the influence of oxidation. This initial damage state for a particular load level is assumed based on the corresponding damage state for the model from the standard damage progression analysis. In the model with Set 1 material properties at a strain level of 0.2%, the damage at the beginning of the oxidation simulation is almost entirely in the fill tow as shown in Figure 9.6. There is no damage at all in the matrix. The only other damage in the configuration is one integration point in each warp tow that has failed in the σ_{33} damage mode as shown in Figure 9.6. Figure 9.8 shows the evolution of damage as the oxidation progresses for 200 hours. After one hour of oxidation, there is new damage under σ_{22} and σ_{33} failure modes in the bottom region of the fill tow where the oxygen is slowly making its way into the interior of the laminate. The simulation also shows some slight damage in the matrix pocket closer to the exposed surface of the laminate. There is also some damage in the σ_{22} failure mode in the lower half of the warp tow, which can be explained due to the oxidation front creeping into the interior of the laminate. The more interesting behavior is that regions of the top half of the warp tow fails in the σ_{33} damage mode. This is interesting because the damage is seen after only one hour of oxidation, at which time the oxidation front has not reached even close to the top half of the model. This can be explained by the redistribution of the load in the configuration after material damage. As mentioned earlier, even before oxidation began, there was damage in the fill tow. Figure 9.8 shows that after only one hour of oxidation, there is significant damage in the fill tow, which renders most of the fill tow incapable of carrying load. This increases the load on the warp tow. The effect of the external load on the laminate is to straighten the undulating warp tows, which causes a tensile σ_{33} in the top half of the tow. When the load on the warp tow increases, it also increases the σ_{33} stress in the top half of the tow making it exceed the strength. This behavior shows that the influence of oxidation on the mechanical behavior is not always localized and in some cases, its effect can be seen in the interior of the laminate where the material has not been oxidized.

Figure 9.9 shows the initial damage state in the two-ply laminate at 0.4% strain before oxidation begins. It shows that there is very little damage in the matrix pockets. The fill tow on the other hand has considerable damage in the σ_{22} and σ_{33} failure modes. Figure 9.9 also shows that warp tow has some damage in the top half under mainly the σ_{33} failure mode. As the oxidation progresses, some build-up of σ_{11} damage is seen in the lower matrix pocket as shown in Figure 9.9. There is little new damage in the fill tow since most of the tow was already damaged before the oxidation began. The warp tow sees considerable new damage under the σ_{22} failure mode in the bottom half of the tow as oxidation progresses. This can be explained by the fact that the fill tow is mostly damaged and much of the load is now carried by the warp tow. Therefore, the warp tow

would experience higher stresses. In addition to the higher stresses, the oxidation causes the strengths to drop by 50% thereby increasing the potential of failure.

Figure 9.10 shows the plot of the volume averaged σ_{xx} with the volume averaged ε_{xx} for the Set 1 model indicating the drop in the volume average σ_{xx} at the end of 200 hours of oxidation for the two simulations discussed earlier. It shows that for the 0.2% strain level simulation, the volume averaged σ_{xx} stress reduced from the point labeled A to A' indicating a drop of 15% at the end of 200 hours of oxidation whereas in the case of the 0.4% strain level, the corresponding stress dropped over 22% indicated by the line B-B'. Figure 9.11 shows the volume averaged σ_{xx} for all three simulations normalized with the initial volume averaged stress as the oxidation progresses over 200 hours. As mentioned earlier, at the 0.09% strain level, there was no new damage due to oxidation and therefore there was no drop in the volume averaged stress. Instead, there was a slight increase in the volume averaged stress due to the fact that the stiffness in the matrix increases when oxidized but the increase is so small that it is not noticeable in Figure 9.11. In the case of the 0.2% strain level, a significant part of the stress drop occurs in the beginning of the oxidation process within the first two hours. This indicates that the damage that occurred in the remaining 198 hours was not significant enough to reduce the load in the laminate. In the case of the 0.4% strain level, a major portion of the stress drop occurs at a single time step at 53.33 hours when the stress drops to 78.3% of the initial stress. The damage that occurs before and after that point accounts for just 0.7% of the total drop in load.

The results from the simulations of the laminate using the Set 2 material properties are discussed next. Similar to the simulations on the laminates with Set 1 material properties, three simulations were performed with strain levels of 0.1%, 0.2% and 0.4%. In the simulation with 0.1% strain, the initial damage, as shown in Figure 9.12, is confined to mostly the inter-laminar matrix pocket. There is also slight damage under σ_{33} failure mode in the top part of the warp tow. The coupled analysis shows that there is no new damage caused due to the effect of oxidation. This is similar to the model with Set 1 material properties and 0.09% strain, where the stress state in the oxidized materials is not significant enough to cause new damage. With 0.2% strain, the initial damage is, as expected, more widespread than that in the case with 0.1% strain. As shown in Figure 9.13, the damage in the inter-laminar matrix pocket has increased in

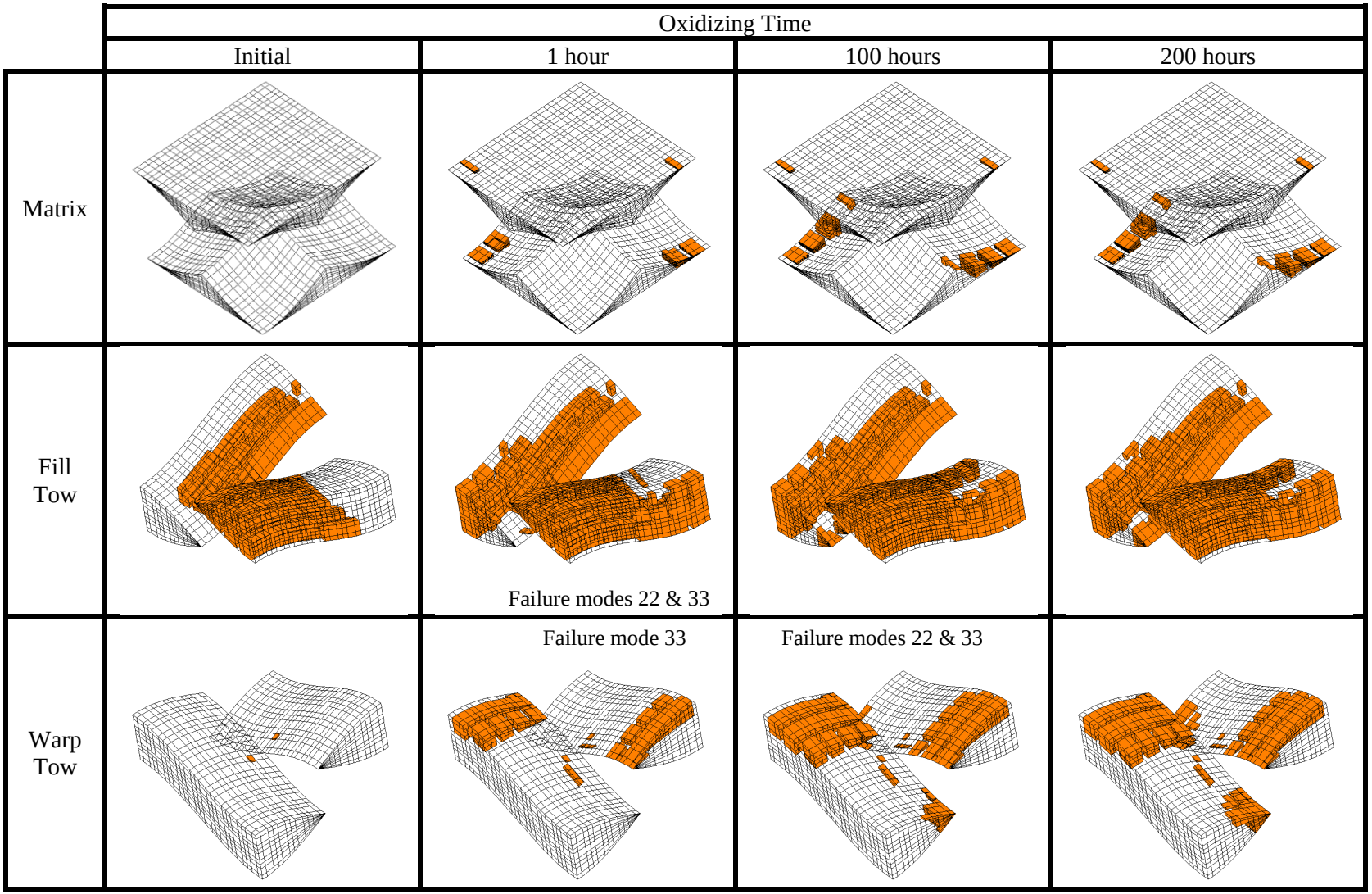

Figure 9.8: Evolution of damage due to oxidation in the two-ply laminate at 0.2% strain using Set 1 material properties

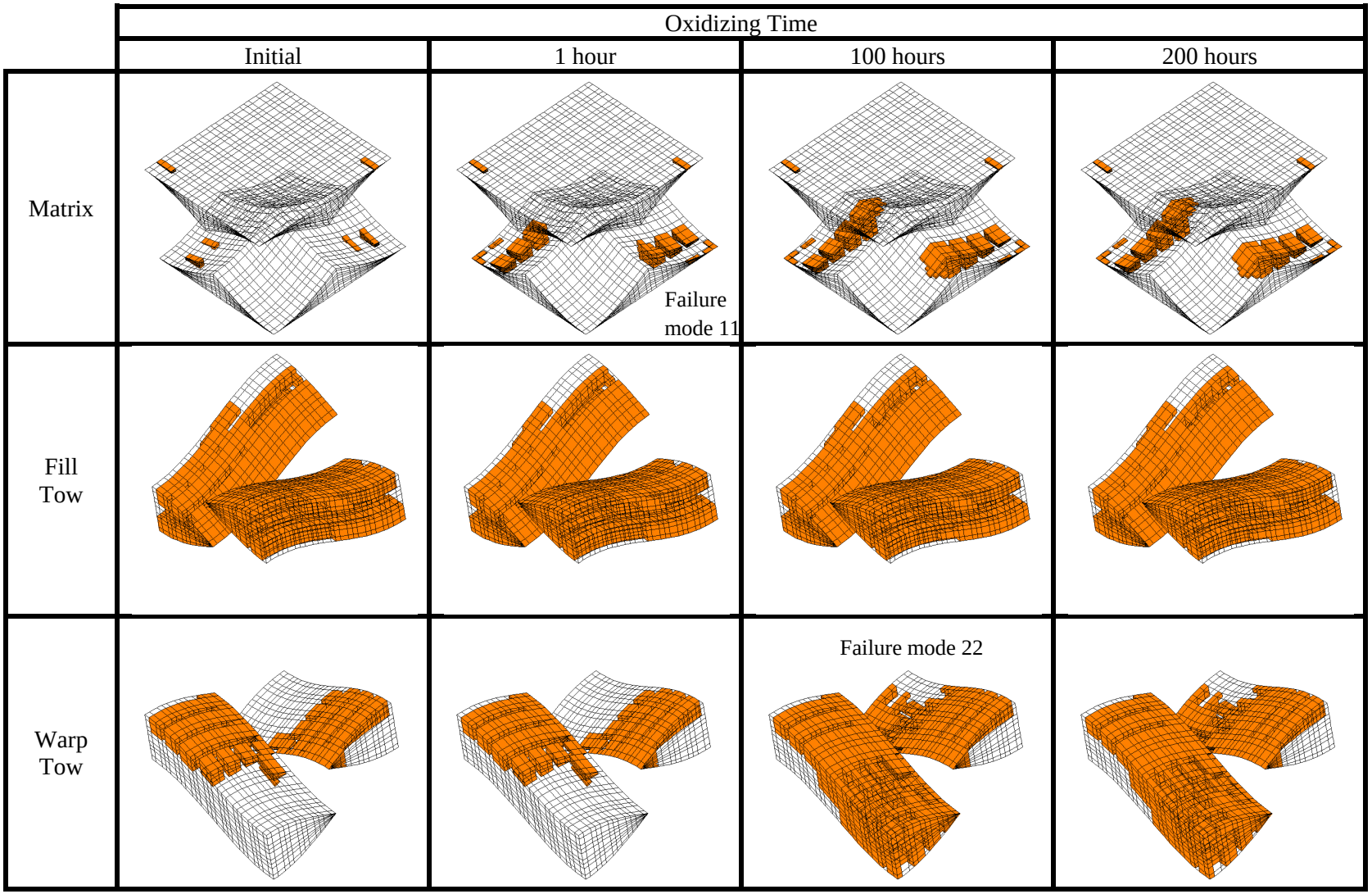

Figure 9.9: Evolution of damage due to oxidation in the two-ply laminate at 0.4% strain using Set 1 material properties

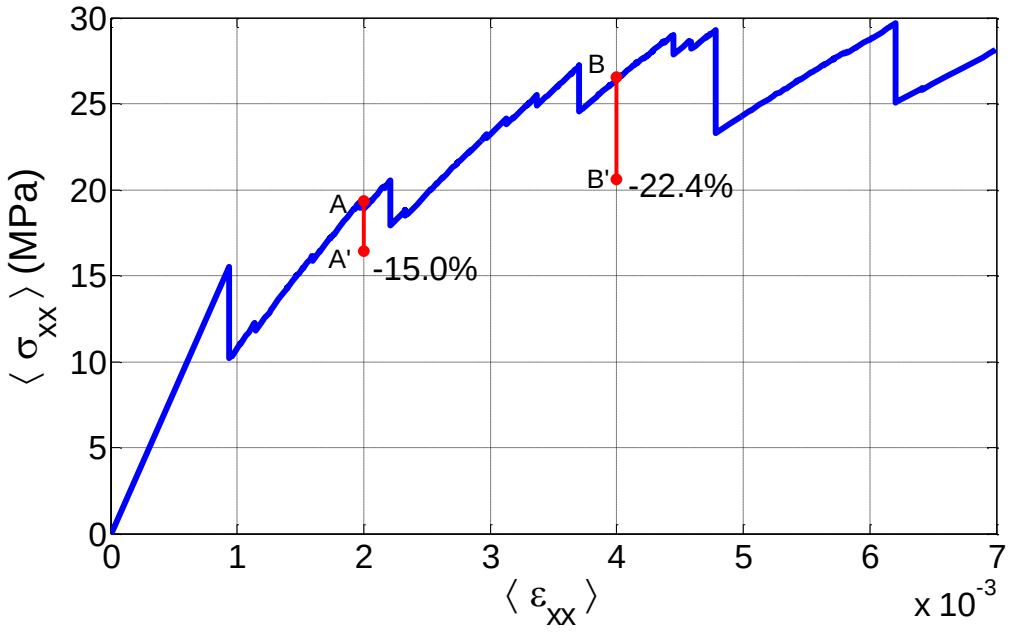

Figure 9.10: Volume averaged stress-volume averaged strain for the Set 1 material two-ply laminate showing drop in stress after 200 hours of oxidation

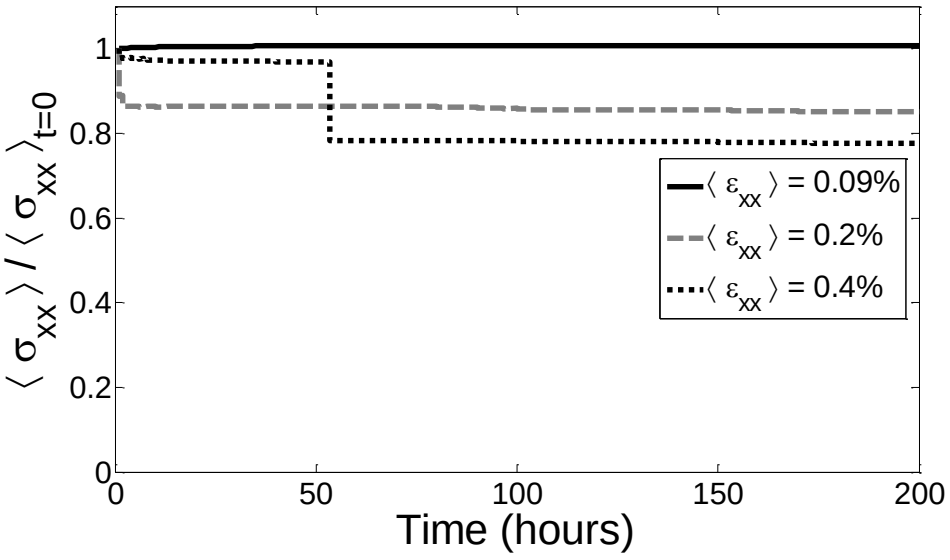

Figure 9.11: Variation in volume averaged stress due to oxidation for the Set 1 material two-ply laminate at different strain levels

addition to new σ_{11} failure in the bottom matrix pocket. The fill tow has σ_{22} and σ_{33} failure in regions from the bottom to the top, with more damage in the latter. Figure 9.13 also shows that the damage in the warp tow increased. The simulation predicted that the damage in the lower matrix pocket grows mostly under σ_{11} and σ_{22} failure modes. The simulation also predicts, as shown in Figure 9.13, that there is new damage in the bottom part of the fill tow under the σ_{22} failure mode. This can be explained as a direct effect of the oxidation of the tows which reduces the strength by as much as 50%. The warp tow also has new damage growth as an effect of the oxidation. As shown in Figure 9.13, the warp tow starts to see damage in the lower part of the tow under σ_{22} failure mode as the oxidation progresses. The warp tow also starts to have σ_{33} damage at the location indicated by A as the oxidation simulation nears the end of 200 hours. A similar simulation was performed for a constant strain level of 0.4%. In this case, the initial damage state is more extensive compared to the simulation with 0.2% strain. The matrix, fill tow and warp tow have considerable damage as shown in Figure 9.14. As expected, the coupled analysis predicted growth in the damage in the lower matrix pocket due to oxidation. Most of this damage occurs under σ_{11} failure mode along with σ_{22} and σ_{33} failure modes. In the case of the fill tows, the oxidation causes additional damage in the lower part of the tow under σ_{22} failure mode, as shown in Figure 9.14. Additional damage is also seen in the warp tow as an effect of the oxidation. The new damage in the warp tow occurs under σ_{22}, σ_{33} and σ_{13} failure modes.

Similar to Figure 9.10, Figure 9.15 shows the plot of the volume averaged σ_{xx} versus volume averaged ε_{xx} for the Set 2 model indicating the drop in the volume average σ_{xx} at the end of 200 hours of oxidation for the two simulations discussed earlier. Line A-A' shows that for the 0.2% strain level simulation, the volume averaged σ_{xx} stress dropped 13% at the end of 200 hours of oxidation whereas in the case of the 0.4% strain level, the corresponding stress dropped over 13.3% (indicated by line B-B'). Figure 9.16 shows the volume averaged σ_{xx} for all three simulations normalized with the initial volume averaged stress as the oxidation progresses over 200 hours. Just as the model with Set 1 material properties at the 0.09% strain level, there was no new damage due to oxidation and the volume averaged stress actually increases slightly, although it is not noticeable in Figure 9.16. In the case of the other two strain levels, the drop in volume averaged stress is more gradual than the behavior seen in the corresponding models with Set 1 material properties. Although there are some sudden drops in the volume averaged stress as seen in Figure 9.16, they are not as significant as the drops seen in Figure 9.11. This behavior is attributed to growth in the matrix damage observed in the Set 2 laminates that is not seen in the Set 1 laminates.

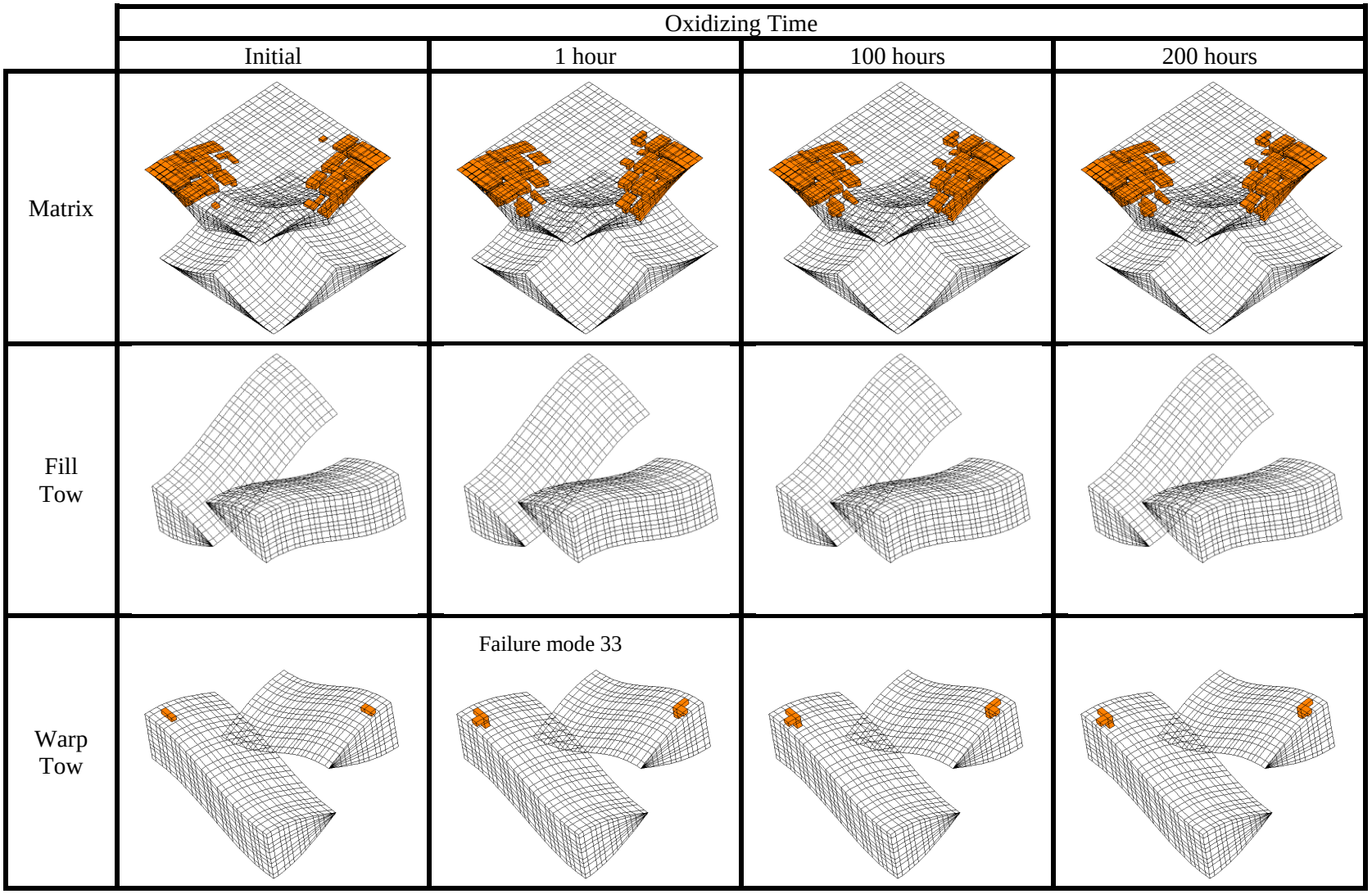

Figure 9.12: Evolution of damage due to oxidation in the two-ply laminate at 0.1% strain using Set 2 material properties

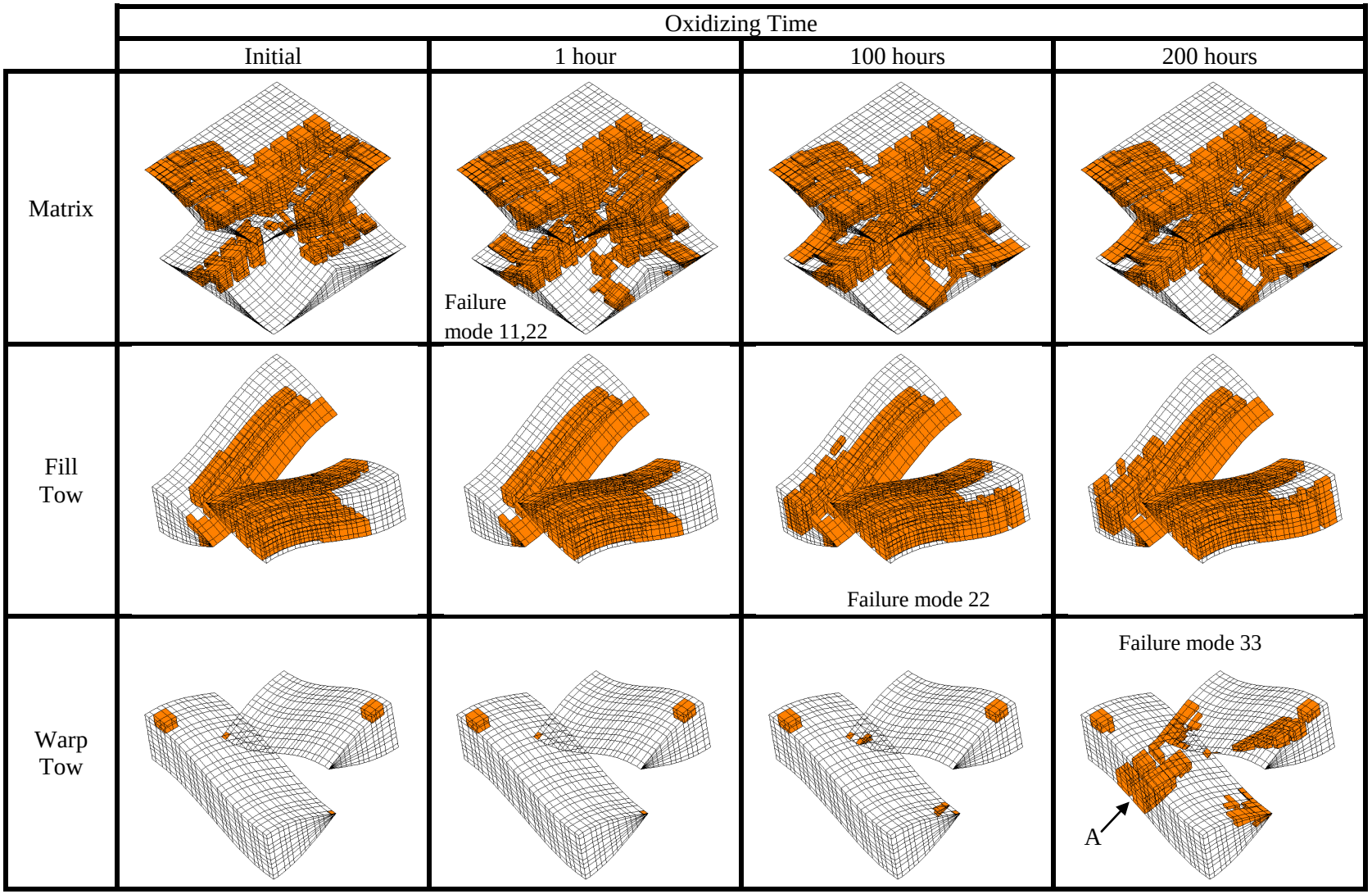

Figure 9.13: Evolution of damage due to oxidation in the two-ply laminate at 0.2% strain using Set 2 material properties

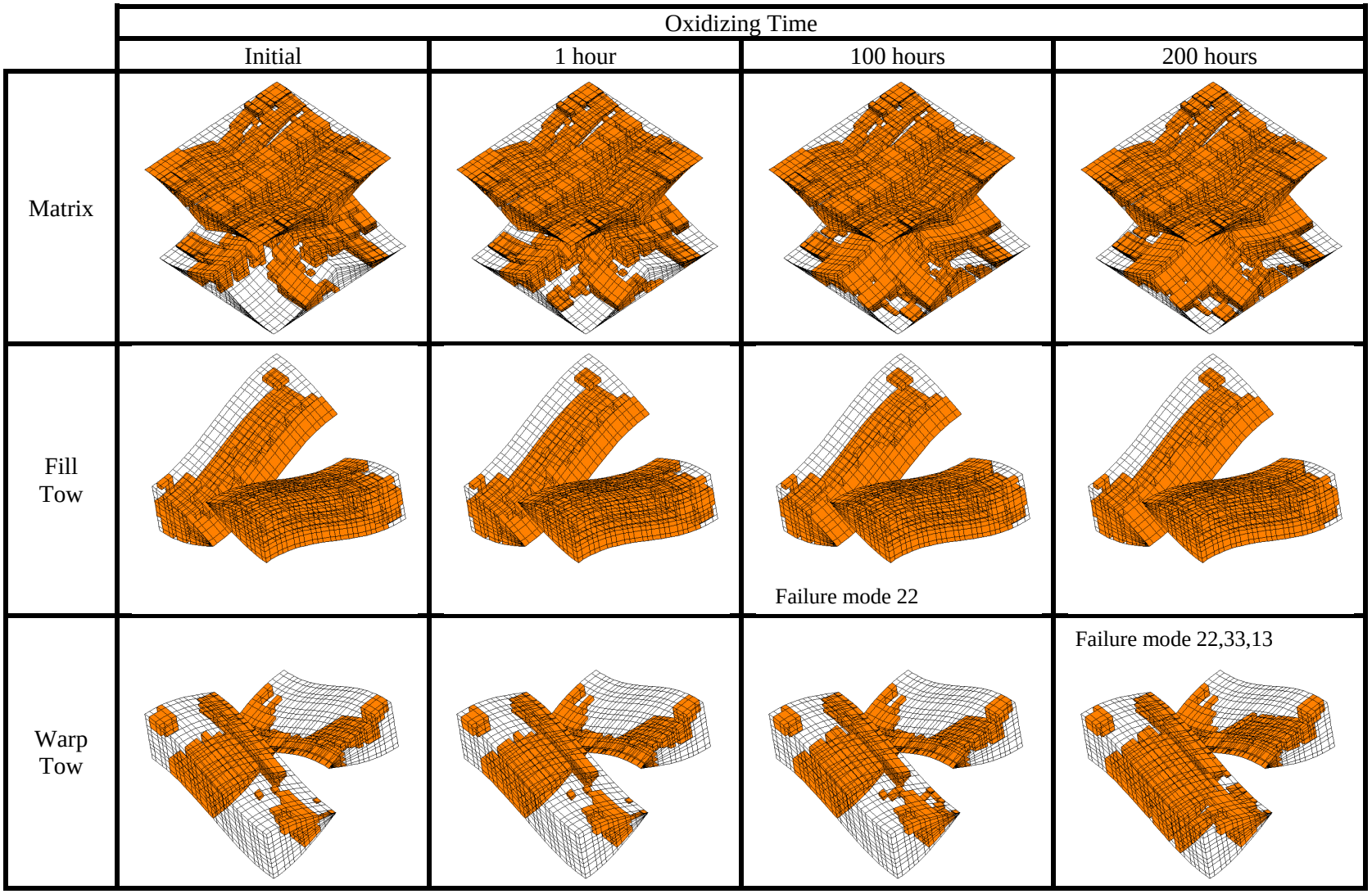

Figure 9.14: Evolution of damage due to oxidation in the two-ply laminate at 0.4% strain using Set 2 material properties

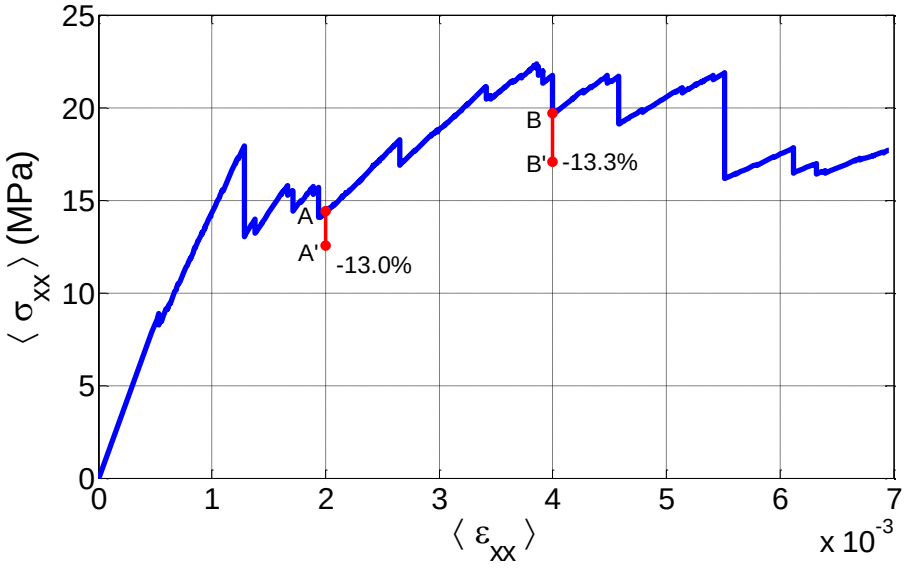

Figure 9.15: Volume averaged stress-volume averaged strain for the Set 2 material two- ply laminate showing drop in stress after 200 hours of oxidation

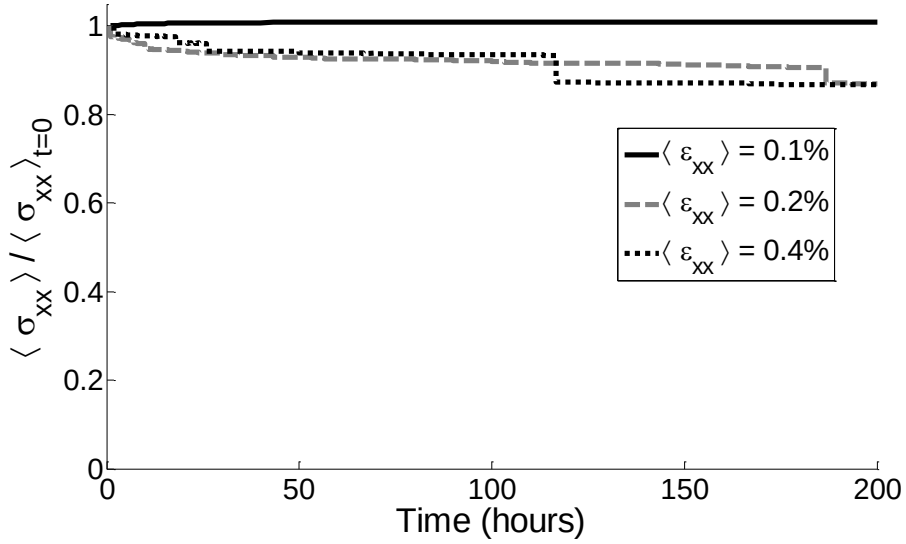

Figure 9.16: Variation in volume averaged stress due to oxidation for the Set 2 material two-ply laminate at different strain levels

9.6.2. Effect of number of plies

A parametric study was conducted to see if the number of plies in the laminate had any significant effect on the mechanical behavior under oxidation. In addition to the laminates that were discussed in the previous section, 4-ply and 6-ply laminates were analyzed for both Set 1 and Set 2 material properties. First, a damage progression analysis (i.e. no oxidation) was performed on the laminates to determine the mechanical behavior as the load on the laminate was increased. Figure 9.17 gives a plot of the volume averaged σ_{xx} with the volume averaged ε_{xx} for the different laminates using Set 1 material properties. It shows that the overall behavior is not significantly different, which is not surprising. Figure 9.18 shows the same plot for the laminates with Set 2 material properties. Again, the number of plies does not seem to have an effect on the overall behavior. Looking at the evolution of damage in the laminates revealed generally the same trends as seen in the 2-ply laminates. In the case of the Set 1 laminates, the fill tows had initial damage and continued to accumulate much more damage than the warp tows followed by the matrix, which had very little failure. In the case of Set 2 laminates, as seen in the corresponding 2-ply laminate, the damage initiates in the matrix followed by the fill tow failing considerably while the warp tow has less damage in comparison.

The coupled simulations were performed on these laminates as was done for the 2-ply laminates discussed in the previous section. The laminates were analyzed at different strain levels and overall they showed the same trends as seen in the 2-ply laminates. If the strain levels are too low, for example at 0.1%, the oxidation was not found to have any significant effect of the mechanical behavior. The results from the 0.2% and 0.4% strain level simulations will be discussed here. Since the general trends are the same as compared to the 2-ply laminates, the evolution of damage in each laminate will not be discussed here. Instead, comparisons of the overall behavior will be discussed. Comparing the results from the 2-ply, 4-ply and 6-ply laminates is not easy since they do not follow the same load path as shown in Figure 9.18. It would definitely not make sense to make comparisons at same strain level using the predicted volume average stress values because of the same reason. It makes more sense to look at the percentage drop in the volume average stress.

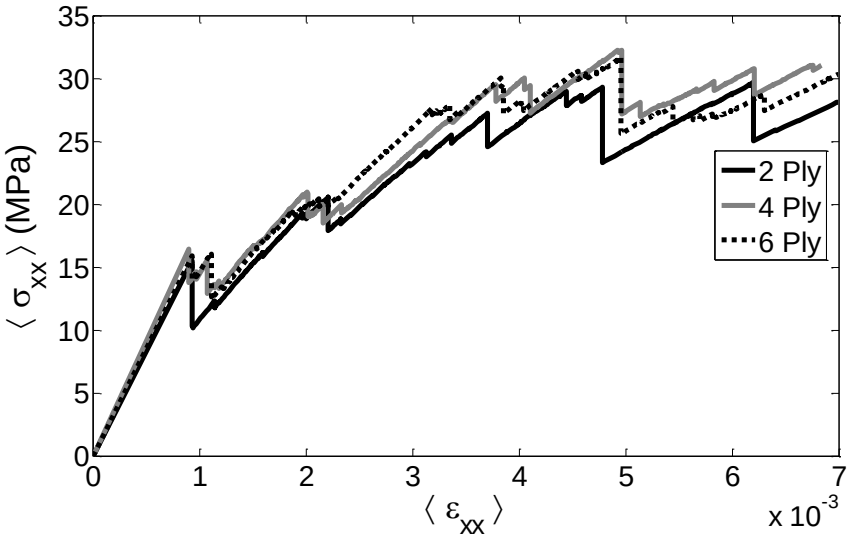

Figure 9.17: Volume averaged stress-volume averaged strain curves for the laminate with Set 1 material properties

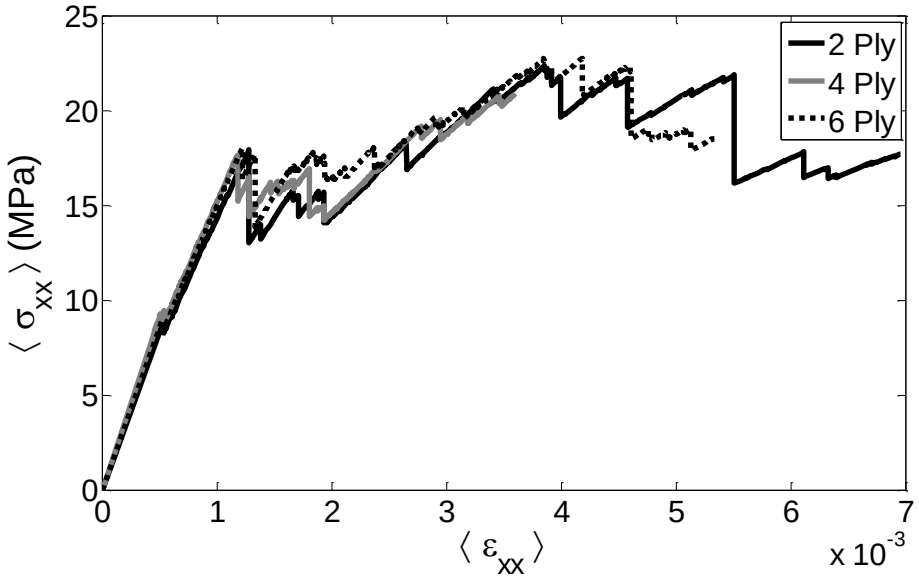

Figure 9.18: Volume averaged stress-volume averaged strain curves for the laminate with Set 2 material properties

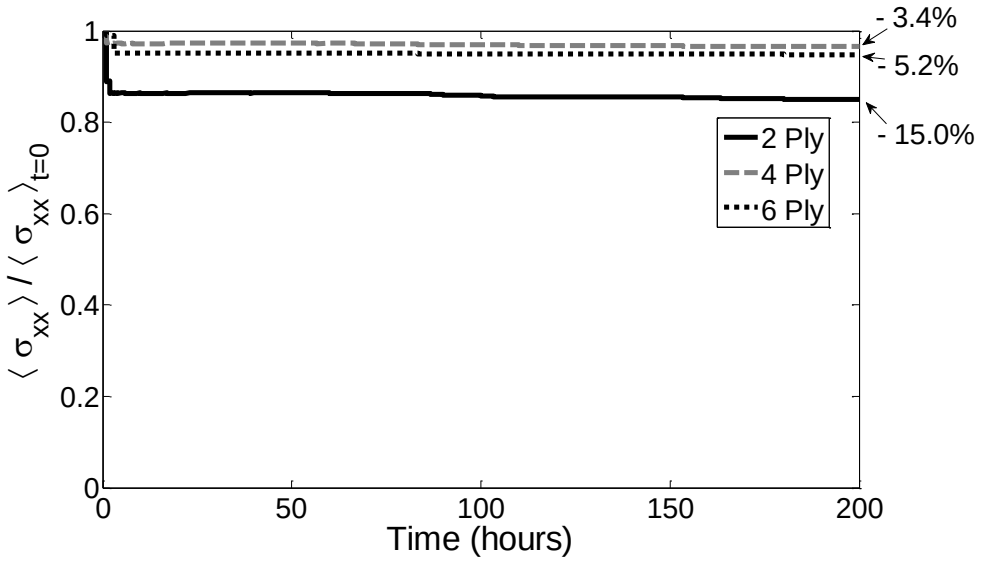

Figure 9.19: Variation in volume averaged stress due to oxidation for the various Set 1 material laminates at 0.2% strain level

Figure 9.19 shows the variation in normalized volume average stress at 0.2% strain for the 2-ply, 4-ply and 6-ply laminates using Set 1 materials. In the 2-ply laminate, under a 0.2% strain level, the volume average stress drops 15% whereas in the 4-ply model, it drops only 3.4%, which indicates that the damage in the 4-ply laminate was not significant. This is intuitive since a smaller fraction of the laminate is getting oxidized when the number of plies increases from 2 to 4. However when the number of plies is increased from 4 to 6, the stress drop increases slightly from 3.4% to 5.2%. This particular trend could not be explained but as discussed later in this section, this counter-intuitive behavior was not observed for the other material set or for other strain levels. Figure 9.19 also shows that all the Set 1 material laminates experience the significant drop in the volume average stress within 3 hours of oxidation. Figure 9.20 shows the variation of the normalized stress for the 0.4% strain level. It shows the percentage drop in the volume average stress at the end of 200 hours steadily reducing as the number of plies in the laminate increase. Comparison of Figures 9.19 and 9.20 shows that when the strain level was increased, the decrease in percentage load drop was more gradual with the number of plies. In the case of 0.4% strain, the drop is 22.4% for a 2-ply laminate, 14.8% for a 4-ply laminate and 9.5% for a 6-ply laminate. On the other hand, in the 0.2% strain level, as seen in Figure 9.19, the percentage drop reduces from 15% to less than 6% as the number of plies is increased to 4 and 6. Note that this trend is specific to the laminates with Set 1 material properties and cannot be generalized. Similar simulations were performed on the corresponding laminates with Set 2 material properties and Figures 9.21 and 9.22 shows the variation in volume average stress for 0.2% and 0.4% strain loading respectively. Again, a similar trend is seen where there is a significant reduction in the percentage drop in volume average stress at the end of 200 hours (from 13% to 4.1%) for a 0.2% loading when the number of plies is increased from 2 to 4. When the number of plies is increased to 6, the drop is only 3.3%, which is a further reduction in the

drop compared to the corresponding case in the Set 1 material laminates. Also, the variation in the normalized stress with respect to time is much more gradual in the Set 2 laminates as compared to the Set 1 laminates. When the strain level is increased to 0.4%, again similar trends are seen where the reduction in the percentage drop is not as drastic as that for 0.2% strain. Figure 9.22 shows that the percentage volume average stress drop at the end of 200 hours of oxidation reduces from 13.3% to 7% when the number of plies go up from 2 to 4 and the drop further reduces to 5.2% when the number of plies is increased to 6. This behavior can be explained based on the fact that the oxidation process oxidizes the same amount of material in all these laminates. In the coupled simulations described in this work, the oxidation analysis does not depend on the stress or damage state in the laminate. Therefore, regardless of the number of plies, the oxidation layer thickness varies in the same manner in all the laminates. This also has to do with the fact that at the end of the 200 hour simulation, the maximum predicted oxidation layer thickness is less than the thickness of a single ply. Increasing the number of plies in the laminate effectively increases the amount of material that can carry load, but the oxidation process only affects the same amount of material regardless the number of plies. Therefore, it would be expected that the percentage drop in volume average stress, or load drop, would decrease as the number of plies increased.

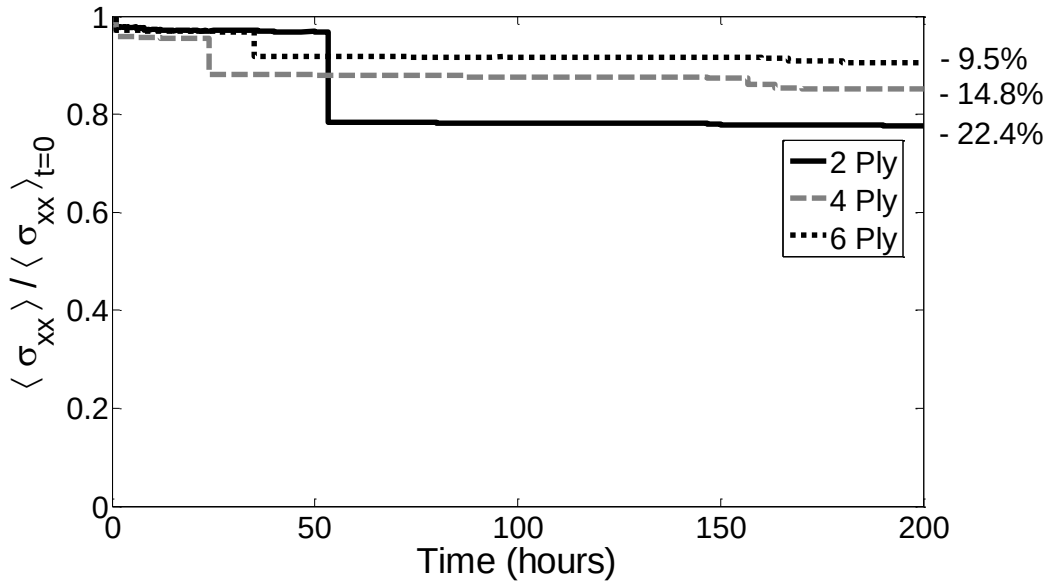

Figure 9.20: Variation in volume averaged stress due to oxidation for the various Set 1 material laminates at 0.4% strain level

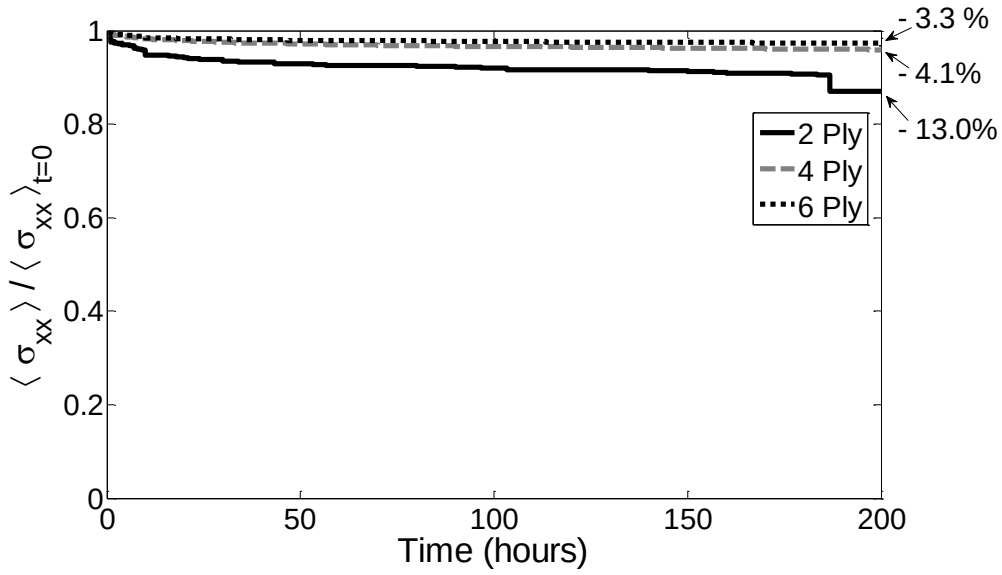

Figure 9.21: Variation in volume averaged stress due to oxidation for the various Set 2 material laminates at 0.2% strain level

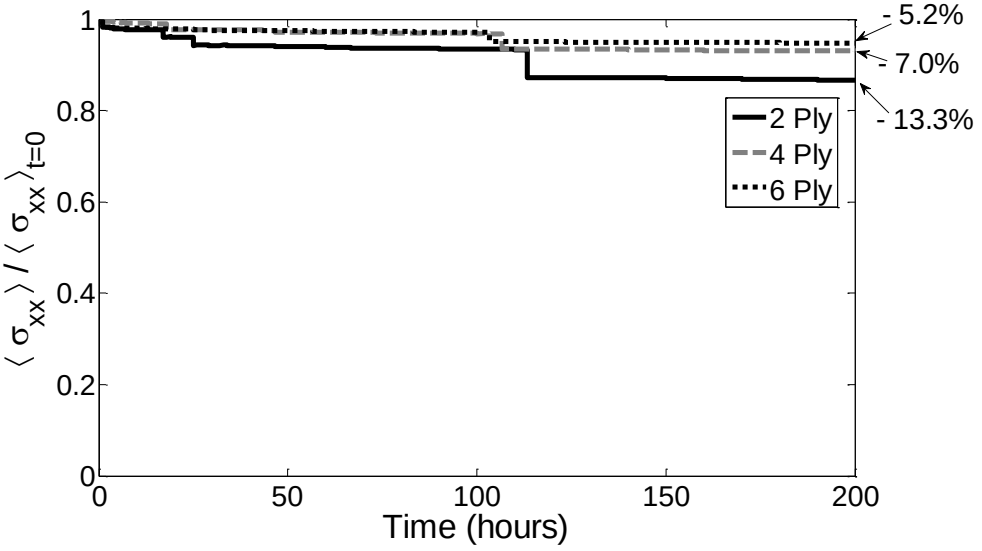

Figure 9.22: Variation in volume averaged stress due to oxidation for the various Set 2 material laminates at 0.4% strain level

8.10. Summary

The coupled analysis model described in Section 3 is used to predict the mechanical behavior of woven composite laminates that are under mechanical load as well as exposed to oxygen. The configuration that is analyzed and the complete parameters for the material system and the constitutive relations are described in this section. The current implementation of the coupled analysis model makes a number of assumptions when simulating the behavior of the laminate. The effects of thermal expansion and the shrinkage of the matrix due to oxidation are ignored. These are effects that need to be considered in future implementations of the coupled analysis model in order to represent more accurately the behavior of the underlying mechanisms. The effect of the stress and damage state on the oxidation behavior also needs to be considered in future enhancements of the coupled model. However, the analyses described in this work provide a framework for the implementation of a more robust tool to predict the behavior of laminates under oxidation. Due to lack of a full set of reliable material properties, two sets of material properties were assumed to the represent the typical behavior of composite materials. Simulations were performed on laminates with both sets of properties. The predicted mechanical behavior due to the effect of oxidation was described. This included illustrating the initiation and progression of damage in the laminate. A parametric study was also performed to determine the effect of the number of plies on the mechanical behavior under oxidation.

10. Conclusions and Future Work

This research work has contributed in various ways to help develop a better understanding of textile composites and materials with complex microstructures in general. An instrumental part of this work was the development of a framework that made it convenient to perform multiscale/multiphysics analyses of advanced materials such as textile composites with complex microstructures. In addition to the studies conducted in this work, this framework lays the groundwork for continued research of these materials. In addition to implementing an oxidation model, the framework was also used to implement strategies that expedited the simulation of oxidation in textile composites so that it would take only a few hours. Finally, a coupled diffusion/oxidation and damage progression analysis was implemented that was used to study the mechanical behavior of textile composites under mechanical loading as well as oxidation. The following sections discuss the conclusions drawn from the work performed to achieve the objectives of this research effort. This section concludes by mentioning some suggestions for possible future work.

10.1. Simulation of oxidation in textile composites

The oxidation behavior of textile composites was simulated using the finite element framework that was developed as part of this work. This involved implementing various strategies because of the multiple scales of microstructure involved in the configuration. An oxidation model was implemented based on the model developed by Pochiraju et al to simulate oxidation in neat PMR-15 resin. Homogenized oxidation material properties for a unidirectional laminate or tow were determined assuming that the fiber was impermeable and un-oxidizable. The homogenized properties were validated using different configurations. It was also determined that the oxidation behavior in heterogeneous configurations is complex and depends on various factors such as the location of the material boundaries. The oxidation model had severe limitation on the element size and time step size based on the finite element formulation. Therefore, a typical oxidation analysis was very computationally intensive and it was not feasible to simulate oxidation of a textile composite without strategies to expedite the analysis. Optimal element sizes were determined and the time step size was ramped up to achieve better efficiencies. An adaptive meshing strategy was also developed that exploited certain characteristic of the oxidation behavior to reduce the size of the problem. The adaptive meshing strategy was able to give computational time savings of over 60%. However, these initial strategies were not enough to make a full 3D oxidation analysis feasible. Therefore, a decoupled subdomain strategy was developed that divided up a 3D analysis domain into an array of 1D domains which could then be solved in a more timely manner. The 1D models could also be analyzed independently on different processors in a multi-core machine thereby increasing the efficiency even further. The decoupled subdomain strategy was validated and used in conjunction with the adaptive meshing strategy to simulate oxidation of a plain weave laminate. The analysis revealed that the tow architecture of the textile composite had a significant effect on the distribution of the oxidation front location in the woven configuration. After 200 hours of oxidation of a 200 micron thick ply, the smallest oxidation layer thickness was found to 84 microns whereas the largest was 110 microns. Later increases in efficiency and the use of parallel algorithms eventually led to the ability to perform three-dimensional oxidation analysis in a timely manner. However, when 3D results are compared to results obtained through the decoupled subdomain strategy, it is seen that the strategy performs remarkably well given the significant simplifying assumptions involved.

10.2. Prediction of damage progression in textile composites under oxidation

The multiscale/multiphysics analysis framework was used to implement a coupled diffusion/oxidation and continuum damage analysis to study the mechanical behavior of textile composites in oxidizing environments. The current implementation of the coupled model considers only the effect of oxidation on the mechanical behavior and not vice versa. Since only one-way coupling was assumed, the oxidation simulation could be performed independently before the coupled analysis. The coupled analysis was used to predict progressive damage in a Graphite/PMR-15 plain weave laminate that is uniaxially loaded to a fixed strain level and then exposed to oxidation through the top and bottom surfaces. A constitutive model was developed that degrades the engineering properties depending on the mechanical state and how much the material has oxidized. Due to lack of a full set of reliable material properties, two sets of material properties were assumed to represent the typical behavior of composite materials. The predicted mechanical behavior due to the effect of oxidation was described and an attempt was made to explain some of the behavior observed. The simulations showed the evolution of damage in the composite as it undergoes oxidation. It was seen that in some cases the effect of oxidation is not localized and that damage also occurs in regions that are not oxidized due to load redistribution. The simulations also showed the variation of the volume averaged stress in the laminate as the laminate oxidizes. It was seen that the various stress allowables of the materials in the laminate had an effect on this behavior. A parametric study was also performed to determine the effect of the number of plies on the mechanical behavior under oxidation. The simulations predicted a significant drop in the load carried by a 2-ply laminate for different strain levels and the load drop reduced, as expected, when the number of plies was increased to 4 and 6. However, the proportion by which the load drop reduces was not very intuitive and indicates that the material properties and the microstructure of the textile laminates have a complicated effect on the behavior under oxidation.

10.3. Future Work

Over the course of this research work, several ideas came up that might have successfully helped in advancing the understanding of these advanced materials. However, not all of them could be pursued due to various reasons. In addition to this, there are some obvious extensions to the research work presented in this dissertation. Some of them are listed below:

1. For analyzing even smaller length scales, hybrid models directly linking atomistic regions to continuum finite element regions have been developed by several researchers. These include the FEAt model [59], the MAAD approach [60,61], the QuasiContinuum method [62-64] and the coupled atomistic and discrete dislocation plasticity (CADD) approach [65] and the bridging scale method [66]. Currently, the hierarchical strategies explained in this work are implemented only for the continuum mechanics regime. However, it might be worthwhile to explore the possibility of using these strategies in analyzing multiple scale problems involving the atomistic scale.
2. The current finite element formulation for the oxidation model assumes that the time step is small enough that the assumptions to account for the nonlinearity hold. Future extensions to the model could look at defining a residual and iterating to drive the residual to zero to account for the nonlinearity at each time step.

3. When trying to replace a heterogeneous material with a homogenized material in an oxidation model, it is reasonable to assume that some or possibly all of these properties might change. In addition to the current homogenization strategy, there is at least one other possible approach for achieving this goal. One is to use a multi-scale analysis that keeps track of the 'local' information such as oxidation state and actual average concentration in the constituent matrix in the homogenized material. Given this information, it would be possible to calculate the reaction rate R at a particular material point in the tow's constituent matrix using Eq.(3.55). Next, the effective reaction rate for the larger scale homogenized tow is determined by a simple rule of mixtures and plugged into the governing equations. When the equations for a time step are solved, the calculated concentrations are transformed back to the local scale using a rule of mixtures in order to keep track of the oxidation state of the constituent matrix. Thus, a continuous transfer of information between the two scales needs to be maintained throughout the simulation.
4. In this work, the fibers in the tows are idealized to be in a square array and the fibers are assumed to be impermeable and do not oxidize. While there are other factors that can influence the oxidation behavior in composites such as the properties of the fiber/matrix interface or interphase, they are not taken into account for the homogenization model described in this work. Cracks in the matrix or along the fiber/matrix interface can also affect the oxidation behavior by allowing rapid ingress. Depending on the type of damage that is observed in these composites, it might be possible to account for their effects in the homogenized model. For example, if the damage is diffuse, the homogenized properties can be degraded appropriately or if the damage is confined to certain areas, cracks can be introduced in the homogenized model. These and other such factors should be addressed in a likely extension to the model.
5. The oxidation level information from the decoupled subdomain strategy is currently approximated as a single linear function to define the active zone. A better approximation could be made using a few more points to define a piecewise linear function for the active zone.
6. A simple constitutive model or property degradation scheme was developed to account for the effect of oxidation on the mechanical behavior. This scheme can be modified and enhanced in the future when the effect of oxidation on the coupled oxidation-mechanical behavior is more accurately determined. This can also include a constitutive model to account for the effect of mechanical damage on the oxidation behavior, which would make the analysis fully coupled.
7. The effects of thermal expansion and the shrinkage of the matrix due to oxidation are ignored in the current implementation of the coupled model. These are effects that should to be considered in future implementations of the coupled analysis model in order to more accurately represent the behavior of the underlying mechanisms.

Publications and Presentations

This award has contributed to research that has been presented in the following publications and presentations:

Journal Publications:

1. Varghese, J., and Whitcomb, J. (2009). Micromechanics of Oxidation in Composites with Impermeable Fibers, *Journal of Composite Materials*, 43(19): 2011-2043.

2. Owens, B., Whitcomb, J., Varghese, J. (2010) "Effect of Finite Thickness and Free Edges on Stresses in Plain Weave Composites", *Journal of Composite Materials*, 44(6): 675 - 692.

3. Varghese, J., Owens, B., and Whitcomb, J. Simulation of Oxidation in Textile Composites, *Journal of Composite Materials*, Submitted March 2010.

Dissertations and Theses:

1. Owens, B. (2009) Implementation of B-splines in a conventional finite element framework, Master's Thesis, Department of Aerospace Engineering, Texas A&M University, College Station, TX.

2. Varghese, J. (2009). A Finite Element Framework for Multiscale/Multiphysics Analysis of Structures with Complex Microstructures, PhD Dissertation, Department of Aerospace Engineering, Texas A&M University, College Station, TX.

Proceedings:

1. Varghese, J., Whitcomb, J., Goyal, D., "Finite Element Analysis of Progressive Damage in Textile Composites Due to Oxidation", *49th AIAA/ASME/ASCE/AHS/ASC Structures, Structural Dynamics, and Materials Conference*, April 7-10, 2008, Schaumburg, IL.

2. Varghese, J., and Whitcomb, J., "Micromechanics of Oxidation in Composites with Impermeable Fibers", *49th AIAA/ASME/ASCE/AHS/ASC Structures, Structural Dynamics, and Materials Conference*, April 7-10, 2008, Schaumburg, IL.

3. Owens, B., Whitcomb, J., Varghese, J., "Effect of Free Edges on Stresses in Woven Composites", *TexComp 9: International Conference on Textile Composites*, October 13-15, 2008, University of Delaware.

4. Owens, B., Whitcomb, J., and Varghese, J., "Effect of Mesh Refinement on Various Measures of Convergence for Plain Weave Composites" *50th AIAA/ASME/ASCE/AHS/ASC Structures, Structural Dynamics & Materials Conference*, May 4-7, 2009, Palm Springs, CA.

5. McLendon, R., Whitcomb, J., and Varghese, J., "Predicting Damage Progression for a Fiber Reinforced Orthotropic Lamina Undergoing Shear Loading", *50th AIAA/ASME/ASCE/AHS/ ASC Structures, Structural Dynamics & Materials Conference*, May 4-7, 2009, Palm Springs, CA.

6. Varghese, J. and Whitcomb, J., "Prediction of Damage Progression in Textile Composites In Oxidizing Environments", *SEM Annual Conference & Exposition on Experimental and Applied Mechanics*, June 1-4, 2009, Albuquerque, NM.

7. Varghese, J. and Whitcomb, J., "Simulation of Oxidation in Textile Composites", *17th International Conference on Composite Materials (ICCM-17)*, July 27-31, 2009, Edinburgh, UK.

Conference Presentations:

1. Whitcomb, J., Varghese, J., and Goyal, D., "Finite Element Analysis of Progressive Damage in Textile Composites due to Oxidation", *ASME International Mechanical Engineering Congress & Exposition*, November 11-16, 2007, Seattle, WA.

2. Whitcomb, J. and Varghese, J. "Framework for Rapid FE Analysis of Textile Composites", *ASME International Mechanical Engineering Congress & Exposition*, November 11-16, 2007, Seattle, WA.

3. Varghese, J., Whitcomb, J., and Goyal, D., "Finite Element Analysis of Progressive Damage in Textile Composites due to Oxidation", *44th Annual Technical Meeting, Society of Engineering Science*, October 21-24, 2007, College Station, TX.

4. Varghese, J., Whitcomb, J., Goyal, D., "Finite Element Analysis of Progressive Damage in Textile Composites Due to Oxidation", *49th AIAA/ASME/ASCE/AHS/ASC Structures, Structural Dynamics, and Materials Conference*, April 7-10, 2008, Schaumburg, IL.

5. Varghese, J., and Whitcomb, J., "Micromechanics of Oxidation in Composites with Impermeable Fibers", *49th AIAA/ASME/ASCE/AHS/ASC Structures, Structural Dynamics, and Materials Conference*, April 7-10, 2008, Schaumburg, IL.

6. Owens, B., Whitcomb, J., Varghese, J., "Effect of Free Edges on Stresses in Woven Composites", *TexComp 9: International Conference on Textile Composites*, October 13-15, 2008, University of Delaware.

7. Owens, B., Whitcomb, J., and Varghese, J., "Effect of Mesh Refinement on Various Measures of Convergence for Plain Weave Composites" *50th AIAA/ASME/ASCE/AHS/ASC Structures, Structural Dynamics & Materials Conference*, May 4-7, 2009, Palm Springs, CA.

8. McLendon, R., Whitcomb, J., and Varghese, J., "Predicting Damage Progression for a Fiber Reinforced Orthotropic Lamina Undergoing Shear Loading", *50th AIAA/ASME/ASCE/AHS/ ASC Structures, Structural Dynamics & Materials Conference*, May 4-7, 2009, Palm Springs, CA.

9. Varghese, J. and Whitcomb, J., "Prediction of Damage Progression in Textile Composites In Oxidizing Environments", *SEM Annual Conference & Exposition on Experimental and Applied Mechanics*, June 1-4, 2009, Albuquerque, NM.

10. Varghese, J., and Whitcomb J., "Prediction of Damage Progression in Textile Composites in Oxidizing Environments", *17th International Conference on Composite Materials (ICCM-17)*, July 27-31, 2009, Edinburgh, UK.

References

1. Luan, X. G., Cheng, L. and Zhang, L. (2005). Life Prediction of 3D Woven C-SiC Composites at High Temperatures with Low-frequency Cyclic Stresses, *Journal of Composite Materials*, **39**(13): 1195-1202.

2. Hale, J. M. and Gibson, A. G. (1998). Coupon Tests of Fibre Reinforced Plastics at Elevated Temperatures in Offshore Processing Environments, *Journal of Composite Materials*, **32**(6): 526-543.

3. Haque, A. and Rahman, M. (2000). Durability and Damage Development in Woven Ceramic Matrix Composites Under Tensile and Fatigue Loading at Room and Elevated Temperatures, *Journal of Engineering Materials and Technology*, **122**(4): 394-401.

4. Peddiraju, P., Noh, J., Whitcomb, J. and Lagoudas, D. C. (2007). Prediction of Cryogen Leak Rate Through Damaged Composite Laminates, *Journal of Composite Materials*, **41**(1): 41-71.

5. Shen, C. H., Springer, G. S. (1981). Effects of Moisture and Temperature on the Tensile Strength of Composite Materials. In: GS Springer (ed), *Environmental Effects on Composite Materials*. pp. 79–93, Technomic Publishing, Lancaster, PA.

6. Roy, S., Reddy, J. N. (1988). A Finite Element Analysis of Adhesively Bonded Composite Joints with Moisture Diffusion and Delayed Failure. *Comput. Struct*, **29**: 1011–31.

7. Weitsman, Y. (1990). Moisture in Composites: Sorption and Damage. In: Reifsnider, K. L., (ed), *Composite Materials Series – 4: fatigue of composites*. pp. 385–429, Elsevier, New York.

8. Dasgupta, A., Agarwal, R. K. (1992). Orthotropic Thermal Conductivity of Plain-Weave Fabric Composites using Homogenization Technique. *J Compos Mater*, **26**: 2736–58.

9. Roy, S., Dharani, L. R., Gupta, V., Xu, W. (2000). Modeling of Hygrothermal and Aging Effects in Textile Composites. *41st AIAA/ASME/ASCE/AHS/ASC Structures, Structural Dynamics, and Materials Conference and Exhibit*, Atlanta, GA, Apr. 3-6, AIAA-2000-1682.

10. Li, Y., Tang, X., Miranda, J., Sue, H. J., Whitcomb, J. D. and Bradley, W. (1999). Study of Moisture Diffusion Behavior in Hybrid IM7/BMI Composites. In: *Proceedings of the 57th Annual Technical Conference*. New York: Society of Plastics Engineering.

11. Tang, X., Whitcomb, J. D., Li, Y. and Sue, H. J. (2005). Micromechanics Modeling of Moisture Diffusion in Woven Composites, *Composites Science and Technology*, **65**: 817–826.

12. Whitcomb, J. D. and Tang, X. (2001). Micromechanics of Moisture Diffusion in Composites with Impermeable Fibers, *Journal of Composite Materials*, **36**(9): 1093–102.

13. Tang X., (2001). Micromechanics of 2D Woven Composites, PhD Dissertation, Department of Aerospace Engineering, Texas A&M University, College Station, TX.

14. Yin, X., Cheng, L., Zhang, L., Xu, Y. and Luan, X. (2001). Oxidation Behavior of Three-Dimensional Woven C-SiC Composites, *Mater. Sci. Tech.*, **17**(4): 727-730.

15. Strife, J. R. and Sheehan, J. E. (1988). Ceramic Coatings for Carbon-Carbon Composites, *American Ceramic Society Bulletin*, **67**(2): 369.

16. Courtois, C., Desmaison, J., Tawil, H., (1991). Protection Against Oxidation of C/SiC Composites by Chemical Vapour Deposition of Titanium Diboride : Deposition Kinetics and Oxidation Behaviour of Films Prepared from TiCl4/BCl3/H2 Mixtures, *Journal de Physique IV (Colloque)*, **1**(C2): 657-664.

17. Halbig, M. C., Eckel, A. J., Cawley, J. D. and Brewer, D. N. (1997). Stressed Oxidation of C/SiC Composites, *Proceedings of the 21st Annual Conference on Composites, Advanced Ceramics Materials and Structures*, Cocoa Beach, Florida, January 12-16.

18. Luan, X. G., Cheng, L. and Zhang, L. (2005). Life Prediction of 3D Woven C-SiC Composites at High Temperatures with Low-frequency Cyclic Stresses, *Journal of Composite Materials*, **39**(13): 1195-1202.

19. Halbig, M. C., Eckel, A. J. and Cawley, J. D. (1999). Oxygen Diffusion and Reaction Kinetics in Continuous Fiber Ceramic Matrix Composites, NASA/TM—1999-208911, National Aeronautics and Space Administration Lewis Research Center ARL–TR–1692

20. McKee, D. W. (1988). Oxidation Behavior of Matrix-Inhibited Carbon/Carbon Composites, *Carbon*, **26**:659-665.

21. Ochoa, O. O. and Elliott, C. H. (1998). Inhibited Carbon-Carbon Composites: Isothermal and Fatigue Exposure, *Journal of Composite Materials*, **32**(12): 1157-1177.

22. Luo, R., Zheng, Y. and Li, L. (2000). Effect of Additives on Mechanical Properties of Oxidation-Resistant Carbon/Carbon Composite Fabricated by Rapid CVD Method, *Carbon*, **38**(15): 2109-2115.

23. Mazany, A. M., Bianco, R. and Stover, E. R. (2005). Oxidation Inhibition of Carbon-Carbon Composites, Patent publication number: WO/2005/047213, latest accessed online

24. Tandon G. P., Pochiraju K.V. and Schoeppner G.A. (2006). Modeling of oxidative development in PMR-15 resin, *Polymer Degradation and Stability*, **91:** 1861-1869.

25. Schoeppner, G.A., Tandon, G.P., and Pochiraju, K.V. (2008). Predicting Thermo-oxidative Degradation and Performance of High-Temperature Polymer Matrix Composites, In: Kwon, Young W. Allen, David H. and Talreja, Ramesh R. (eds.), *Multiscale Modeling And Simulation Of Composite Materials And Structures*, **1st edn**, p. 359, Springer, New York.

26. Schoeppner, G.A., Tandon, G.P., and Pochiraju, K.V. (2008). Predicting Thermo-oxidative Degradation and Performance of High-Temperature Polymer Matrix Composites, In: Kwon, Young W. Allen, David H. and Talreja, Ramesh R. (eds.), *Multiscale Modeling And Simulation Of Composite Materials And Structures*, **1st edn**, p. 359, Springer, New York.

27. Rupnowski, P., Gentz, M., Kumosa, M., (2006). Mechanical Response of a Unidirectional Graphite Fiber/Polyimide Composite as a Function of Temperature, *Composites Science and Technology*, **66**: 1045–1055.

28. Rupnowski, P., Gentz, M., Sutter, J., Kumosa, M., (2004). Mechanical Response of a Woven Graphite/Polyimide Composite to In-Plane Shear Dominated Loads at Room and Elevated Temperatures, *Acta Materialia*, **52**: 5603–5613.

29. Odegard, G., Kumosa, M., (2000). Determination of Shear Strength of Unidirectional Composite Materials with the Iosipescu and 10^{o}-Axis Shear Tests, *Composites Science and Technology*, **60**: 2917-2943.

30. Pochiraju, K., Tandon, G., Schoeppner, G., (2008). Evolution of Stress and Deformations in High-Temperature Polymer Matrix Composites during Thermo-Oxidative Aging, *Mechanics of Time-Dependent Materials*, **12**: 45–68.

31. Roy, S., Singh, S., Schoeppner, G., (2008). Modeling of Evolving Damage in High Temperature Polymer Matrix Composites Subjected to Thermal Oxidation, *Journal of Material Science*, **43**: 6651–6660.

32. Wang, S., Chen, X., (2006). Computational Micromechanics for High-Temperature Constitutive Equations of Polymer-Matrix Composites With Oxidation Reaction, Damage, and Degradation, *Journal of Engineering Materials and Technology*, **128**(1): 81.

33. Varghese, J. (2009). A Finite Element Framework for Multiscale/Multiphysics Analysis of Structures with Complex Microstructures, PhD Dissertation, Department of Aerospace Engineering, Texas A&M University, College Station, TX.

34. Colin, X., Verdu, J., (2003). Thermal Aging and Lifetime Prediction for Organic Matrix Composites, *Plastics Rubber and Composites*, **32**: 349–3562.

35. Colin, X., Marais, C., Verdu, J., (2001). A New Method for Predicting the Thermal Oxidation of Thermoset Matrices: Application to an Amine Cross-Linked Epoxy, *Polymer Testing*, **20**: pp.795–803.

36. Pochiraju, K. V., Tandon. G. P., (2004). Time dependent Composite Material Behavior Under Thermo-Oxidative Environmental Conditions. In: *Proceedings of IMECE*, Anaheim, CA.

37. Bowles, K. J., Jayne, D., Leonhardt, T. A. and Bors, D., (1993). Thermal Stability Relationships Between PMR-15 resin and Its Composites. NASA Technical Memorandum 106285.

38. Bowles, K. J., Papadopoulos, D. S., Inghram, L. L., McCorkle, L. S. and Klan, O. V. (2001). Longtime Durability of PMR-15 Matrix Polymer at 204, 260, 288 and 316°C, NASA/TM-2001-210602.

39. Tsuji, L. C., McManus, H. L. and Bowles, K. J. (1998). Mechanical Properties of Degraded PMR-15 Resin. NASA Technical Report, 1998-208487: 1–18.

40. Abdeljaoued, K. (1999). Thermal Oxidation of PMR-15 Polymer Used as a Matrix in Composite Materials Reinforced with Carbon Fibers, MS Thesis, Ecole Nationale Superieure des Arts et Metiers, Paris.

41. Johnson, T. F. and Gates, T. S., (2001). High Temperature Polyimide Materials in Extreme Temperature Environments, In: AIAA Paper 2001-1214, *42nd AIAA/ASME/ASCE/AHS/ASC Structures, Structural Dynamics and Materials Conference and Exhibition*, Seattle, WA.

42. Schoeppner, G. A., Tandon, G. P. and Ripberger, E. R. (2007). Anisotropic Oxidation and Weight Loss in PMR-15 Composites. *Composites Part A: Applied Science and Manufacturing*, **38**: 890–904.

43. Tang, X. and Whitcomb, J. D. (2003). General Techniques for Exploiting Periodicity and Symmetries in Micromechanics Analysis of Textile Composites, *Journal of Composite Materials*, **37**: 1167 - 1189.

44. Goyal, D. and Whitcomb, J. D. (2006). Analysis of Stress Concentrations in 2 x 2 Braided Composites, *Journal of Composite Materials*, **40**(6): 533-546.

45. Reddy, J. N., (1993). *An Introduction to the Finite Element Method*, 2nd ed., McGraw-Hill, Inc., New York.

46. Colin, X., Marais, C., Verdu, J., (2001). Thermal Oxidation Kinetics for a Poly(bismaleimide). *Journal of Applied Polymer Science*, **82**: 3418–3430.

47. Colin, X., Marais, C., Verdu, J. (2002). Kinetic Modeling and Simulation of Gravimetric Curves: Application to the Oxidation of Bismaleimide and Epoxy Resins. *Polymer Degradation and Stability*, **78**: 545–553.

48. Quaresimin, M., (2002). Fatigue of Woven Composite Laminates Under Tensile and Compressive Loading, *10th European Conference on Composite Materials (ECCM-10),* Brugge, Belgium.

49. Goyal, Deepak. Analysis of Linear Elasticity and Non-Linearity due to Plasticity and Material Damage in Woven and Biaxial Braided Composites, PhD Dissertation, Texas A&M University, 2007.

50. Odegard, G., Kumosa, M., (2000). Elastic-Plastic and Failure Properties of a Unidirectional Carbon/PMR-15 Composite at Room and Elevated Temperatures, *Composites Science and Technology*, **60**: 2979-2988.

51. Hull, D. and Clyne, T. (1996). *An Introduction to Composite Materials*, 2nd Ed, Cambridge University Press, New York.

52. Srirengan, K. and Whitcomb, J. D. (1998). Finite Element Based Degradation Model for Composites with Transverse Matrix Cracks, *Journal of Thermoplastic Composites*, **11**: 113-123.

53. Blackketter, D. M., Walrath, D. E. and Hansen, A. C. (1993). Modeling damage in a plain weave fabric-reinforced composite material, *Journal of Composites Technology & Research*, **15**(2): 136-142.

54. Choiy, J and Tamma, K. K. (2001). Woven Fabric Composites Part I: Predictions of Homogenized Elastic Properties and Micromechanical Damage Analysis, *Int. J. Numer. Meth. Engr*, **50**:2285-2298.

55. Zako, M., Uetsujib, Y., Kurashikia, T. (2003). Finite Element Analysis of Damaged Woven Fabric Composite Materials, *Composites Science and Technology*, **63**: 507–516.

56. Nicoletto, G. and Riva, E. (2004). Failure Mechanisms in Twill-Weave Laminates: FEM Predictions vs. Experiments, *Composites: Part A*, **35**: 787–795.

57. Guagliano, M. and Riva, E. (2001). Mechanical behaviour prediction in plain weave composites, *Journal of Strain Analysis*, **36**(2): 153-162.

58. Chapman, C.D. and Whitcomb, J.D., (2000). Thermally Induced Damage Initiation and Growth in Plain and Satin Weave Carbon-Carbon Composites, *Mechanics of Composite Materials and* Structures, **7**: 177-194.

59. Gumbsch, P. (1995). An Atomistic Study of Brittle Fracture: Toward Explicit Failure Criteria from Atomistic Modeling, *J. Mater. Res.*, **10**(11):2897-2907.

60. Abraham, F.F., Broughton, J.Q., Bernstein, N. and Kaxiras, E. (1998). Spanning the Length Scales in Dynamic Simulation, *Computers in Physics*, **12**(6): 538.

61. Abraham, F.F., Bernstein, N., Broughton, J. Q. and Hess, D. (2000). Dynamic Fracture of Silicon: Concurrent Simulation of Quantum Electrons, Classical Atoms, and the Continuum Solid, *MRS Bulletin*, **25**(5):27-32.

62. Tadmor, E.B., Ortiz, M. and Phillips, R. (1996). Quasicontinuum Analysis of Defects in Solids, *Philosophical Magazine A*, **73**(6):1529.

63. Shenoy, V., Miller, R., Tadmor, E. B., Rodney, D., Phillips, R. and Ortiz, M. (1999). An Adaptive Methodology for Atomic Scale Mechanics - The Quasicontinuum Method, *J. Mech. Phys. Sol.*, **47**:611-642.

64. Shenoy, V., Miller, R., Tadmor, E. B., Phillips, R. and Ortiz, M. (1998). Quasicontinuum Models of Interfacial Structure and Deformation, *Phys. Rev. Lett.*, **80**(4):742.

65. Shilkrot, L. E., Miller, R. E. and Curtin, W. A., (2002). Coupled Atomistic and Discrete Dislocation Plasticity, *Phys. Rev. Lett.*, **89**:025501-1–025501-4.

66. Park, H.S., Karpov, E.G., Klein, P.A. and Liu, W.K. (2005). The Bridging Scale for Two-Dimensional Atomistic/Continuum Coupling, *Philosophical Magazine*, **85**(1):79-113.